COMPETING REACTION CHANNELS IN IR LASER INDUCED UNIMOLECULAR REACTIONS

Berman, M.R.

1981

MASTER

LBL-12213

Lawrence Berkeley Laboratory

UNIVERSITY OF CALIFORNIA

Materials & Molecular Research Division

COMPETING REACTION CHANNELS IN IR-LASER-INDUCED UNIMOLECULAR REACTIONS

Michael Robert Berman
(Ph.D. thesis)

January 1981

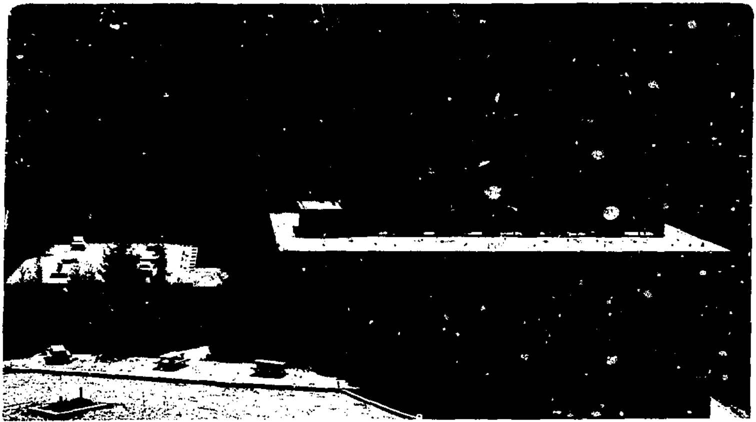

Prepared for the U.S. Department of Energy under Contract W-7405-ENG-48

DISTRIBUTION OF THIS DOCUMENT IS UNLIMITED

Competing Reaction Channels in IR-Laser-Induced Unimolecular Reactions

Michael Robert Berman

Abstract

The competing reaction channels in the unimolecular decomposition of two molecules, formaldehyde and tetralin were studied. A TEA CO_2 laser was used as the excitation source in all experiments. The dissociation of D_2CO was studied by infrared multiphoton dissociation (MPD) and the small-molecule nature of formaldehyde with regard to MPD was explored. The effect of collisions in MPD were probed by the pressure dependence of the MPD yield and IR fluorescence from multiphoton excited D_2CO. MPD yield shows a near cubic dependence in pure D_2CO which is reduced to a 1.7 power dependence when 15 Torr of NO is added. The peak amplitude of 5 μm IR fluorescence from D_2CO is proportional to the square of the D_2CO pressure in pure D_2CO or in the presence of 50 Torr of Ar. The results are explained in terms of bottlenecks to excitation at the v=1 level which are overcome by a combination of vibrational energy transfer and rotational relaxation. The wavelength and power dependence of MPD yield were also studied.

The radical/molecule branching ratio in D_2CO MPD was measured using NO as a radical scavenger to be 0.10 ± 0.02 at a fluence of 125 J/cm^2 at 946.0 cm^{-1}. This result is fit using a set of rate equations to model MPD in order to locate the barrier height to molecular dissociation in D_2CO. The calculations are most sensitive to the relative locations of the barrier height and the radical threshold.

The barrier height to molecular dissociation was calculated to be 3.6 ± 2.0 kcal/mole below the radical threshold or 85.0 ± 3.0 kcal/mole above the ground state of D_2CO. In H_2CO, this corresponds to 2.5 ± 2.0 kcal/mole below the radical threshold or 83.8 ± 3.0 kcal/mole above the ground state. Comparison with UV data indicate that RRKM theory is an acceptable description of formaldehyde dissociation in the 5-10 Torr pressure range.

The unimolecular decomposition of tetralin was studied by MPD and SiF_4 - sensitized pyrolysis. Both techniques induce decomposition without the interference of catalytic surfaces. Ethylene loss is identified as the lowest energy reaction channel. Dehydrogenation is found to result from step-wise H atom loss. Isomerization via disproportionation is also identified as a primary reaction channel.

Dedicated to

my parents

ACKNOWLEDGEMENTS

As I reflect on the past years that I have spent in Berkeley, I feel fortunate to have shared these times with a wonderful group of people. I have enjoyed myself while learning a great deal. I'd like to thank all of you who helped make it possible.

I have had the pleasure of performing this research under the direction of Brad Moore. I have learned much from Brad whose insights and encouragements were invaluable. I would like to express my thanks and appreciation for his guidance and patience throughout the course of this work.

My foray into the realm of organic chemistry was the result of a collaboration with Paul Comita and Bob Bergman. I have enjoyed sharing our different perspectives on the same problem. Much of the success of these experiments was due to Paul's ability to put deuterium atoms in just the right places.

The members of the Moore group have been superb colleagues and cohorts. I have greatly enjoyed and benefitted from many conversations with Hai-Lung Dai and Linda Young on the state of science and the world. Jim Weisshaar and Pauline Ho shared in exploring the secrets of formaldehyde. The assembly of my trusty CO_2 laser was in no small part due to the help of Andy Kung. Floyd Hovis introduced me to the highly intermittent world of signal averagers while Andy Lanford and Alison Abatte kept me tapping my toes (Rocky Top!). Jackie Denney oversees the menagerie below and somehow keeps things running as smoothly as they do.

The preparation of this thesis was greatly assisted by Cordelle Yoder who expertly typed this manuscript and by Nancy Monroe and Gloria Pelatowski who drew the figures.

Special thanks are reserved for Steve Hansen and Shanta Devarajan with whom I shared innumerable unique conversations and even more fond memories.

I would like to express my love and appreciation to my wife, Sally. We have shared the good times and the bad breaks. Through it all, her love and smiles have been constant sources of strength and encouragement. Finally, I want to thank my parents, sister, and my entire family for all of their love and support. I love you all, dearly.

This work was supported by the Assistant Secretary for Nuclear Energy, Office of Advanced Isotope Separation Technology, Advanced Isotope Separation Technology Division of the U.S. Department of Energy under Contract No. W-7405-ENG-48.

TABLE OF CONTENTS

TABLE OF CONTENTS (continued)

Blank

CHAPTER I

INTRODUCTION

Unimolecular reactions, either dissociation or isomerization, are among the simplest systems of chemical reactions. They encompass such common yet diverse gas phase reactions as the pyrolysis of hydrocarbons in an automobile engine and the photodissociation of ozone in the upper atmosphere. Rate constants for such reactions usually obey the general Arrhenius equation

$$k = A\, e^{-E_a/kT}$$

however, this offers little basic insight into the dynamics of unimolecular reactions.

Modern theories of unimolecular reactions are based on the theory due to Lindemann[1] developed in 1923. Many advances have followed[2-7] culminating in the widely used RRKM theory.[8-9] According to these theories, an energized molecule reacts with a rate constant that is dependent on its total energy content. Often, more than one reaction channel is available to an energized molecule. Under one set of conditions, pyrolysis at a low temperature or photolysis with long wavelength light for example, one reaction may predominate. When higher temperatures or shorter wavelength excitation is used, another reaction may begin to contribute or even dominate. Product ratios will therefore vary with excitation conditions. The competition between reaction pathways is governed by the Arrhenius parameters of the reactions, the activation energy E_a and the pre-exponential A-factor. By measuring the product or branching ratios in unimolecular reactions, the energetics of these pathways can be investigated.

Unimolecular reactions can be initiated in many ways. Theoretical descriptions of unimolecular reactions are insensitive to the method of generating the excited molecule. Pyrolysis in static vessels, flow tubes, shock tubes or flames, chemical activation and UV photolysis have been the stalwart experimental techniques over the past decades. The development of high power infrared lasers has provided the capability for dissociating molecules with purely vibrational excitation. IR multiphoton excitation (MPE) provides a method for funneling large quantities of vibrational energy directly into a molecule and inducing dissociation. IR multiphoton dissociation (MPD) has quickly become a common tool of the modern photochemist.

When direct excitation of a molecule is unable to provide sufficient excitation due to poor absorption of the laser light, this powerful energy source can be utilized to indirectly excite the molecules of interest. Collisional energy transfer from a strongly absorbing but non-dissociating species can be used to heat the species of interest to temperatures greater than 1000 K, sufficient to cause dissociation. This technique provides the bonus that homogeneous gas phase unimolecular reactions can be induced at high temperatures in the absence of hot surfaces whose catalytic effects can drastically alter the branching ratio.

In this thesis, the latter two techniques, IR MPD and sensitized pyrolysis are used to study the competing reaction channels in two gas phase systems. In the first system, MPD is used to investigate the ground state photochemistry of formaldehyde. The branching ratio between dissociation to radical and molecular products can be used to discern the energetics of these reaction pathways. In addition, the dynamics of small-molecule MPD are explored. In the second system, the organic molecule tetralin, both techniques are employed to identify the lowest energy reaction pathway and elucidate the dissociation mechanism.

At this point, a brief discussion of MPD is in order due to its central role in this work. In MPD, a molecule is driven by an intense laser field up a ladder of vibrational levels to dissociation. Several review articles[10-12] are available which distill much of the burgeoning MPD literature. The photophysics of MPD have been described by several authors.[13-15] Generally, the vibrational energy levels of a molecule are divided into three regions. Excitation in region I consists of a single or multiphoton transition between discrete vibration-rotation states. Several photons (usually between 1 to 5) are absorbed in this region depending on the density of states of the molecule. Excitation in region I determines the wavelength dependence of MPD. The frequency that delivers maximum MPD is usually slightly red shifted[16] from the peak of the one photon absorption spectrum. This shift compensates for the detuning of the laser from resonance at higher vibrational levels which are more closely spaced than the fundamental due to anharmonicity. Many explanations[16-18] have been offered to justify how detuning in region I is compensated for, but no single explanation is as general as the process of MPD has proved to be. Excitation in region 1 remains the least well documented part of MPD.

As a molecule absorbs more and more photons, the density of vibrational states at the energy of the next step can become so large that a resonance is assured. Region II is defined by such a quasi-continuum (QC) which is established when the spacing between levels is less than the laser bandwidth. In this region, absorption, which can be incoherent, is quite easy and the molecule can quickly be brought to the dissociation limit. This is the origin of region III. States above the dissociation limit have lifetimes that can be calculated by RRKM theory. In region III, dissociation will compete with further excitation and deactivation. It has been shown[19-21] that a rate equation model can be used successfully to describe these competing processes in MPD in regions II and III. MPD yield has been shown to be determined by the laser fluence not laser power due to the incoherent excitation in the QC. When more than one reaction channel competes with excitation, however, the branching ratio will be dependent on the excitation rate in region III and hence the laser power.

Most studies of MPD have centered on relatively large (5-10 atoms) polyatomic molecules since their large density of states produces a QC that begins at low energies (1000-5000 cm^{-1}) facilitating collisionless dissociation. Small molecules display some different MPD characteristics. Collisions and higher powers are needed to drive molecules through region I. The role of collisions in the excitation process is probed by the pressure dependence of dissociation and IR fluorescence from multiphoton excited D_2CO in Chapter III of this thesis.

Formaldehyde photochemistry in the UV has been extensively studied both experimentally[22-29] and theoretically.[30-35] Chapters III and IV contain, respectively, experimental and theoretical descriptions of formaldehyde photochemistry in the infrared, for which the molecule remains on the ground state potential surface. A long standing question in formaldehyde photochemistry has been: what is the height of the barrier to dissociation to molecular products? The competition between excitation, deactivation and dissociation in the MPD of formaldehyde provides a probe of this barrier height that is manifested in the branching ratio between radical and molecular products. Using a rate equation model with the RRKM rates for molecular dissociation calculated by Miller and the experimentally observed branching ratio, the barrier height can be extracted. Since IR MPD compliments UV photochemistry, these results must be consistent with UV observations.

The final chapter of this thesis deals with the unimolecular decomposition of tetralin. Dissociation by flow pyrolysis[36,37] and chemical activation[38] lead to markedly different product distributions. The former exhibits H_2 loss as the major reaction channel while C_2H_4 elimination is predominant in the latter. In order to resolve this discrepancy, two other methods of activation were used: MPD and sensitized pyrolysis using SiF_4 as the absorbing medium. The results identify ethylene loss as the lowest energy reaction channel with dehydrogenation in the flow pyrolysis being, to some extent, surface catalyzed. The mechanism of decomposition was also investigated in detail with the use of isotopically labeled tetralins. These experiments display the utility of sensitized pyrolysis as a means to study homogeneous gas phase reactions that are prone to surface catalysis.

References

1. F. A. Lindemann, Trans. Faraday Soc. 17, 598 (1922).

2. C. N. Hinshelwood, Proc. Roy. Soc. (A). 113, 230 (1927).

3. N. B. Slater, Theory of Unimolecular Reactions, (Methuen, London, 1959).

4. O. K. Rice and H. C. Ramsperger, J. Am. Chem. Soc. 49, 1617 (1927); ibid. 50, 617 (1928).

5. L. S. Kassel, J. Phys. Chem. 32, 225 (1928); ibid. 32, 1065 (1928).

6. R. A. Marcus and O. K. Rice, J. Phys. and Colloid Chem. 55, 894 (1951).

7. R. A. Marcus, J. Chem. Phys. 20, 359 (1952).

8. P. J. Robinson and K. A. Holbrook, Unimolecular Reactions, (Wiley, New York, 1972).

9. W. Forst, Theory of Unimolecular Reactions, (Academic, New York, 1973).

10. R. V. Ambartzumian and V. S. Letokhov in Chemical and Biochemical Applications of Laser, Vol. III, ed. C. B. Moore, (Academic New York, 1977), p. 167.

11. N. Bloembergen and E. Yablonovitch, Phys. Today, May 1978, p. 23.

12. P. A. Schulz, Aa. S. Sudbø, D. J. Krajnovich, H. S. Kwok, Y. R. Shen, and Y. T. Lee, Ann. Rev. Phys. Chem. 30, 379 (1979); P. A. Schulz, Ph.D. Dissertation, University of California, Berkeley, 1979.

13. S. Mukamel and J. Jortner, Chem. Phys. Lett. 40, 150 (1976); J. Chem. Phys. 65, 5204 (1976).

14. J. Stone, M. F. Goodman, and D. A. Dows, Chem. Phys. Lett. 44, 411 (1976); J. Chem. Phys. 65, 5052, 5062 (1976).

15. M. Quack, J. Chem. Phys. 69, 1282 (1978); ibid. 70, 1069 (1979).

16. R. V. Ambartzumian, Yu. A. Gorokhov, V. S. Letokhov, G. N. Makarov and A. A. Puretskii, JETP Lett. 23, 22 (1976).

17. V. S. Letokhov and A. A. Makarov, Opt. Commun. 17, 250 (1976).

18. C. D. Cantrell and H. W. Galbraith, Opt. Commun. 18, 513 (1976); ibid. 21, 374 (1977).

19. E. R. Grant, P. A. Schulz, Aa. S. Sudbø, Y. R. Shen and Y. T. Lee, Phys. Rev. Lett. 40, 115 (1978).

20. W. Fuss, Chem. Phys. 36, 135 (1979).

21. J. L. Lyman, J. Chem. Phys. 67, 1868 (1977).

22. J. H. Clark, C. B. Moore, and N. S. Nogar, J. Chem. Phys. 68, 1264 (1978).

23. A. Horowitz and J. G. Calvert, Int. J. Chem. Kinet. 10, 713 (1978); ibid. 10, 805 (1978).

24. P. L. Houston and C. B. Moore, J. Chem. Phys. 65, 757 (1976).

25. J. P. Reilly, J. H. Clark, C. B. Moore and G. C. Pimentel, J. Chem. Phys. 69, 4381 (1978).

26. R. S. Lewis and E. K. C. Lee, J. Phys. Chem. 82, 249 (1978).

27. J. C. Weisshaar and C. B. Moore, J. Chem. Phys. 70, 5135 (1979); ibid. 72, 2875 (1980).

28. J. C. Weisshaar, Ph.D. Dissertation, University of California, Berkeley, 1979.

29. M. B. Zughul, Ph.D. Dissertation, University of California, Berkeley, 1978.

30. D. M. Hayes and K. Morokuma, Chem. Phys. Lett. 12, 539 (1972).

31. R. L. Jaffe and K. Morokuma, J. Chem. Phys. 64, 4881 (1976).

32. M. J. H. Kemper, J. M. F. van Dijk, H. M. Buck, J. Am. Chem. Soc. 100, 7841 (1978).

33. D. F. Heller, M. L. Elert and W. M. Gelbart, J. Chem. Phys. 67, 4061 (1978).

34. J. D. Goddard and H. F. Schaefer, III, J. Chem. Phys. 70, 5117 (1979).

35. W. H. Miller, J. Am. Chem. Soc. 101, 6810 (1979).

36. A. G. Loudon, A. Maccoll, and S. K. Wong, J. Chem. Soc. (B), 1733 (1970).

37. T. Gangwer, D. MacKenzie, and S. Casano, J. Phys. Chem. 83, 293 (1979).

38. P. B. Comita and R. G. Bergman (private communication).

CHAPTER II

GENERAL EXPERIMENTAL

This chapter describes the basic experimental apparatus and procedures common to both sets of experiments discussed in this thesis. It focuses mainly on the CO_2 laser: its components, operating conditions and output characteristics. More detailed experimental procedures specific to the formaldehyde or tetralin experiments are described in Chapters III and V.

A. Laser

The excitation source in all of these experiments is a grating tuned CO_2 TEA laser. The major component of the laser is a Tachisto Model 215 discharge head. The discharge head was bolted to an aluminim base plate and fitted with ZnSe Brewster angle windows which selected the horizontal polarization. The laser cavity was 108 cm long defined by a Ge output coupler and a diffraction grating each mounted in a Burleigh model SG 101 Gimbal mount bolted to the base plate. The diffraction grating (PTR-Model 303), a master grating of 150 lines/mm ruled on Cu and blazed at 8 μm to give maximum reflectivity for the horizontal polarization at 10 μm, allowed selection of single vibration-rotation laser transitions. The output coupler typically used was a 2.5 cm diameter Ge disc (Coherent 50-8) having a 10 m radius of curvature on the cavity side. This surface was uncoated providing approximately 35% reflectivity. The output side was flat and AR coated for 10 μm. For experiments on weak laser transitions an output coupler coated for 50% reflectivity (Coherent) on the cavity side was used. An adjustable intracavity iris on a Unislide mount 5 cm from the output coupler defined the spatial mode of the beam. When fully opened, the laser output was a rectangular multimode beam, 1.9 x 1.2 cm, determined by the gain medium between the electrodes. Reducing the iris to a diameter of 6 mm provided a well defined Gaussian beam (see Figure II-1).

A 50 kV, 5 mA power supply (Hipotronics 50-B) provided the necessary energy for the discharge. Operating voltages ranged between 26-29 kV. A resistor chain with a total resistance of 50 MΩ was used to drop the voltage by a factor of 50 for measurement by a voltmeter with a full scale reading of 1 kV across 1 MΩ. The laser discharge was initiated by the breakdown of a spark gap triggered by a -200 V pulse from an external trigger box. The circuit diagram of the variable repetition rate trigger box is shown in Hovis' thesis.[1] The jitter in triggering relative to the 10 V synch out pulse was ± 200 ns. The laser was grounded to the base plate and through the ground wire of the 110 V AC input. An aluminum box enclosed the laser to reduce rf noise and a line filter (Corcom Model 3K5) was placed between the 110 V AC input and the HV power supply to prevent propagation of rf noise through the power cord.

Gases were flowed through Eastman Polyflow tubing. Flow rates were monitored by Dwyer RMA-6 flow meters and controlled by needle valves (Hoke 3132 M4B). Needle valves were installed at the laser and spark gap exhausts to maintain the appropriate gas mixture in the cavity when the laser was not in constant operation. This eliminated the need for a 10 minute purge before firing the laser. The gas mixture typically used had He : Ne : CO_2 flowmeter settings of 7 : 6 : 8 standard cubic ft air/h. The actual flow rate for each gas must be corrected by multiplying by (specific gravity of gas)$^{-\frac{1}{2}}$.

Figure II-1. Spatial distribution of intensity in the CO_2 laser pulse. The internal aperture of the laser was 9.0 mm. A 0.5 mm diameter pinhole was scanned in 0.5 mm steps. Transmitted light was detected by an Au:Ge detector. Each point is the average of 16 shots.

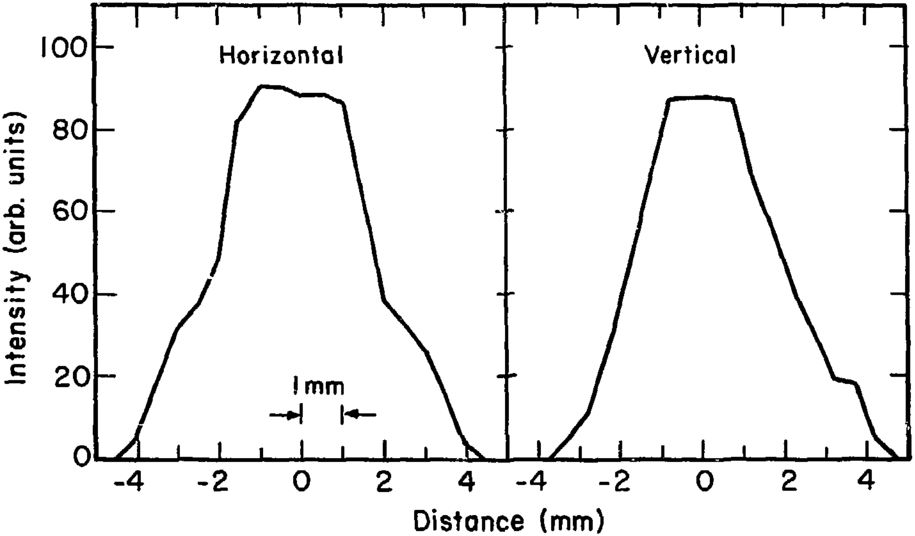
Horizontal
Vertical
Intensity (arb. units)
100
80
60
40
20
0
1mm
-4
-2
0
2
4
-4
-2
0
2
4
Distance (mm)

XBL 811-7508

This mixture provided laser output with a 70 ns peak followed by a 1.3 μs tail with the energy split almost equally between the two components (Figure II-2a). The tail could be reduced or entirely eliminated by removal of most or all of the N_2 from the gas mixture with an accompanying loss of power (Figure II-2b). Lower total power but slightly higher peak power could be obtained with 10 : 6 : 8 flow meter settings. The temporal profile of the pulse could also be affected by the position of the output coupler. Slight angular misalignment of the output coupler decreased the spike and enhanced the tail resulting in a broad pulse several hundred ns in duration. These pulses were spatially very asymmetric and of low energy. In all cases, the laser output showed a large amount of self mode locking.[2] Oscillations with a FWHM of 2.3 ns modulated the intensity by a factor of 2 in the peak and throughout the tail. They were spaced by ~7 ns peak-to-peak corresponding to the round trip time for light in the laser cavity. No attempt was made to eliminate this structure. The temporal shape of the pulse was measured by either a Molectron P-05 pyrolelectric detector or a Rofin Model 7415 photon drag detector (PDD).

The laser energy in all experiments was measured with a Scientech Model 38-0101 volume absorbing calorimeter. A Scientech Model 362 power-energy meter output device was used to integrate the output of a single pulse.

The average power reading for a given repetition rate was calibrated against the individual pulse energy of several pulses before and after the average power measurement. The pulse-to-pulse energy reproducibility was typically ±10%. This calibration process was repeated several times to minimize the effects of changing laser power during these measurements since the long time constant of the Scientech (~15 s) required waiting

Figure II-2. a) Temporal profile of CO_2 laser pulse under normal operating conditions as measured by the photon drag detector.

b) Temporal profile of pulse with nitrogen deficient gas mixture (He : N_2 : CO_2 flow meter settings 12 : 2 : 12).

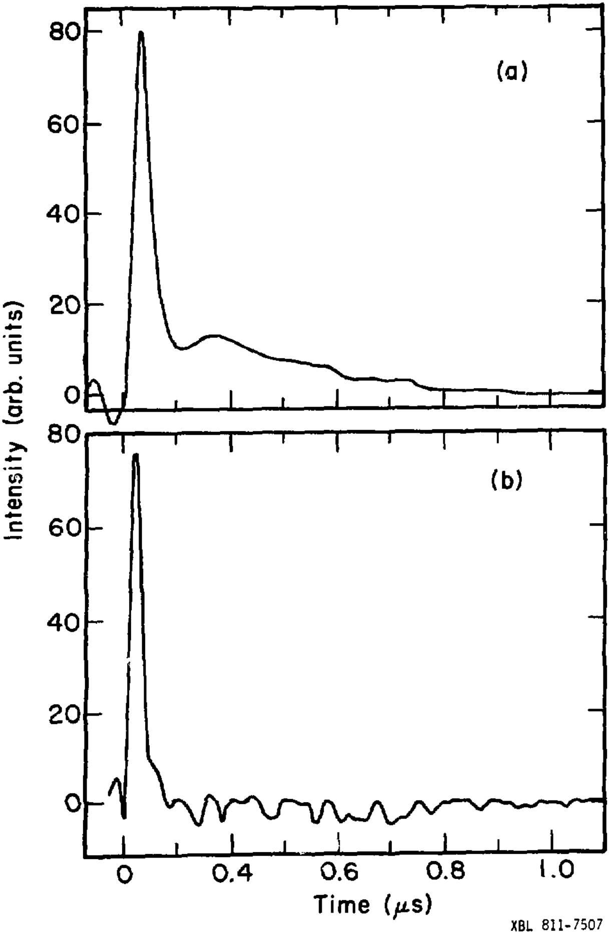
80
60
40
20
0
(a)
80
60
40
20
0
(b)
Intensity (arb. units)
0
0.4
0.6
0.8
1.0
Time (μs)

XBL 811-7507

at least a minute after the average power measurement before the energy of a single pulse could be measured. A NaCl beam splitter reflected about 5% of the beam into another Scientech power meter (Model 36-0001) so that the laser output could be independently monitored. There was no deviation in the energy per pulse measurement from the average power measurement divided by the repetition rate for rates of 0.87 Hz or 1.00 Hz. For a repetition rate of 0.32 Hz, average power measurements were 8% too high. This was a result of reading the peak voltage since a steady state value was never reached at this slow repetition rate.

Typical laser energy output was 2J/pulse with the intracavity iris fully opened on strong lasing transitions. Multiphoton dissociation experiments were typically performed with a 1.2 cm diameter aperture and energies between 1.0 and 1.5 J/pulse. With a 6 mm iris the beam energy was reduced to ~0.7 J/pulse. During continued operation, the grating position needed to be tuned slightly down and to the left (<0.001 inch) as components warmed up.

The laser wavelength was measured with an Optical Engineering CO_2 Spectrum Analyzer. Transitions observed with an uncoated Ge (cavity side) output coupler were, in the (001)-(10°0) band, R(8) to R(32) and P(8) to P(38), and in the (00°1)-(02°0) band, R(8) to R(34) and P(8) to P(42). Spacing between lines was about 0.002 and 0.004 in of the grating micrometer for R and P branches respectively. The 50% reflecting output coupler extended the range to P(46) in the (00°1)-(02°0) band with an increase of about a factor of 2 in power or the P(40) line (0.5 J/pulse with full aperture). The nominal linewidth of CO_2 TEA lasers[3] is $0.1\ cm^{-1}$.

Attenuation of the laser beam was accomplished by the insertion of either NaCl plates or gas cells with NaCl windows containing SF_6 or SiF_4. Varying the pressure of the absorbing gas changed the attenuation without significantly altering the spatial or temporal beam shape. The PDD output showed no observable change in the beam profile due to saturation or thermal blooming. Attenuation by uncoated Ge or CaF_2 flats produced interference stripes in the beam dramatically altering the intensity distribution and were not used.

The spatial profile of the laser beam was analyzed by scanning a pinhole (0.5 or 0.025 mm) on an X-Y translation stage (Micro Swiss International) across the beam. The transmitted light impinged on a NaCl diffuser and was scattered into a Au : Ge detector cooled to 77 K and equipped with a 5.6 KΩ load resistor. The output of 16 shots at each position was averaged. The resulting beam profile for a 9 mm internal aperture is shown in Figure II-1.

B. IR Fluorescence Detection

IR fluorescence experiments were carried out with either a Hg : Ge or Au : Ge photoconductive detector (SBRC), each 3 x 10 mm in size and cooled by LHe. The Cu detector was equipped with an SBRC model A320 current-feedback amplifier. This system had a time constant of 80 ns. The Hg detector employed an impedence matching buffer amplifier which has been previously described.[4] Its output was amplified by a Keithley 104 wideband amplifier. The time constant for this detector was ~300 ns. The output of this detector contained large rf noise spikes (~400 mV) in the few hundred ns directly before and after the pulse. This noise was approximately an order of magnitude less with the Cu detector.

A 2 mm thick BaF_2 window was mounted in front of the detector at the detector temperature. Dielectric-coated filters cooled to nearly 77 K were placed in the detector dewar filter wheel.[1,4] Scattered light was reduced by 3 mm of MgF_2 and 6 mm of CaF_2 externally mounted over the detector viewing window. A 2.5 cm focal length parabolic mirror was mounted just below the lower viewing window to reflect fluorescence back towards the detector. A 5 cm diameter f/1 CaF_2 lens was placed midway between the laser beam axis and the detector element (10 cm from each) to focus fluorescence onto the detector.

Signal averaging was achieved with a Biomation 8100 transient recorder, a Tracor-Northern 575A signal averager and a Hewlett-Packard 7004B X-Y recorder. Triggering was accomplished by the amplified output (~1 V) of the photon drag detector.

References

1. F. E. Hovis, Ph.D. Dissertation, University of California, Berkeley, 1979.

2. D. L. Lyon, E. V. George, and H. A. Haus, Appl. Phys. Lett. 17, 474 (1970); J. Gilbert and J. L. Lachambre, Appl. Phys. Lett. 18, 187 (1971).

3. P. R. Pearson and H. M. Lamberton, IEEE J. Quantum Electron, QE-8, 145 (1972); A. J. DeMaria, Proc. IEEE 61, 731 (1973).

4. J. Finzi, Ph.D. Dissertation, University of California, Berkeley, 1975.

CHAPTER III

IR MULTIPHOTON DISSOCIATION OF FORMALDEHYDE

A. Introduction

This chapter contains two basic thrusts, both related to multiphoton dissociation (MPD) in formaldehyde. The first few sections study the dynamics of MPD in formaldehyde, a species at the small molecule limit of MPD. The final section focuses on using MPD to study the photochemistry of formaldehyde.

The formaldehyde molecule has long been a favorite of experimental and theoretical photochemists since its small size often enables detailed analysis. Its size, however, proves to be a handicap for MPD. Its low density of states means that the QC will be difficult to reach and dissociation correspondingly hard to achieve. The well studied behavior of larger molecules, such as the MPD prototype SF_6, is not followed. Collisions, for example, are beneficial rather than detrimental[1] to dissociation. As previously observed[2,3] in other small molecules, higher power densities than those needed in SF_6 are required to achieve dissociation in formaldehyde. Such small molecule behavior manifests itself in such observables as the wavelength and pressure dependence of MPD and IR fluorescence from multiphoton excited molecules. These observations provide information regarding the nature and the position of the bottlenecks to excitation that exist in the molecule. These characteristics of MPD in formaldehyde are described in Sections C–E of this chapter.

The technique of MPD can be used to great advantage in formaldehyde to study photochemistry on its ground state potential surface. Most, if not all of formaldehyde UV photochemistry has been postulated[4,5] to take place through high vibrational levels of the ground electronic state, S_0. Theoretical calculations[4] show that the first excited singlet state, S_1, correlates to excited states of both molecular and radical dissociation products while S_0 correlates to the observed ground state products. Dissociation to radical products has a threshold between 87.6 and 89.4 kcal/mole above the ground state in D_2CO.[6] Molecular products are almost isoenergetic with formaldehyde but are separated by a large barrier (Fig. III-1). The location of this barrier has long been a question in formaldehyde photochemistry. Extensive calculations[7] have recently been performed in order to fix the barrier height. Using MPD along with calculated dissociation rates,[8] an experimental test of the calculated barrier height can be provided.

In MPD, formaldehyde molecules are driven stepwise, to higher and higher levels of vibrational excitation on the ground state potential surface (Fig. III-1). Tunneling through the barrier to molecular products may occur at any energy up the excitation ladder. With UV excitation, only a small section of the barrier is probed. The dissociation rates from these high vibrational levels increase with excitation energy[8] and at high enough energies the radical channel provides another available pathway. The ensuing competition between excitation and dissociation and the partitioning of molecules between the available reaction channels results in a branching ratio between radical and molecular dissociation for a given set of excitation conditions. The measurement of this branching ratio provides a probe of the energetics of these dissociative pathways. In Section F of this chapter the details of the measurement of the branching ratio are presented. The results are analyzed in Chapter IV in order to extract the barrier height to molecular dissociation relative to the D + DCO threshold.

Figure III-1. A schematic of the D_2CO potential energy surface. The ground state levels of products are shown. The top of barrier to molecular dissociation includes the transition state zero-point energy. The vertical arrows show IR multiphoton excitation, horizontal arrows represent dissociation through or above the barrier and the curved arrows depict the branching ratio.

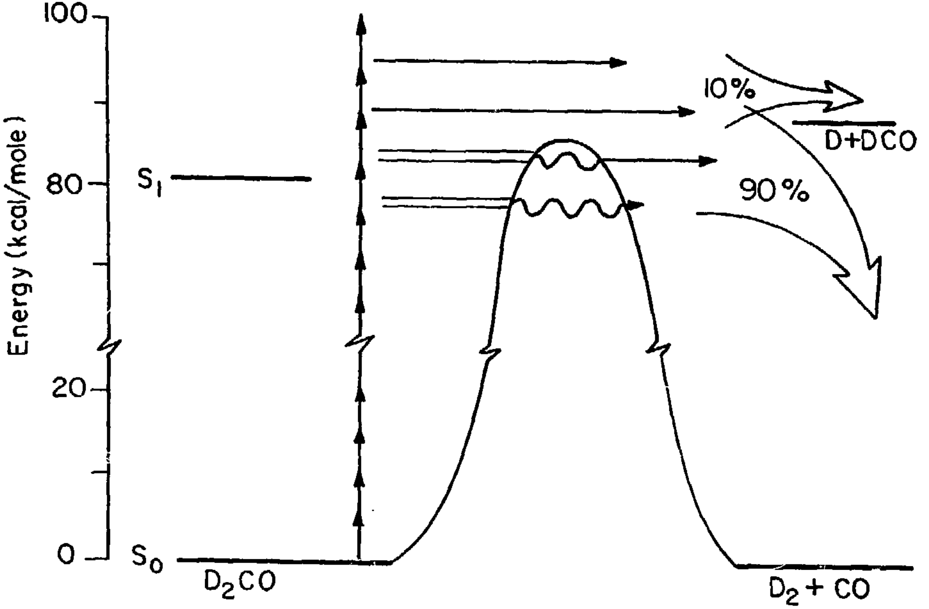

XBL 811-5056

B. Experimental

In this section the experimental conditions for the MPD experiments on formaldehyde will be described. Different laser conditions were used for different sets of experiments. In the wavelength dependence study of D_2CO the incident laser intensity was kept constant at 1.0 J/pulse for each laser line with the use of an SF_6 attenuation cell. All incident energies are corrected for the loss due to the front window of the cell which was measured in a separate experiment. Experiments were performed with the incident energies listed in Table III-1 except where otherwise noted. All fluences and power densities are calculated using the diameter at the $\frac{1}{e}$ power point of the beam (beam waist). From Figure II-2, 80% of the total beam energy passes through this area. The fluence is defined as

$$\text{Fluence} = \frac{0.8E_T}{a}$$

where E_T is the total energy per pulse and a is the cross sectional area at the beam waist defined by $a = \pi r_{1/e}^2$ where $r_{1/e}$ is the radius at the beam waist. Power densities are calculated for the 100 ns spike of the pulse neglecting self mode locking giving

$$I = \frac{0.8\ E_p}{a \times 10^{-7}}$$

where E_p is the energy in the 100 ns spike. Focusing was performed with either a 15 cm focal length NaCl lens or a 25 cm focal length anti-reflection coated Ge lens which gave beam waists of 0.08 and 0.10 cm, respectively.

In order to facilitate the replacement of windows, the photolysis cell body was made of 2.3 cm i.d. pyrex glass with a #28 O-ring joint on

Table III-1. Laser conditions for MPD experiments

	Focal Length (cm)	Laser Energy (J/pulse)	Fluence (J/cm^2)	Power Density (GW/cm^2)
Wavelength Dependence				
D_2CO	15	1.0	160	0.8
HDCO	25	1.2	120	0.6
H_2CO	25	1.2	120	0.6
Pressure Dependence				
975.9 cm^{-1}	25	1.7	175	0.9
1039.4 cm^{-1}	15	1.8	290	1.4
Infrared Fluorescence	25	1.3	133	0.67
Branching Ratio				
Normal Intensity	25	1.25	125	0.65
High Intensity	25	1.9	195	1.0
Buffer Gas	15	1.25	200	1.0
Radical Scrambling	25	1.5	150	0.75

each end. Interchangeable window mounts were of similar i.d. with a #28 O-ring joint at one end. The other end was cut at Brewster's angle and sealed with a polished NaCl window epoxied (Eccobond 45) in place. The cells were 44 cm long, close to the minimum that could be used without damage to the windows. All cells had a sidearm that could be closed off with a stopcock in order to isolate condensable materials. Gas handling was performed on a glass and grease vacuum line with a base pressure of $\sim 1 \times 10^{-6}$ Torr. Pressures were measured with a Celesco pressure transducer calibrated against a Hg manometer and with an MKS Baratron capacitance manometer (Model 145 AH-10).

The procedure for a photolysis was to fill a cell with the appropriate pressure of formaldehyde and freeze it into the sidearm. In all branching ratio and wavelength dependence experiments, 8 Torr of D_2CO was used. When radical yields were to be measured, NO was added to the cell. The measured NO pressure was decreased by 2% to correct for the volume of the sidearm. If a buffer gas was used, it was added after the NO was frozen down in the sidearm and the cell pumped out. Correction was made for the loss of NO due to its finite vapor pressure of ~0.1 Torr over LN_2. The absolute NO pressure was not critical in these cases so long as it was consistent in all buffer gas experiments. Krypton pressures greater than 20 Torr could not be used since dielectric breakdown occurred in the cell at the focus. Higher pressures of Ar could be used but it does not condense at 77 K and severely interfered with G.C. analysis of the products. Another radical scavenger, isobutene was once added to the photolysis cell in an attempt to scavenge D atoms. Visible fluorescence was observed in the focal region indicating dissociation of the isobutene was occurring and no analysis was performed.

Photolyses were typically 2700-3600 shots in duration at a repetition rate of 1 Hz. The average laser power was constantly monitored by a Scientech power meter and maintained constant to within ±15% over the course of a photolysis. After photolysis, the cell was returned to the vacuum line and all condensable materials frozen into the sidearm with LN_2. Non-condensables were then frozen into a transfer loop[9] with liquid helium and analyzed by gas chromatography or mass spectroscopy. In the wavelength dependence experiments, non-condensable products were measured by the pressure rise in the vacuum line when the cell was opened. Results obtained in this fashion agreed with G.C. analysis of the same photolysis to ±3%. Both techniques were calibrated with samples containing known pressures of D_2 and CO. The uncertainty in the absolute D_2 and CO yields measured by G.C. analysis were <3%. The G.C. calibration was linear in the 0.05-0.7 μmole range used (Fig. III-2).

G. C. analyses were performed on a Varian 3600 gas chromatograph equipped with a 1/4 in o.d. x 15 ft long column of standard Cu tubing packed with MS5A, 50/60 mesh (Analabs). The reference column was an empty Cu tube. He carrier gas flow rates were 40 ml/min for each column. The thermal conductivity detector was operated at 150°C with the filament at 230°C having a current of 257 mA. The column was temperature programmed to rise from an initial temperature of 40°C maintained for 20 minutes, to 70°C at a rate of 10° per minute. The peaks were recorded on a strip chart recorder (Linear) and integrated with a planimeter (Burrell). A typical G.C. trace is shown in Figure III-3. Mass spectral analyses were performed on an AEI MS-10 mass spectrometer. Several electron voltages were used. Infrared spectra were recorded on a Nicolet Model 7199 FTIR.

Figure III-2. G.C. calibration curves for D_2 and CO.

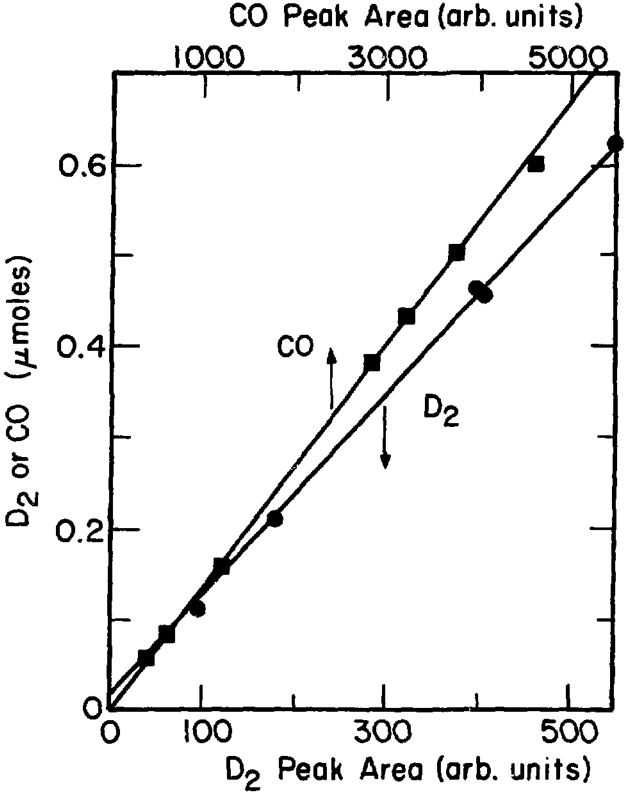
CO Peak Area (arb. units)
1000
3000
5000
0.6
0.4
0.2
0
D2 or CO (µmoles)
CO
D2
0
100
300
500
D2 Peak Area (arb. units)

XBL 811-7509

Figure III-3. Typical G.C. trace of D_2CO photolysis products with 7 Torr NO used. The N_2 peak results from the reaction of DNO radicals. NO appears at 65 min. Temperature rises at 10°C/min for 3 minutes, 25 min after injection.

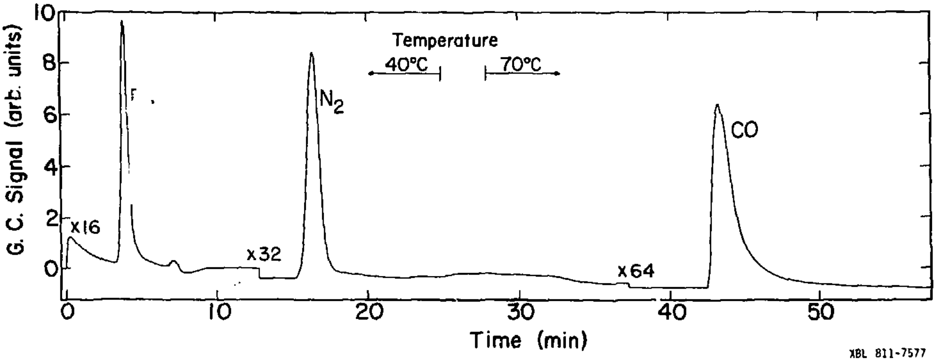
G. C. Signal (arb. units)
10
8
6
4
2
0
Time (min)
0
10
20
30
40
50
Temperature
40°C
70°C
x16
x32
x64
N$_2$
CO

XBL 811-7577

The cell used for viewing IR fluorescence was similar to the photolysis cell however it was 30 cm long and had 2.0 cm diameter CaF_2 viewing windows positioned above and below the focus of the laser beam. Infrared fluorescence was viewed through the following filters cooled to 77 K in the filter wheel inside the detector dewar: At 5 μm, N 4701-9, with peak transmission of 64% at 2130 cm^{-1}, 10% power points at 2060 and 2197 cm^{-1}, 1% power points at 2026 and 2215 cm^{-1}. In the 6-7 μm range, either N 6017-8, with peak transmission of 78% at 1668 cm^{-1}; 10% power points at 1630 and 1703 cm^{-1}, 1% power points at 1622 and 1710 cm^{-1}, or L5030-9 with an open-band transmittance of 86%, 1 and 10% power cut-on points at 2000 and 1975 cm^{-1} respectively, used with an external CaF_2 window. All filters were obtained from OCLI. The CO gas filter cell used was 4 cm long with CaF_2 windows and filled with 700 Torr CO. Multiple exponential decays were analyzed by first fitting the longest time decay, extrapolating to zero time and subtracting this contribution from the decay curve. This process was repeated on the resulting curve working back to the fastest decay time.

The formaldehydes used were prepared from the appropriate polymers, H_2CO (Matheson, Coleman and Bell), HDCO and D_2CO (Merck, Sharpe and Dohme, each 98 atom % D) as described elsewhere.[5,6,9] Nitric oxide (Matheson) was purified[10] by passage through silica gel at 195 K and degassed at 77 K. Kr (J. T. Baker) was purified by repeated freeze-pump-thaw cycles. Ar and CO (Matheson Research Grade) and D_2 (Matheson C. P., >99.5%) were all used without further purification.

C. Wavelength Dependence

MPD of formaldehyde in the 900-1100 cm^{-1} range is restricted for all practical purposes to its deuterated isotopes. The best overlaps with

CO_2 laser lines occur in the ν_4 (938 cm^{-1}) out-of-plane bending mode and the ν_6 (990 cm^{-1}) C-D wagging mode of D_2CO. These modes are strongly coupled by Coriolis interactions[11,12] with $\xi^a_{64} = 4.54$ cm^{-1}. These modes produce a 200 cm^{-1} wide band of overlapping spectral lines. High resolutions IR spectra[13] show approximately 10 lines/cm^{-1} in this region. The ν_4 (1059 cm^{-1}) and ν_6 (1027 cm^{-1}) modes of HDCO can also be excited by a CO_2 laser. Only weak vibration-rotation lines from these modes in H_2CO extend into this wavelength region. Evans et al[3] have achieved dissociation of H_2CO using a focused DF laser near 2800 cm^{-1}.

The MPD yield of D_2CO per pulse, $\bar{Y}$ vs excitation wavelength is shown along with the fundamental IR spectrum in the ranges 935-990 and 1035-1060 cm^{-1} in Figure III-4. The MPD yield spectrum does not display a smooth wavelength dependence[14-17] across the absorption band producing a single broad maximum as seen in larger molecules such as SF_6, despite the high intensity of 800 MW/cm^2. The resolution of features seen in the MPD yield spectrum are limited by the discrete tunability of the CO_2 laser and power broadening of $\omega_R = \frac{\mu \cdot E}{\hbar} = 2$ cm^{-1}. The transition dipole moment of $\mu = 4 \times 10^{-20}$ esu cm was estimated as $(\nu_D/\nu_H)\ \mu_{H_2CO}$ where μ_{H_2CO} was obtained from integrated absorption measurements[18] on H_2CO.

The enhancement of the yield at individual frequencies shows no striking correlation between peaks in the IR absorption spectrum at either one or two times the laser frequency. Due to power broadening, it may instead be important to consider the total integrated intensity in a bandwidth $\Delta\omega = \omega_R = 2$ cm^{-1}, centered at the laser frequency or some multiple of the laser frequency, in order to explain variations in the yield spectrum. These variations may not be due to just the wavelength dependence of the absorption of the first one or two photons. Since D_2CO behaves

Figure III-4. Wavelength dependence of MPD yield of 8 Torr of D_2CO and laser fluence ≈ 160 J/cm^2 along with the infrared spectrum of 15 Torr D_2CO at 0.1 cm^{-1} resolution. Note different transmittance scales.

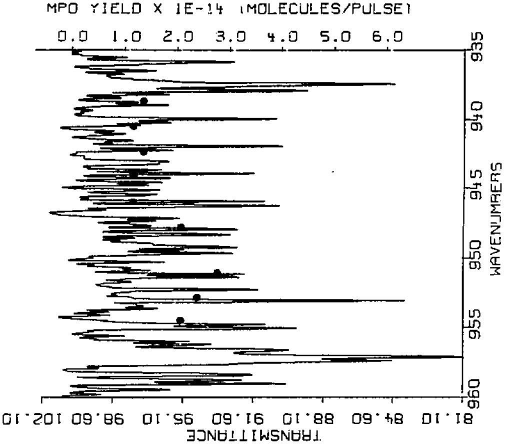
MPO YIELD X 1E-14 (MOLECULES/PULSE)
0.0
1.0
2.0
3.0
4.0
5.0
6.0
935
940
945
950
955
960
WAVENUMBERS
TRANSMITTANCE
81.10
84.60
88.10
91.60
95.10
98.60
102.10

XBL 811-7584

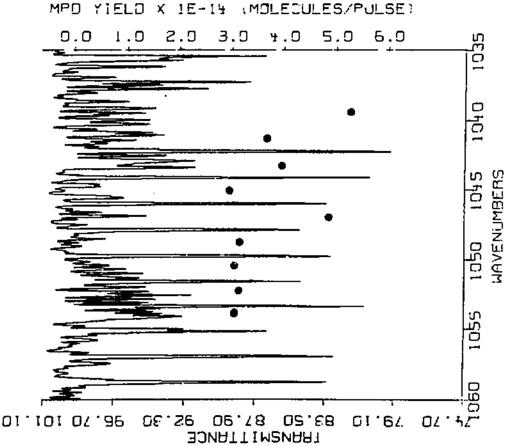
MPO YIELD X 1E-14 (MOLECULES/PULSE)
0.0
1.0
2.0
3.0
4.0
5.0
6.0
1035
1040
1045
1050
1055
1060
WAVENUMBERS
TRANSMITTANCE
74.70
79.10
83.50
87.90
92.30
96.70
101.10

as a small molecule in regard to MPD, the QC begins at relatively high energies (see Sec. IV-B.2) due to the low density of vibrational states. Finding a ladder of vibration-rotation states allowed by dipole selection rules and spaced by multiples of the energy of a laser photon is difficult due to the paucity of levels. The asymmetric rotor nature of formaldehyde adds somewhat to the irregularity of the spacing. The diagonal anharmonicity of the ν_4 mode is[19] about 3 cm^{-1}. Coincidences of levels that provide all or part of such a ladder permitting excitation to the QC and dissociation can lead to sharp features in the MPD yield spectrum. Climbing up such a ladder of energy levels in D_2CO requires collisions (see next section) to change energy levels or move to another ladder in order to overcome energy mismatches which act as bottlenecks to excitation. Since several ladders of a few photons each may be required to reach the QC, dramatic resonance effects may, to some extent, be washed out and cannot be expected to be closely related to the IR absorption spectrum from the ground state.

The concept of going up several steps on one ladder before reaching a bottleneck and switching to another ladder is supported by experiments by Evans *et al.*[3] They found that a DF laser operating on several lines gave a factor of about 100 increase in MPD yield compared to operation with the same total energy in a single line. The availability of several pumping frequencies makes many ladders accessible and eases the bottlenecking problems.

An enhancement of the dissociation yield is seen for excitation near 1040 cm^{-1} relative to that at 940 cm^{-1}. This is contrary to the usual red shift of the yield spectrum from the fundamental absorption in collisionless MPD. Some sharper peaks are seen in the ν_6 region but the total absorption strengths of the ν_4 and ν_6 modes are comparable. The yield enhancement can be attributed to the location of the C-D stretching modes in D_2CO. The C-D stretch absorption band extends from 2000-2275 cm^{-1} (Fig. III-5). With excitation at 940 cm^{-1}, two photons bring the molecule to 1880 cm^{-1} well below these levels. The second photon from irradiation at 1040 cm^{-1} leaves the molecule at 2080 cm^{-1} in the heart of the C-D stretching levels. These levels can borrow intensity via Fermi resonance from the bending overtone levels establishing a denser manifold of acceptable final states for a dipole allowed transition. This added density of states can ease energy mismatches resulting in more available excitation pathways and an onset of the QC at lower energy, leading to increased dissociation yields. HDCO dissociation yield (Table III-2) is also greater in the 1040 cm^{-1} region than near 940 cm^{-1} for the few frequencies used, but this may just be due to stronger absorption in the former region. H_2CO shows minimal dissociation even under maximum fluence conditions at the wavelength providing the best overlap of CO_2 laser line and H_2CO rotational line.

The power dependence of formaldehyde MPD has been measured by Koren _et al._[20] The set of points at different intensities in Table III-2 show similarly that in these experiments, D_2CO dissociation has an approximately cubic power dependence while HDCO displays an I^5 behavior. Additional confirmation of this behavior in D_2CO is seen in Section F of this chapter.

Figure III-5. C-D stretching region of the D_2CO IR spectrum. D_2CO pressure = 8 Torr, resolution = 0.1 cm^{-1}.

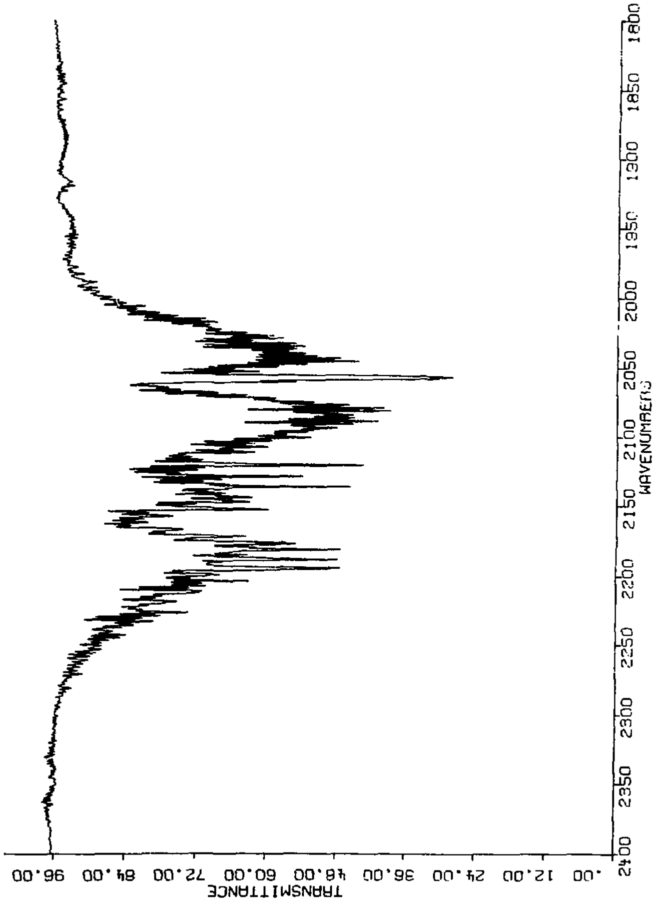
TRANSMITTANCE
.00
12.00
24.00
36.00
48.00
60.00
72.00
84.00
96.00
WAVENUMBERS
2400
2350
2300
2250
2200
2150
2100
2050
2000
1950
1900
1850
1800

XBL 811-7583

Table III-2. Wavelength dependence of formaldehyde MPD yield

CO_2 Laser Line	Frequency (cm^{-1})	$\bar{Y}$ (molecules/pulse)
	D_2CO[a]	
00°1-02°0		
R(20)	1078.6	3.5×10^{14}
P(12)	1053.9	3.1
P(14)	1052.2	3.2
P(16)	1050.4	3.1
P(18)	1048.7	3.2
P(20)	1046.9	4.9
P(22)	1045.0	3.0
P(24)	1043.2	4.0
P(26)	1041.3	3.7
P(28)	1039.4	5.3
00°1-10°0		
R(20)	975.9	2.2×10^{14}
P(08)	954.5	2.1
P(10)	952.9	2.4
P(12)	951.2	2.8
P(14)	949.5	2.0
P(16)	947.7	2.1
P(18)	946.0	2.1
P(20)	944.2	1.2
P(22)	942.4	1.4
P(24)	940.5	1.2
P(26)	938.7	1.4
	D_2CO[b]	
00°1-02°0		
P(18)[c]	1048.7	3.8×10^{14}
P(18)[d]	1048.7	7.1×10^{13}

continued

Table III-2 (continued)

CO_2 Laser Line	Frequency (cm^{-1})	$\bar{Y}$ (molecules/pulse)
	$HDCO^b$	
00°1-02°0		
P(18)[c]	1048.7	3.4×10^{14}
P(18)	1048.7	3.8×10^{13}
P(20)	1046.9	3.0×10^{13}
00°1-00°1		
P(18)	946.0	6.7×10^{12}
	H_2CO^b	
00°1-02°0		
R(22)	1079.9	$< 10^{12}$
R(16)	1076.0	$< 10^{12}$
R(14)	1074.6	$< 10^{12}$
R(12)	1073.3	$< 10^{12}$
R(12)[c]	1073.3	$< 10^{12}$
00°1-10°0		
R(22)[c]	977.2	$< 10^{12}$

---

[a] D_2CO pressure = 8 Torr, 25 cm focal length lens, incident energy = 1.0 J/pulse.

[b] Formaldehyde pressure = 8 Torr, 15 cm focal length lens, incident energy = 1.2 J/pulse.

[c] Incident energy = 1.9 J/pulse.

[d] Incident energy = 1.1 J/pulse.

D. Pressure Dependence

The dependence of MPD-yield on D_2CO pressure was studied in the range from 1-10 Torr at two laser frequencies (Figs. III-6,7). The dissociation yield is proportional to $P_{D_2CO}^{3.25\pm0.35}$ at 975.9 cm^{-1} and $P_{D_2CO}^{3.0\pm0.3}$ at 1039.4 cm^{-1}. Koren et al.[20] observed a $P_{D_2CO}^{2.3}$ behavior in this pressure range at 944.2 cm^{-1} however, they worked under significantly more strongly focused conditions and a power density of 16 GW/cm^2. Evans et al[3] saw an approximately square dependence on H_2CO pressure using DF laser excitation. These large pressure dependences are in direct contrast to the case of collisionless MPD in SF_6 where dissociation yield decreases with increasing pressure.[1] The necessity of collisions for MPD in D_2CO indicates the difficulty of excitation to the QC. Two important questions to consider are: at what level of excitation does this bottleneck occur and how do collisions aid in MPD of D_2CO? The results of this and the following section will address these questions.

The addition of 15 Torr of NO to the photolysis cell increased the dissociation yield but reduced the yield dependence on D_2CO pressure to $P_{D_2CO}^{1.7}$ (Fig. III-6). This is presumably due to rotational relaxation of D_2CO by collisions with NO. By redistributing population among J, K states in D_2CO bottlenecks to higher excitation arising from energy mismatches between the laser frequency and the allowed transitions from a particular J, K state can be overcome. The large dependence on D_2CO pressure that remains indicates that D_2CO-D_2CO collisions play an important role in the excitation process in formaldehyde. The exact nature of the collisional processes will be discussed in more detail in the next section in conjunction with the IR fluorescence data.

Figure III-6. The pressure dependence of the CO yield produced by MPD of D_2CO at 975.9 cm^{-1}. The laser energy was 1.7 J/pulse and the fluence was 175 J/cm^2. Least squares fits give slopes for pure D_2CO = 3.25; and for D_2CO + 15 Torr NO = 1.7. Products were analyzed by G.C.

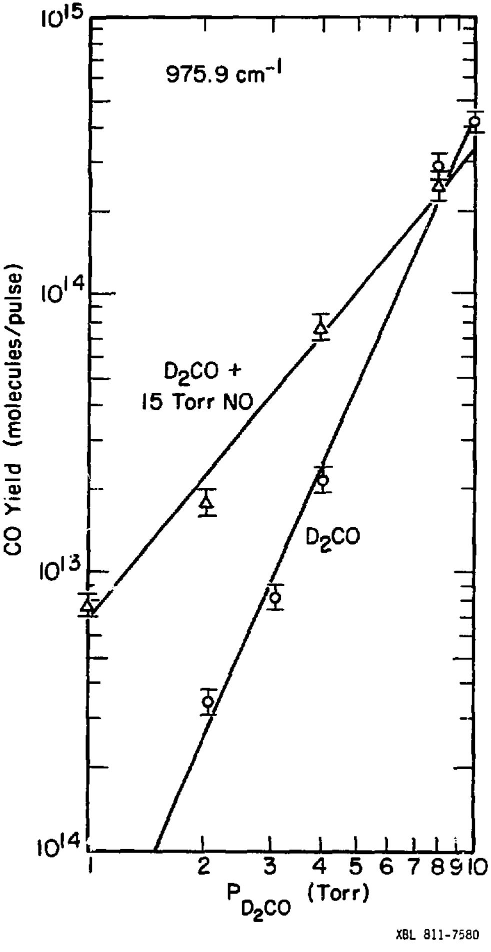
975.9 cm⁻¹
CO Yield (molecules/pulse)
10¹⁵
10¹⁴
10¹³
10¹⁴
D₂CO +
15 Torr NO
D₂CO
1
2
3
4
5
6
7
8
9
10
P_D₂CO (Torr)

XBL 811-7580

Figure III-7. The pressure dependence of CO and D_2 yield produced by MPD of pure D_2CO at 1039.4 cm^{-1}. Laser energy was 1.8 J/pulse and the fluence was 290 J/cm^2. A least squares fit gives a slope = 3.0. Products were analyzed by pressure rise. The yield plotted is one half the total pressure rise.

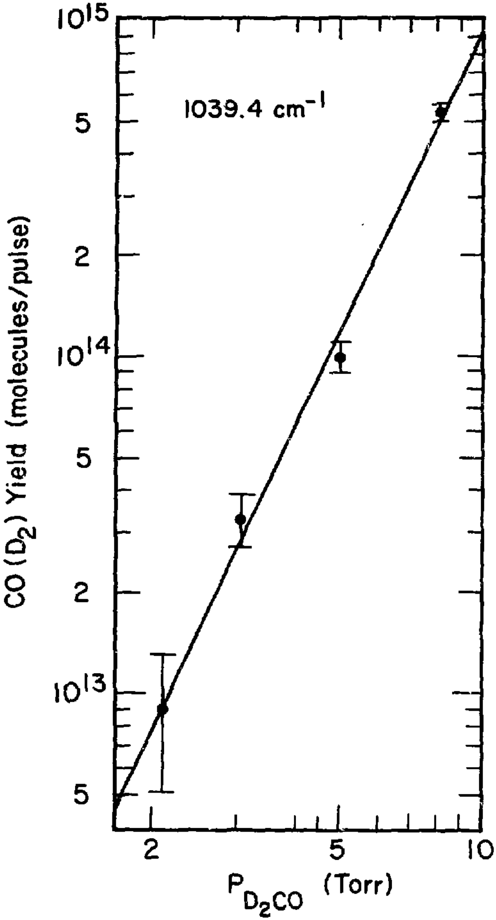

10^{15}
5
2
10^{14}
5
2
10^{13}
5
1039.4 cm^{-1}
CO (D$_2$) Yield (molecules/pulse)
2
5
10
P_{D_2CO} (Torr)

XBL 811-7574

E. Infrared Fluorescence

Infrared fluorescence from C-D and C-O stretches of D_2CO excited at 949.5 cm^{-1} was observed as described in Chapters II and III. In the C-D stretching region, a cold gas filter of ~700 Torr CO was used since molecular CO emits within the bandpass of the filter used. No effect on the decay curve was observed indicating that the fluorescence signal was not due to product CO molecules. The wavelength dependence of the fluorescence intensity was observed on an oscilloscope to be, roughly, similar to the yield spectrum in the 10.6 μm region.

The total fluorescence in the C-D stretching region was proportional to the square of the formaldehyde pressure (Fig. III-8). One factor of pressure comes just from the increase in number density. The second factor of pressure indicates that collisions are required in order to significantly populate v=1 of the stretching mode. This corresponds to slightly more than the energy of two photons in the pumped mode. This implies that there is either very poor intermode coupling, which in itself is detrimental to continued excitation, or that a severe bottleneck to excitation exists at these very low energy levels. In contrast to this square pressure dependence, IR fluorescence from HFCO, a molecule that dissociates much more easily than D_2CO, increases linearly with pressure.[21]

The possibility that the square dependence of fluorescence intensity on pressure arises due to pressure broadening is unlikely since power broadening is on the order of 2 cm^{-1}, while the pressure broadening coefficient[22] for pure H_2CO self-broadening is 1.1×10^{-3} cm^{-1} $Torr^{-1}$, resulting in a 0.01 cm^{-1} linewidth at 8 Torr.

Figure III-8. Peak infrared fluorescence intensity at 5 μm (2060 - 2197 cm^{-1}) from multiphoton excited D_2CO as a function of pressure.[2] Laser fluence = 133 J/cm^2 and frequency = 949.5 cm^{-1}.

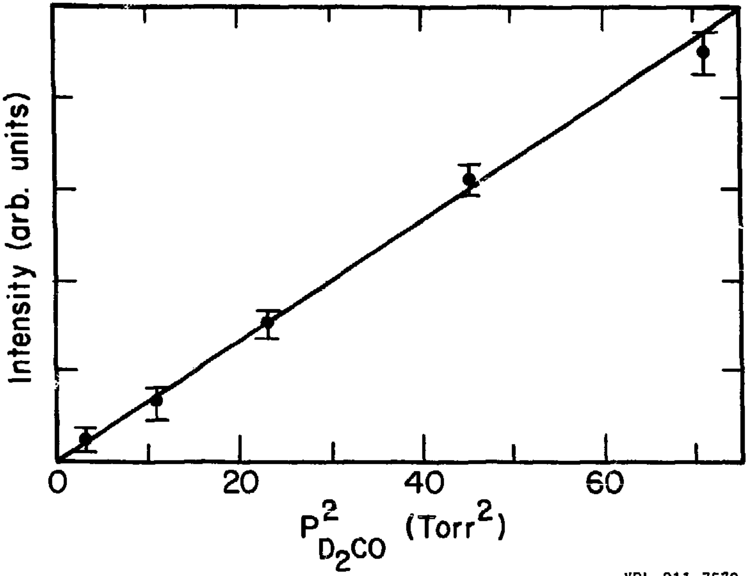

XBL 811-7570

The IR fluorescence from 2.1 Torr of D_2CO was studied as a function of Ar pressure (Fig. III-9). The fluorescence intensity at $P_{Ar} = 0$ in this graph is the fluorescence intensity from 2.1 Torr of pure D_2CO. The fluorescence intensity increased with a less than linear dependence on Ar pressure and this effect was saturated by an Ar pressure of 40 Torr. The time of the peak fluorescence intensity did not change relative to the start of the laser pulse and the fluorescence decay rates remained virtually unchanged as a function of Ar pressure. Thus, the observed saturation of the peak fluorescence intensity with Ar pressure is not due to vibrational deactivation of D_2CO by Ar during the laser pulse. It is shown in Chapter IV using IR fluorescence data, that the average population in a stretching mode of a molecule in the laser focal zone is $\langle n \rangle_s = 0.65$, indicating that the observed IR emission is primarily from $1 \rightarrow 0$ transitions.

At an Ar pressure of 50 Torr, rotational relaxation is for the most part complete, yet the fluorescence intensity is still proportional to the square of the D_2CO pressure (Fig. III-10). Thus, $D_2CO - D_2CO$ self-collisions appear to be necessary for populating the C-D stretching levels and overcoming excitation bottlenecks at low energies. The increasing fluorescence intensity with increasing Ar pressure is presumably due to rotational relaxation which, in the v=0 level, permits more molecules to absorb by filling in the hole in the rotational population distribution created by the loss, by absorption, of molecules in the rotational states that have allowed transitions at the laser frequency. The molecules excited to v=1 will all be in the particular J, K states determined by the allowed transitions at the laser frequency from v=0. The probability of transitions from these particular states, however, may be small.

Figure III-9. Peak infrared fluorescence intensity at 5 μm from 2.1 Torr of D_2CO as a function of added Ar pressure. Laser fluence ≈ 133 J/cm^2 and frequency = 949.5 cm^{-1}.

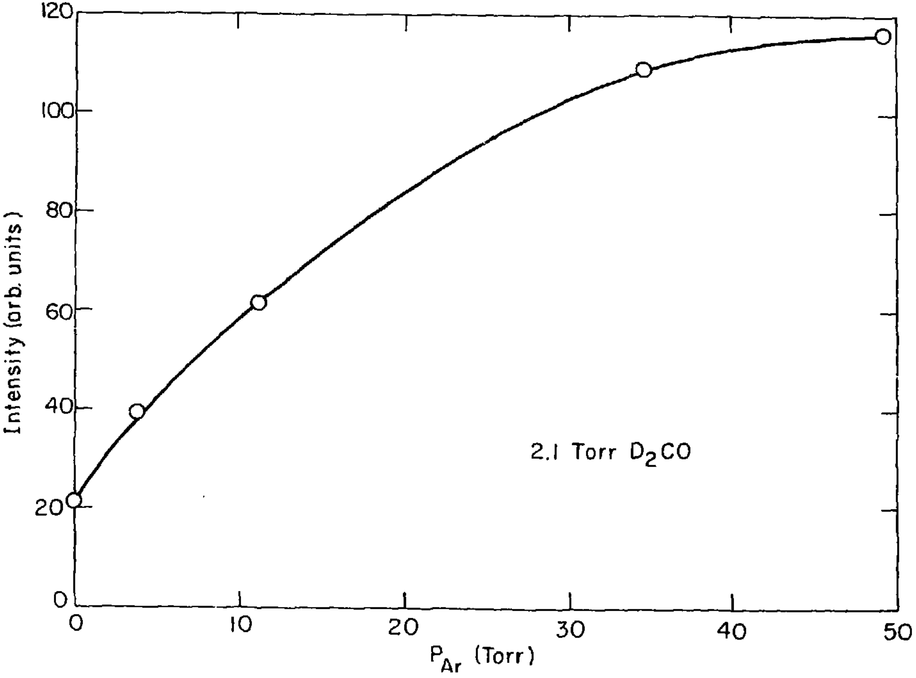
Intensity (arb. units)
120
100
80
60
40
20
0
0
10
20
30
40
50
P_{Ar} (Torr)
2.1 Torr D_2CO

XBL 811-5053

Figure III-10. Peak infrared fluorescence intensity at 5 μm from D_2CO vs D_2CO pressure^2 with 50 Torr Ar added. Laser fluence = 133 J/cm^2 and frequency = 949.5 cm^{-1}.

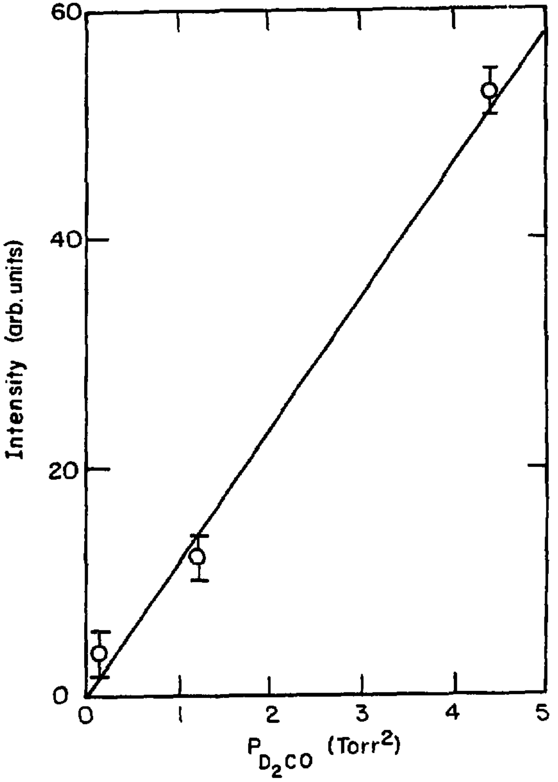

XBL811-5052

Rotational relaxation in the v=1 state distributes the population into many J, K states facilitating continued absorption to v=2 and higher vibrational levels.

We can now consider the following mechanism that provides a kinetic scheme to explain the observed pressure dependence of IR fluorescence and MPD yield:

$$\left\{\begin{array}{l} D_2CO\ (v=0;\ J,\ K) + h\nu \rightarrow D_2CO\ (v=1;\ J',\ K') \\ D_2CO\ (v=0;\ J'',\ K'') + M \rightarrow D_2CO\ (v=0;\ J,\ K) + M \end{array}\right\} \qquad \begin{array}{r} (1) \\ (2) \end{array}$$

$$\left\{\begin{array}{l} D_2CO\ (v=1;\ J',K') + M \rightarrow D_2CO\ (v=1;\ J''',\ K''') + M \\ D_2CO\ (v=1;\ J''',\ K''') + h\nu \rightarrow D_2CO\ (v=2) \\ D_2CO\ (v=1) + D_2CO\ (v=1) \rightarrow D_2CO\ (v=2) + D_2CO\ (v=0) \end{array}\right\} \qquad \begin{array}{r} (3) \\ (4) \\ (5) \end{array}$$

$$\left\{\begin{array}{l} D_2CO\ (v=2) + nh\nu \rightarrow D_2CO\ (QC) \\ D_2CO\ (v=2) + M + n'h\nu \rightarrow D_2CO\ (QC) \end{array}\right\} \qquad \begin{array}{r} (6) \\ (7) \end{array}$$

$$D_2CO\ (QC) + n''h\nu \rightarrow \left\{\begin{array}{l} D_2 + CO \\ D + DCO. \end{array}\right. \qquad (8)$$

After the absorption of one photon, vibrational uppumping from D_2CO - D_2CO collisions or rotational relaxation in v=1 permits molecules to overcome an excitation bottleneck and reach v=2. Collisions with D_2CO may be more efficient at achieving rotational relaxation in D_2CO than are collisions with Ar, contributing to the strong dependence of MPD yield and IR fluorescence on D_2CO pressure. Rotational relaxation in v=0 fills in the hole in the rotational population distribution enabling more molecules to absorb. Such rotational relaxation and vibrational energy transfer processes may also occur at higher levels of excitation in the discrete state region. The ordering of these processes in unimportant. Bottlenecks to excitation due to energy mismatches between the photon energy and the energy for an allowed transition from a given vibration-rotation state can also be overcome by rotational relaxation. Molecules in a particular v; J, K state which has no allowed transitions at energy hν can be collisionally transferred to a nearby state v; J', K', from which further absorption is possible. Processes such as

$$D_2CO\ (v=m;\ J,\ K) + M \rightarrow D_2CO\ (v=m;\ J',\ K') + M$$

$$D_2CO\ (v=m;\ J',\ K') + n'h\nu \rightarrow D_2CO\ (QC)$$

may contribute to the pressure dependence of the MPD yield. Multiphoton transitions and collisionally induced intramolecular vibrational energy transfer to populate the stretching modes can also contribute to excitation in the discrete state region. Once in the QC, absorption can proceed without the assistance of collisions.

The proposed mechanism employing rotational relaxation and vibrational energy transfer results in a complicated pressure dependence for the dissociation yield determined by the contribution of each possible excitation step. The dependence on rotational relaxation collision partner is determined by the ratio of the IR pumping rate to the rotational relaxation rate and the number of bottlenecks that must be overcome by rotational relaxation in the discrete state region. If we consider, for example, an excitation scheme defined by (1), (2), (5), (6) and (8), the rate of product formation is

$$\begin{aligned}\frac{d[\text{products}]}{dt} &\propto [D_2CO\ (QC)]\\ &\propto [D_2CO\ (v=1)]^2\\ &\propto [D_2CO]^2[M]^a\end{aligned}$$

where a is determined by the need for and the efficiency of rotational relaxation. This predicts a square dependence of MPD yield on D_2CO pressure when another collision partner is present, similar to that observed when 15 Torr of NO is added to the cell. When no foreign gas is added, D_2CO provides all of the rotational relaxation as well as vibrational energy transfer and a near cubic dependence on D_2CO is observed.

The square pressure dependence of the dissociation yield observed by Evans <u>et al</u>.[3] in H_2CO could result from their needing fewer photons to reach the QC (photon energy = 2800 cm^{-1}), reducing the need for collisional processes in the discrete state region. Pressure dependence studies in that system using single-line and multi-line excitation in the presence of another collision partner would be useful to identify the contributions from vibrational energy transfer and rotational relaxation.

IR fluorescence from D_2CO was also observed under unfocused conditions with a 1.0 cm diameter beam in order to obtain vibrational relaxation rates. A typical fluorescence trace is shown in Figure III-11. A multi-exponential decay was observed which was satisfactorily analyzed as a double exponential over 2 decades. The amplitude of the slower decay increased relative to that of the faster decay at higher pressures (Fig. III-12) and at higher laser powers. The identity of the decay channels are not known. The fast decay had a value of $p\tau = 7.8 \pm 0.7$ μs Torr (Fig. III-13) and the slow decay of $p\tau = 115.4 \pm 2.9$ μs Torr (Fig. III-14). It was imperative to carefully subtract the longer time component when analyzing the fast decay in order to get reasonable and consistent values of τ.

Figure III-11. Fluorescence trace of 5 μm fluorescence from 6.6 Torr of D_2CO excited by an unfocused CO_2 laser with an energy of 1.2 J/pulse at 949.5 cm^{-1}.

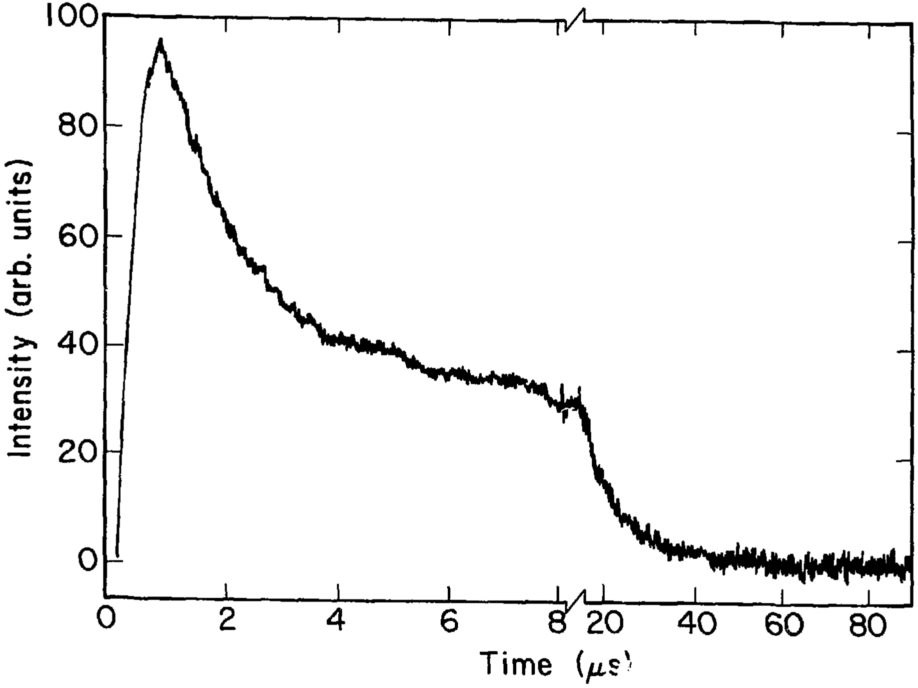

XBL 811-7510

Figure III-12. Amplitude ratio of fast and slow components of 5 um IR fluorescence from unfocused CO_2 laser excited D_2CO vs D_2CO pressure. The laser energy was 1.2 J/pulse and the frequency was 949.5 cm^{-1}.

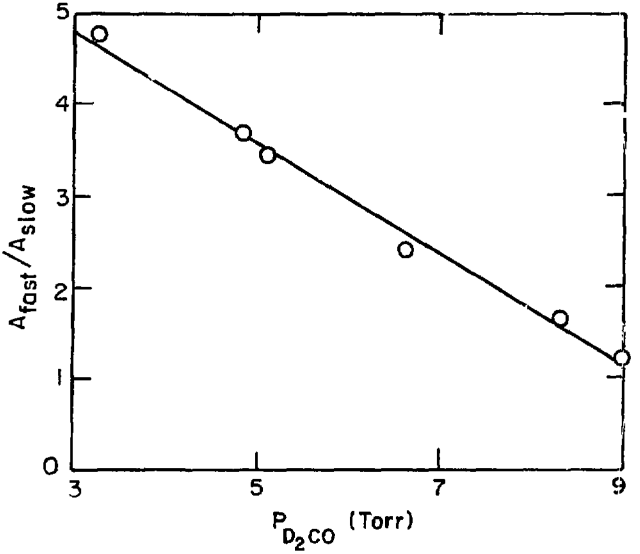

XBL 811-5051

Figure III-13. [illegible]ay time of fast component of 5 μm infrared fluorescence from D_2CO excited by an unfocused CO_2 laser vs D_2CO pressure. The laser energy was 1.2 J/pulse and the frequency = 949.5 cm^{-1}. The slope gives $(p\tau)^{-1}$ = 0.128 μs^{-1} $Torr^{-1}$.

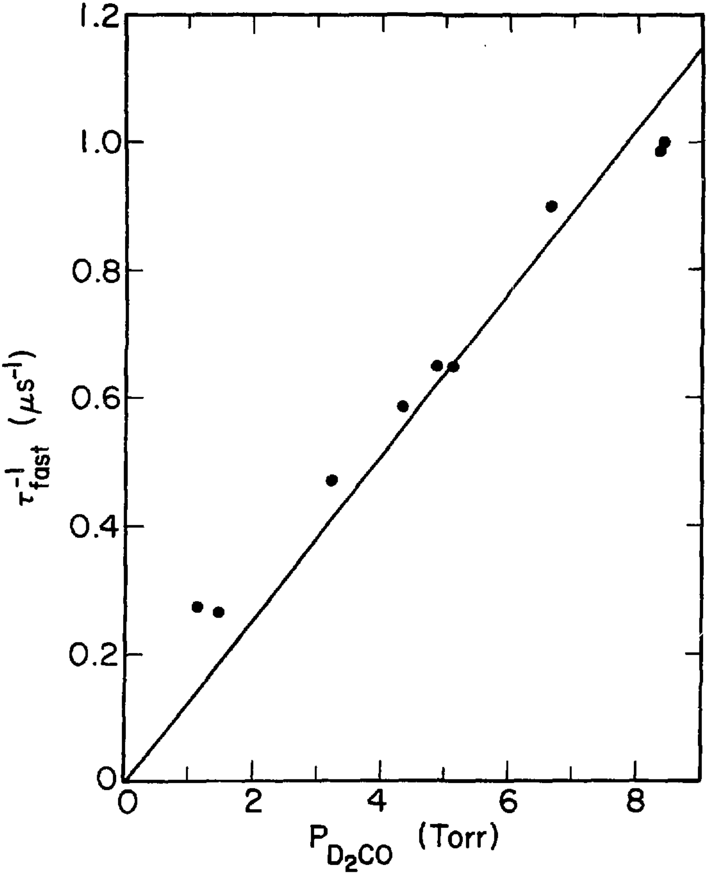

XBL 811-7576

Figure III-14. Inverse decay time of slow component of 5 μm infrared fluorescence from D_2CO excited by an unfocused CO_2 laser vs D_2CO pressure. The laser energy was 1.2 J/pulse and the frequency = 949.5 cm^{-1}. The slope gives $(p\tau)^{-1}$ = 0.00867 μs^{-1} $Torr^{-1}$.

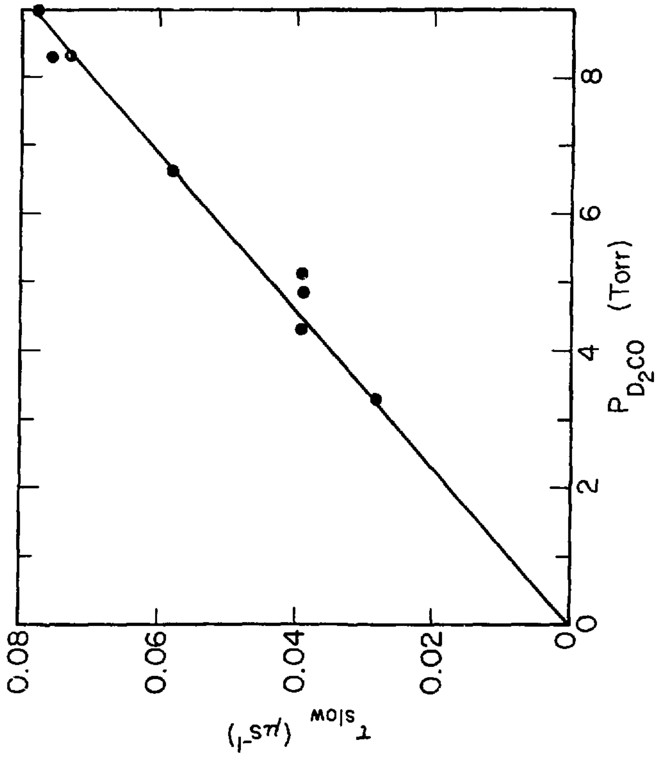

XBL 811-7506

Under focused conditions a long time tail is observed with $\tau = 215$ μs (Figs. III-15,16). This lifetime corresponds to heat transport processes, cooling of the thermally heated gas. The amplitude of this tail extrapolated back to zero time is 1/6 that of the peak fluorescence intensity. This intercept represents the amplitude of the fluorescence arising from purely thermal excitation at the maximum thermal temperature achieved. This value will be used to estimate that temperature in Chapter IV.

F. Branching Ratio

1. Introduction

Both the thermal chemistry[23-27] and UV photochemistry[5,6,9,28-31] of formaldehyde have been extensively studied over the past 50 years. The importance of formaldehyde chemistry is clear from its role in combustion processes[32,33] and atmospheric chemistry.[34] Furthermore, formaldehyde serves as a model for the photochemistry and photophysics of small polyatomic molecules. The primary steps of formaldehyde photochemistry in the near UV have been identified[5,6] as dissociation to molecular and radical products:

$$H_2CO\ (S_0) + h\nu \rightarrow H_2CO\ (S_1) \tag{9}$$

$$H_2CO\ (S_1) \rightarrow H_2CO\ (I) \rightarrow H_2 + CO \tag{10}$$

$$H_2CO\ (S_1) \rightarrow H + HCO \tag{11}$$

Dissociation to molecular products at formaldehyde pressures greater than 0.1 Torr takes place after S_1 decays to an as yet unidentified intermediate state, I. The role of I in radical dissociation is undetermined. IR excitation enhances the UV work by probing the high vibrational states of S_0 which have been proposed[5] as a candidate for I and are directly populated during MPE.

Figure II-15. The infrared fluorescence at 5 μm from 8.0 Torr of D_2CO excited by a focused CO_2 laser at 949.5 cm^{-1}. The fluence at the focus was 133 J/cm^2. The baseline is obtained from a similar trace take on a slower time scale. The long time component of the signal is due to thermal cooling.

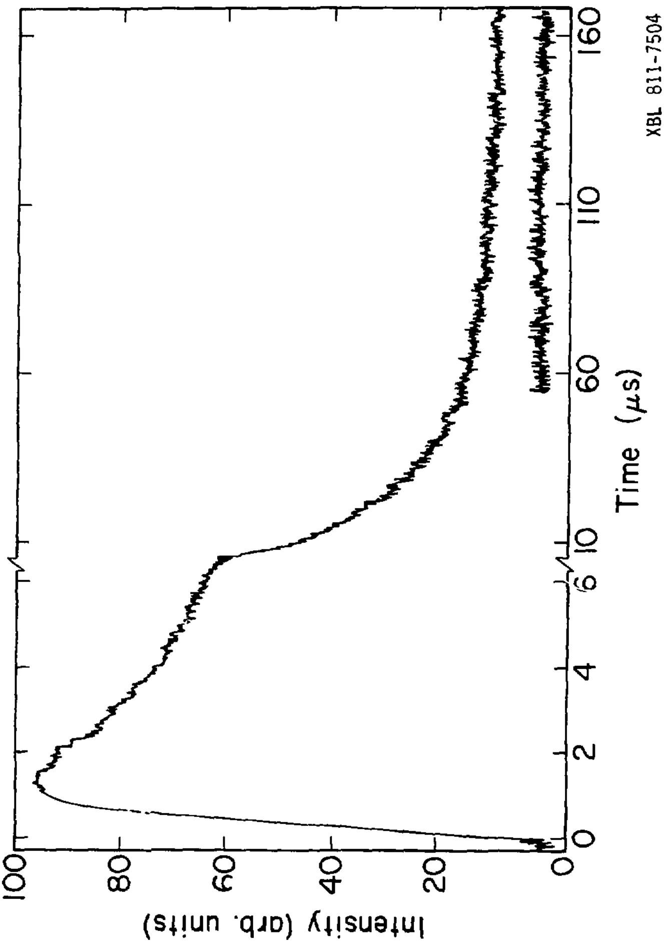

XBL 811-7504

Figure III-16. A semilogarithmic plot of the trace in Figure III-15. The right hand side of the figure is the analysis of the portion of the trace recorded on a slower time scale. The dashed line on the left hand side is the extrapolation of the intensity of the slower decaying components. The amplitude of the long time component extrapolated to time = 0 is 1/6 that of the peak vibrational fluorescence. The decay times are $\tau_f = 2.3$ μs, $\tau_s = 14.2$ μs and $\tau_{thermal} = 215$ μs.

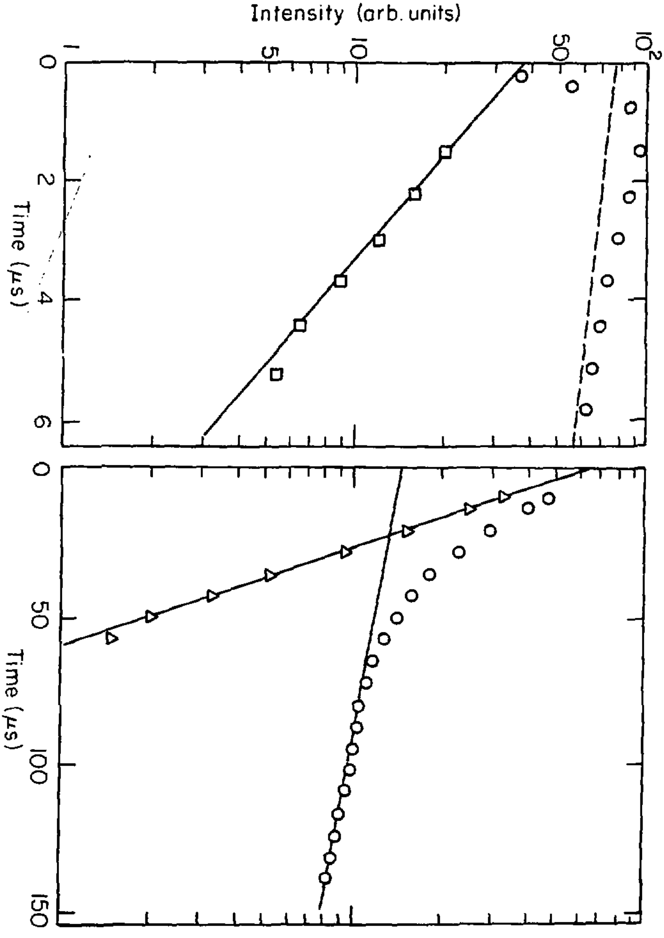
Intensity (arb. units)
10^2
50
10
5
1
0
2
4
6
Time (μs)
0
50
100
150
Time (μs)

XBL 811-5045

In shock tube work,[25-27] the radical pathway (11) has clearly been identfied as a major dissociation route but contributions from molecular dissociation have been questioned.[26] IR MPD provides another means of excitation to explore formaldehyde chemistry on its ground state potential surface. This section is concerned with the branching ratio between radical and molecular dissociation pathways in formaldehyde MPD. In Chapter IV this branching ratio will be used to calculate the barrier height to molecular product formation.

IR MPD in formaldehyde was first observed by Koren et al.[35] On the basis of the large isotope separation achieved in the photolysis of a natural abundance mixture of H_2CO and HDCO they postulated that dissociation is predominantly molecular. In this section a direct measurement of the branching ratio in D_2CO will be discussed. Nitric oxide is used as a radical scavenger to quantitatively reduce the D_2 yield by the amount of radical dissociation.

The primary steps in IR MPD of D_2CO are taken to be dissociation to molecular and radical products

$$D_2CO + nh\nu \rightarrow D_2 + CO \qquad (12)$$

$$D_2CO + nh\nu \rightarrow D + DCO. \qquad (13)$$

Molecular dissociation generates chemically stable products, one D_2 and one CO molecule per dissociation. Dissociation to radical products (13) is followed by a series of competing reactions. The pertinent reactions in formaldehyde - NO mixtures have been well characterized:[6]

$$D + DCO \rightarrow D_2 + CO \qquad (14)$$

$$DCO + DCO \rightarrow D_2CO + CO \qquad (15)$$

$$DCO + NO \rightarrow DNO + CO \tag{16}$$

$$D + D_2CO \rightarrow D_2 + DCO \tag{17}$$

$$D + NO + M \rightarrow DNO + M. \tag{18}$$

At sufficiently high NO pressures, the D atoms and DCO radicals promptly react with NO via (16) and (18). DNO produces no additional D_2[35,37] and is believed to form N_2 and DNO_3 upon reaction with NO. N_2 is observed as a product in photolyses with NO present. Since D atoms are consumed by (18) and produce no D_2, each radical dissociation produces one more CO then D_2. The difference between the CO and D_2 yields thus gives the number of radical dissociations

$$\phi_{CO} - \phi_{D_2} = \phi^R.$$

The total yield is just

$$\phi^T = \phi^M + \phi^R.$$

2. Isotope Effects on Rate Constants

The rate constants for the hydrogen analogs of reactions (14)-(18) have been experimentally determined[38-44] and the best values chosen from Reilly *et al.*[38] and the references therein are listed in Table III-3. In order to analyze the kinetics and normalize the radical yields in the deuterated system, the rate constants for the deuterated species are required. A method for estimating isotope effects on reaction rate constants has been developed by Bigeleisen and co-workers[45] using the formalism of transition state theory. The ratio of rate constants for light isotope 1 and heavy isotope 2 is given by

Table III-3. Rate constants and isotope effects for reactions (14)-(18)

	Reaction	k^H(cm^3/molecule s)	Refs.	$f^{\neq}$	$\frac{U_{2L}}{U_{2L}}$	Γ	$\frac{k^H}{k^D}$	k^D(cm^3/molecule s)
(14)	$D + DCO \rightarrow D_2 + CO$	5.5×10^{-10}	38-41	13.46	1.52	1.91	1.1	5.1×10^{-10}
(15)	$DCO + DCO \rightarrow D_2CO + CO$	6×10^{-11}	38	23.6	1.34	1.49	2.1	2.8×10^{-11}
(16)	$DCO + NO \rightarrow DNO + CO$	1.4×10^{-11}	38	1.76	1.28	1.48	3.4	4.1×10^{-12}
(17)	$D + D_2CO \rightarrow D_2 + DCO$	5×10^{-14}	38	31.3	1.35	1.60	5.6	9×10^{-15}
(18)	$D + NO + M \rightarrow DNO + M$	4.5×10^{-31}[a]	38,42,43	-	-	-	1	4.5×10^{-31}[a]

[a] Units are cm^6/molecule^2 s.

$$\frac{k_1}{k_2} = \frac{f}{f^{\neq}} \frac{U_{1L}}{U_{2L}} \Gamma$$

where for reactant molecules,

$$f = \prod_{i}^{3n-6} \frac{U_{2i}}{U_{1i}} e^{(U_{1i}-U_{2i})} \left(\frac{1-e^{-U_{1i}}}{1-e^{-U_{2i}}} \right)$$

and $U_i = h\nu_i/kT$. For the transition state, $f^{\neq}$ is the same as f except that the product is taken over the 3N-7 bound modes of the transition state. The tunneling correction is given by[45]

$$\Gamma = \frac{1+|U_{1L}^2|/24}{1+|U_{2L}^2|/24}$$

where U_L refers to the frequency of the mode along the reaction coordinate.

In order to apply this technique the vibrational frequencies of the transition state for each isotope are needed. In the absence of a detailed force constant matrix for the transition state, these frequencies can be estimated using the vibrational frequencies of the isolated reactant radicals[46,47] and molecules[48] listed in Table III-4 as a guide. In estimating vibrational frequencies, it is not necessary to accurately predict the imaginary vibrational frequency of the transition state since the ratio of these values for the isotopic species is the quantity of interest. Since this frequency deals entirely with motion along the reaction coordinate, a ratio of scaled stretching frequencies of the isotopes of the ground state molecule for a mode with motion primarily along this coordinate is chosen for this ratio. Although they are for different types of reactions and potential surfaces, these ratios of U_{1L}/U_{2L} used are all within 20% of the value obtained for reaction (3) by extensive

Table III-4. Vibrational frequencies used in calculations (in cm^{-1})

	HCO	DCO	HNO	DNO	H_2CO	D_2CO
ν_1	2488	1937	2716.7	2043	2766.4	2055.8
ν_2	1080.8	847.4	1505	1153.5	1746.1	1700
ν_3	1868.4	1800	1563.3	1547	1500.6	1105.7
ν_4					1167.3	933.8
ν_5					2843.4	2159.7
ν_6					1251.2	990.4
f	5.93		7.70		86.1	
ZPE	2718.6	2292.2	2892.5	2371.8	5820.3[a]	4577.7[a]
ZPE (kcal/mole)	7.8	6.6	8.3	6.8	16.6[a]	13.1[a]
Refs	38.45	38,46	47	47	48	48

---

[a] Calculated including anharmonic correction $ZPE = ZPE_{obs} - \frac{3}{4} \Sigma X_{ii}$ (see Ch IV).

ab initio calculations.[7] The U_{1L}/U_{2L} term is equivalent to $(m_{2L}/m_{1L})^{\frac{1}{2}}$ where m_L is the mass associated with motion along the reaction coordinate.[45] Using the reduced mass of the separating fragments gives values very similar to the ones used.

The magnitude of the imaginary frequency used is important for the tunneling correction. Too large a value of U_L will predict too large a tunneling correction. The tunneling correction is not very large, however, and the ratio that gives Γ should be correct to within 20%.

In reaction (17) consider the D atom approaching formaldehyde along a C-D bond. The reaction products are a D_2 molecule and a DCO radical. The DCO vibrational frequencies are taken as 3 of the 9 frequencies of the transition state. The 3 bending vibrational frequencies of D_2CO and the vibrational frequency of the newly formed D_2 molecule, each scaled by a factor of 0.8 are taken as other frequencies. One additional frequency from a low frequency bending mode is required. This mode will have little effect on the ratio k^H/k^D since the largest effect comes from the $e^{\Delta U}$ term. A large difference in vibrational frequencies between two isotopes occurs in high frequency modes involving large motion of the isotopic atom, C-D stretches for example. The contribution to f from the bending modes is small and a typical value from the other bending modes in this molecule, $f_{bend} = 1.2$ is used. The imaginary vibrational frequency for the reaction coordinate is chosen as 0.81 times the ν_1 C-D stretching frequency of D_2CO. The resulting isotope effect is found to be $k^H/k^D = 5.9$.

The isotope effect for this reaction has been measured experimentally by McNesby *et al.*[44] Their analysis relied on an old value[48] for the rate constant for the reaction $D + H_2 \rightarrow HD + H$. Using a more recent value[50] for this reaction with the data of McNesby brings their measured value of k_{17}^{H} to 5 x 10^{-14} cm^3 $molecule^{-1}$ s^{-1}, now in agreement with that of other workers and gives k_{17}^{D} = 9 x 10^{-15} cm^3 $molecule^{-1}$ s^{-1}. This measured value of k^H/k^D = 5.6 is listed with all of the deuterated rate constants in Table III-3. This value is in surprisingly good agreement with the estimated value for the isotope effect.

For reaction (14), a D atom and a DCO radical reacting to give D_2 and CO, the transition state was taken as the same as for formaldehyde dissociation to molecular products. The frequencies for this transition state have been calculated by Goddard and Schaefer[7] (see Section IV-B). This reaction shows a very small isotope effect, k^H/k^D = 1.1.

For the remaining reactions, the transition state is chosen with reactants approaching such that the bond angles of the products are formed. The formation of new bonds in the products and bond cleavage in the reactants is taken to be partial, but total bond order is conserved. Pauling stated[51] that the force constant is proportional to the bond order, so the vibrational frequency goes as the square root of the bond order as well as decreasing due to the increased mass in the complex. In reaction (16), the C-D bond is taken to have a bond order of 0.65 and a vibrational frequency 0.8 times the normal C-D stretching frequency. The newly formed N-D bond has a bond order of 0.35 and the N-D stretching frequency is 0.6 times that in DNO. The other frequencies used for the transition state are the molecular frequencies scaled by 0.8 except C-O and N-O stretches which are not greatly perturbed in the transition state and are scaled by 0.9. These scaling factors are approximately what was found in calculations by Goddard and Schaefer for reaction (4). The additional vibrational modes are given values of f = 1.05. This predicts

$k^H/k^D = 3.4$ for reaction (16).

For reaction (15), the vibrational frequencies of formaldehyde and the formyl radical are taken as starting points. The C-O stretch of both species and one C-D stretch from the formyl radical are used since they are relatively unperturbed in the transition state. All other vibrational frequencies are scaled by 0.6 with the symmetric stretch of formaldehyde chosen as the reaction coordinate. The three remaining modes of the complex are each taken to have $f = 1.1$. This gives $k^H/k^D = 2.1$. More tightly bound transition states give larger values of $f^{\neq}$ and smaller isotope effects.

When the isotopic species is present only as a free atom in the reactants as in (18), $f = 1$ and if

$$f^{\neq} > \frac{U_{1L}}{U_{2L}} \Gamma ,$$

an inverse isotope effect occurs. This is usually the case for hydrogen so the rate of reaction of deuterium atoms is faster than that for hydrogen. The use of this model to estimate the isotope effect, however, is predicated on the applicability of transition state theory to the reaction in question. Since reaction (18) would be expected to have little or no barrier hence no well defined complex, the use of transition state theory is inappropriate in this case. The hydrogen rate constant for (18) is not well known since the third body can have a large effect on the rate[42,43] but it was never measured with formaldehyde as the collision partner. The value $k^H_{18} = k^D_{18}$ is used here since the atom-radical recombination is fast and small corrections to the rate are not warranted due to the uncertainty of the hydrogen rate. A precise value for this rate is not required so long as the true rate is not a factor of 5 slower than the value used.

3. Kinetics

Another problem that besets the kinetic analysis and the measurement of the branching ratio is determining the radical concentration. Due to the focused geometry, the radical concentration varies throughout the reaction volume. The initial radical concentration determines which reactions dominate the kinetics.

MPD of D_2CO can generate sufficiently large radical concentrations that reaction (14) becomes the major route for the consumption of D and DCO. This reaction yields one D_2 and are CO hence it cannot be differentiated from direct dissociation to molecular products. In order to avoid this complication, one is constrained to work with radical concentrations such that (14) accounts for only a few percent of the total loss of DCO. Figure III-17 shows the competition between (14) and (16) vs NO pressure at several initial radical concentrations calculated using the deuterated rates from Table III-3. Reaction (15) has little effect on the kinetics. At low NO pressures or high radical concentrations, NO does not act as an effective scavenger. Comparison of the fall off at low NO pressure with the observed radical yield (see Sec. III-F.4) indicates that the photolyses produce an average initial radical concentration of $[DCO]_0 = [D]_0$ between (1-5) x 10^{14} radicals/cm^3.

The radical concentration can also be estimated from the dissociation yield and the focal volume. This volume was estimated as head-to-head truncated cones with radius $r_{min} = 0.05$ cm. Since the fluence threshold is not specifically known, r_{max} chosen so that the minimum fluence is 50 J/cm^2, a typical threshold for MPD in small molecules,[2,3] giving $r_{max} = 0.08$ cm. The length of this focal region was measured to be 3.7 cm.

Figure III-17. Fraction of DCO consumed by reaction (16), DCO + NO → DNO + CO, vs reaction (14), D + DCO → D_2 + CO for different initial radical concentrations (in radicals/cm^3) as a function of NO pressure. Rates used are the deuterated rates in Table III-3.

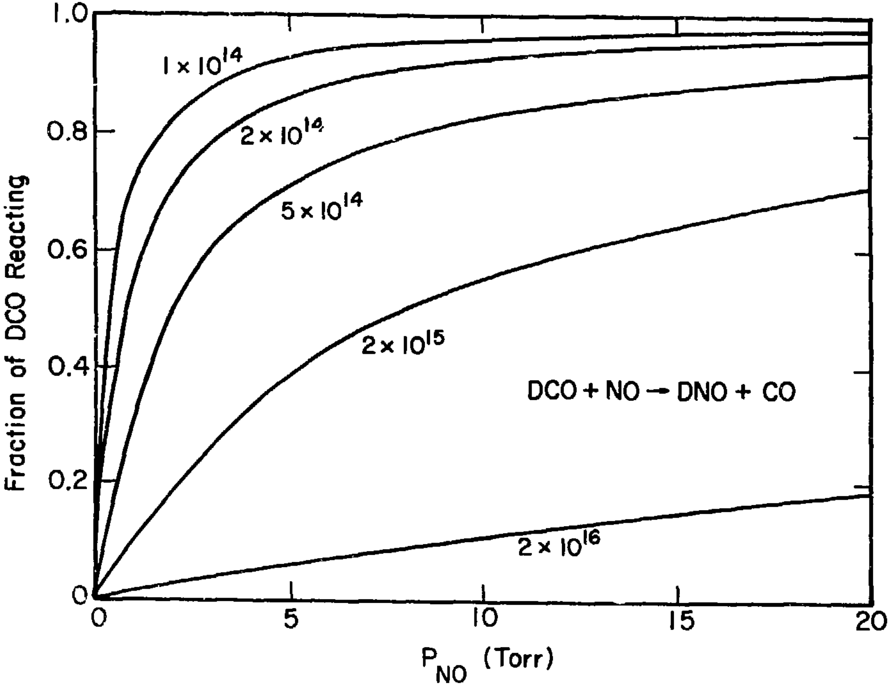
1.0
0.8
0.6
0.4
0.2
0
Fraction of DCO Reacting
0
5
10
15
20
P_{NO} (Torr)
1 × 10^{14}
2 × 10^{14}
5 × 10^{14}
2 × 10^{15}
2 × 10^{16}
DCO + NO → DNO + CO

XBL 811-7581

Using this volume, 0.05 cm^3, and a typical yield of 5 x 10^{13} dissociations per pulse with 10% radical decomposition (see next subsection) gives a radical concentration of 1 x 10^{14} radicals/cm^3.

Since the dissociation yield varies strongly with laser intensity, the radical concentration varies throughout the focal volume. Koren et al.[20] observed an $I^{3.3 \pm 0.2}$ power dependence for MPD of D_2CO and the observations in Sections III-C and F are consistent with that. An effective focal volume can be defined to obtain an average radical concentration by weighting the volume according to this power of the laser intensity. Scaling volume elements by $(I_1/I_o)^{3.3}$ where I_o and I_1 are the intensities at the focus and 1 cm from the center of the focal zone,one finds V_{eff} = 0.010 cm^3 and $[DCO]_0 = [D]_0$ = 5 x 10^{14} radicals/cm^3. Both estimates are in accord with the radical concentration obtained from Figure III-17 and the observed yield behavior.

If radical recombination is small, (17) and (18) determine the fate of D atoms. This competition is independent of initial radical concentration and is shown in Figure III-18. Reaction (18) dominates at high NO pressures with less than 20% contribution from (17) at 2 Torr NO. When D atoms form DNO via (18), radical decompositions produce no D_2 and only one CO,as the initially formed DCO is consumed by (16). In (17), one D_2 molecule is produced along with an additional formyl radical yielding two CO molecules per radical decomposition. In either case, each radical decomposition produces one more CO than D_2. Since molecular dissociation generates equal quantities of CO and D_2, $\phi^R = \phi_{CO} - \phi_{D_2}$.

In order to calculate the radical/molecule branching ratio, the radical yield must be normalized to the total number of dissociation events, $\phi^T = \phi^M + \phi^R$. At NO pressures greater than 2 Torr, (16) and (18)

Figure III-18. Fraction of D atom consumed by reaction (18), D + NO + M → DNO + M vs reaction (17), D + D_2CO → D_2 + DCO, for 8 Torr D_2CO as a function of NO pressure. Competition is independent of initial radical concentration. Rates used are the deuterated rates in Table III-3.

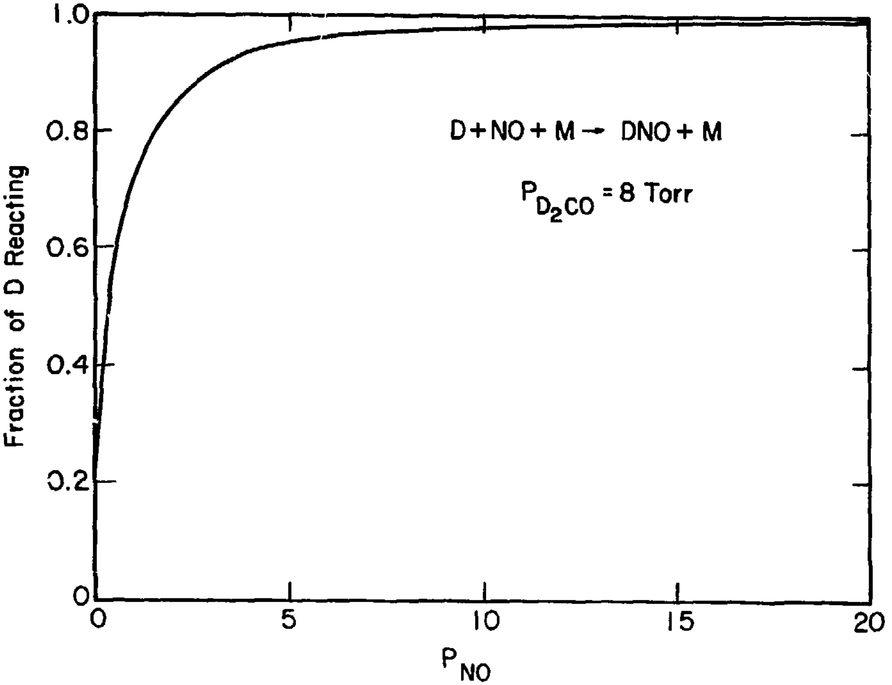
1.0
0.8
0.6
0.4
0.2
0
Fraction of D Reacting
0
5
10
15
20
P_{NO}
$D + NO + M \rightarrow DNO + M$
$P_{D_2CO} = 8$ Torr

XBL 811-7573

dominate the kinetics and $\phi^T = \phi_{CO}$. Between NO pressures of 0.2 to 2.0 Torr, (17) and (18) compete almost equally. The CO yield is larger than ϕ^T since (15) leads to the production of two CO's per radical dissociation. The D_2 yield is less than ϕ^T by the yield of (16) which produces no D_2 In this range,

$$\phi^T = \frac{\phi_{CO} + \phi_{D_2}}{2} \quad \text{within} \pm 15\%.$$

4. Results

The percentage of radical dissociation in MPD of D_2CO as a function of NO pressure is shown in Figure III-19. The line through the data with a slope of 0.013 Torr^{-1} and an intercept of 0.10 is a least squares fit to the data obtained at NO pressures greater than 3 Torr. The fall off at low NO pressures is due to incomplete radical scavenging by NO as previously described. The intercept gives the radical-molecule branching ratio in pure D_2CO, $\frac{\phi^R}{\phi^T} = 0.10 \pm 0.02$ for the fluence and focal geometry employed. The major source of error is the absolute measurement of the D_2 and CO yields. Neglect of radical recombination makes the stated branching ratio a lower limit,but its effect on the intercept should be less than 10%.

The apparent percentage of radical dissociation is seen to increase with increasing NO pressure. This necessitates the extrapolation to zero NO pressure to obtain the branching ratio in pure D_2CO. While added NO increases the apparent radical yield,it does not affect the total dissociation yield (Table III-5). The observed effect of NO on the branching ratio is probably due to the abstraction of D atoms from highly vibrationally excited D_2CO, molecules which would dissociate in the absence of NO. This reaction produces one DNO and one DCO radical ultimately

Figure III-19. Fraction of total dissociation going through the radical channel in MPD of 8 Torr of D_2CO at a laser fluence of 125 J/cm^2 vs added NO pressure. Least squares fit to data for NO pressures greater than 3 Torr gives an intercept = 0.10 and a slope of 0.013 $Torr^{-1}$. See Text for choice of ϕ^T. The photolysis wavelength was 946.0 cm^{-1}.

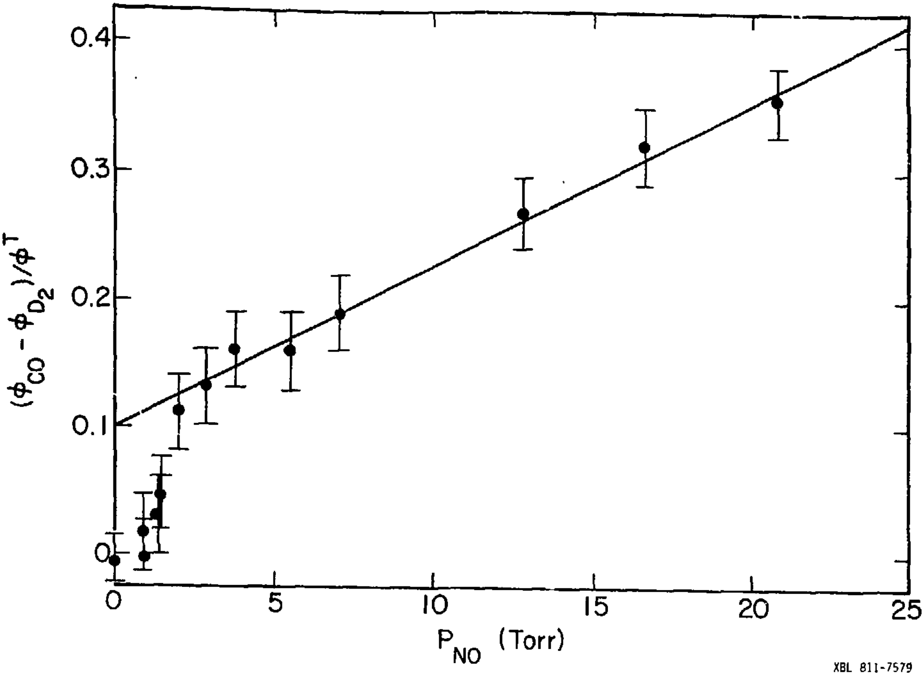

XBL 811-7579

Table III-5. Dissociation yield and branching ratio in MPD of D_2CO

P_{NO} (Torr)	Y_{D_2} (μmoles)	Y_{CO} (μmoles)	$\bar{Y}_{CO}$ (molecules/pulse)	ϕ_R
0	0.476	0.473	7.91×10^{13}	-0.006
0.90	.486	.494	8.26	.017
1.04	.483	.481	8.04	- .004
1.36	.296	.314	5.25	.057
1.44	.272	.293	4.90	.072
1.92	.747	.835	13.97	.111
2.82	.413	.475	7.94	.131
3.77	.497	.592	9.90	.160
5.50	.410	.487	8.14	.158
7.02	.330	.407	6.81	.189
12.80	.385	.525	8.78	.267
16.62	.180	.265	4.43	.321
20.75	.282	.438	7.32	.356
12.6[a]	.405	.485	2.48×10^{14}	.165
30.0[b]	.182	.227	1.55×10^{14}	.198
30.0[c]	-	.106	9.04×10^{12}	-

Photolysis conditions: 8 Torr D_2CO, 25 cm focal length Ge lens, 946.0 cm^{-1}, 1.25 J/pulse, 3600 shots except

a - 1.9 J/pulse, 900 shots,
b - 1.9 J/pulse, 1200 shots,
c - 0.8 J/pulse, 7200 shots.

yielding just one product molecule, CO, mimicking a radical dissociation.

A similar effect is seen in the UV photolysis of formaldehyde-NO mixtures[6] when the excitation frequency is above the threshold for radical chemistry. The NO effect increases at shorter excitation wavelengths. UV excitation of D_2CO just below the radical threshold, however, shows no evidence of radical dissociation even in the presence of 25 Torr of NO while molecular dissociation proceeds with a quantum yield of 0.9. Plots of the radical quantum yield vs NO pressure for UV excitation of D_2CO have slopes of 0.011, 0.016 and 0.018 $Torr^{-1}$ for sets of experiments at 304.0, 298.3, and 2940 nm, respectively. These experiments were performed by Clark et al.[6] at NO pressures of 3 and 25 Torr. The similarity with the 0.013 $Torr^{-1}$ slope seen here for IR excitation indicates that the dissociation rates in the two experiments are comparable and compete with a dissociation or reaction channel that is dependent on NO pressure. This is consistent with UV dissociation taking place through high vibrational levels of S_0. The slope for the NO effect in UV dissociation of H_2CO, again taken from the data of Clark et al., is only 0.005 $Torr^{-1}$ at 299.1 nm. This smaller effect may be due to the larger unimolecular dissociation rates for H_2CO than for D_2CO. These larger rates facilitate unimolecular dissociation before abstraction by NO can compete.

The effect of buffer gas on the percentage radical yield was studied and the results shown in Figure III-20. Photolyses of 8 Torr D_2CO, 5 Torr NO and various pressures of Kr were performed under different focal conditions than those without buffer gas so direct comparison is inappropriate. The radical yield decreases slowly with added Kr pressure. This decreasing radical yield can be attributed to two effects. First, the added buffer gas could cause a reduction of the NO effect by deactivation

Figure III-20. Fraction of total dissociation going through the radical channel in MPD of 7.9 Torr D_2CO + 5.3 Torr NO at a laser fluence of 200 J/cm^2 vs added Kr pressure. Note that a different fluence is used than in Figure III-19. The photolysis wavelength was 946.0 cm^{-1}.

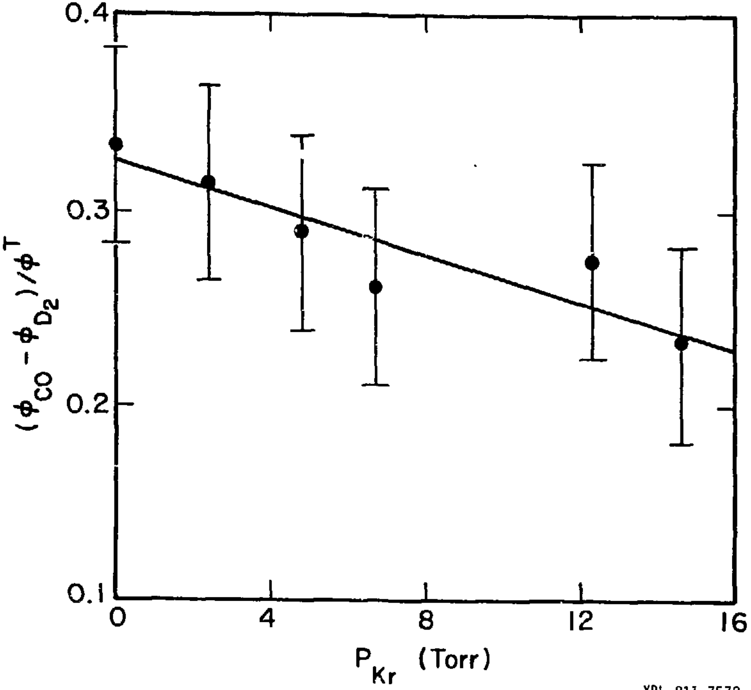

XBL 811-7578

of excited D_2CO or by collisionally aided dissociation before abstraction of a D atom from excited D_2CO by NO occurs. The total dissociation yield was not noticeably decreased by the added buffer gas (Table III-6) even up to ~34 Torr Ar. Increased rotational relaxation due to the buffer gas would, however, increase dissociation. A second possibility is that collisions with Kr remove some of the energy available for dissociation from the excited D_2CO molecules. Dissociation with a lower total energy content favors molecular dissociation. Collisions, however, increase the non-dissociative decay rates limiting dissociation to the most intense part of the pulse favoring the radical channel.

In order to confirm that radical dissociation takes place in the absence of NO, a mixture of 4 Torr each of H_2CO and D_2CO was photolyzed and the products analyzed mass spectrometrically. The results shown in Table III-7 show a significant increase in the m/e = 3 signal relative to pure D_2CO photolyses. Dissociation of the natural abundance of HDCO in the H_2CO cannot account for this large m/e = 3 signal. Radical dissociations can produce HD via $D + H_2CO \rightarrow HD + HCO$ while purely molecular decomposition cannot account for the HD production. The small yield at m/e = 2 indicates that little H_2 is formed. This indicates that significant amounts of dissociation do not occur due to thermal heating or vibrational energy transfer from D_2CO to H_2CO.

The increase in m/e = 3 signal is necessarily small since the radical channel accounts for only 10% of the total dissociation. In pure D_2CO, the D atom produced abstracts another D atom from a D_2CO molecule producing D_2 + DCO. Two DCO radicals recombine to give D_2CO + CO. With equimolar H_2CO and D_2CO present, over half of the radicals will lead to HD since isotope effects favor reaction of D atoms with H_2CO over D_2CO.

Table III-6. Buffer gas dependence of dissociaton yield and branching ratio in MPD of D_2CO

P_{Kr} (Torr)	Y_D (μmoles)	Y_{CO} (μmoles)	$\bar{Y}_{CO}$ (molecules/pulse)	ϕ_R
0	0.209	0.314	7.00×10^{13}	0.335
2.4	.287[a]	.419	8.41	.314
4.8	.353[a]	.496	9.94	.288
6.7	.299[b]	.403	8.79	.261
12.3	.274[a]	.378	7.58	.274
14.6	.311	.404	9.01	.231
34.3[c]	.374	-	8.34[d]	-

Photolysis conditions: 7.9 Torr D_2CO, 5.3 Torr NO,15 cm focal length lens, 1.25 J/pulse, 2700 shots except

a - 3000 shots,
b - 2760 shots,
c - Ar used as buffer gas,
d - D_2 yield per pulse.

Table III-7. Mass spectral analysis of hydrogen product from formaldehyde MPD

Electron Voltage	m/e	Signal; Pure D_2CO, 8 Torr	Signal; $H_2CO:D_2CO$, 4 Torr:4 Torr
70	4	100.0[a]	100.0
	3	8.3	15.6
	2	6.6	12.0
50	4	100.0	100.0
	3	8.2	15.2
	2	2.9	2.2
40	4	100.0	100.0
	3	5.3	9.8
	2	< 1	< 1

[a] Signals are relative to m/e = 4 signal.

Prompt recombination of D + DCO will lower the HD yield. If exchange with formaldehyde is fast relative to recombination of D + DCO, the HD signal will be somewhat less than 10% of the D_2 signal. This is the order of magnitude increase in m/e = 3 seen. The larger m/e = 2 and 3 signals seen with increasing electron voltage indicate the fragmentation and ion-molecule reactions are contributing to the background. Lower voltages could not be used due to loss of sensitivity.

REFERENCES

1. W. Fuss and T. P. Cotter, Appl. Phys. 12, 265 (1977).
2. D. Proch and H. Schröder, Chem. Phys. Lett. 61, 426 (1979).
3. D. K. Evans, R. D. McAlpine and F. K. McClusky, Chem. Phys. Lett. 65, 226 (1979).
4. R. L. Jaffe and K. Morokuma, J. Chem. Phys. 64, 4881 (1976).
5. P. L. Houston and C. B. Moore, J. Chem. Phys. 65, 757 (1976).
6. J. H. Clark, C. B. Moore, and N. S. Nogar, J. Chem. Phys. 68, 1264 (1978).
7. J. D. Goddard and H. F. Schaefer, J. Chem. Phys. 70, 5117 (1979).
8. W. H. Miller, J. Am. Chem. Soc. 101, 6810 (1979).
9. J. H. Clark, Ph.D. Dissertation, University of California, Berkeley, 1977.
10. E. F. Hughes, J. Chem. Phys. 35, 1531 (1961).
11. T. Nakagawa and Y. Morino, J. Mol. Spectrosc. 38, 84 (1971); T. Nakagawa, Y. Takahashi and K. Kuchitsu, Symposium on Molecular Structure and Spectroscopy, Columbus, OH, Paper TM12 (1976).
12. D. Coffey, Jr., C. Yamada, and E. Hirota, J. Mol. Spectrosc. 64, 98 (1977).
13. T. Nakagawa, (unpublished).
14. R. V. Ambartzumian, Yu. Gorokhov, V. S. Letokhov, G. N. Makarov, A. A. Puretskii, JETP Lett. 23, 22 (1976); Sov. Phys. JETP, 44, 231 (1976).
15. V. N. Bagratashvili, I. N. Knyazev, V. S. Letokhov and V. V. Lobko, Opt. Commun. 18, 525 (1976).
16. T. F. Deutsh, Opt. Lett. 1, 25 (1977).
17. D. O. Ham and M. Rothschild, Opt. Lett. 1, 28 (1977).
18. I. C. Hisatune and D. F. Eggers, Jr., J. Chem. Phys. 23, 487 (1955).
19. J. C. D. Brand, J. Chem. Soc. 1956, 858.
20. G. Koren, M. Okon and U. P. Oppenheim, Opt. Commun. 22, 351 (1977).
21. M. R. Berman and D. J. Douglas (unpublished).

22. R. B. Nerf, Jr., J. Mol. Spectrosc. 58, 451 (1975).

23. C. J. M. Fletcher, Proc. Roy. Soc. (London), A146, 357 (1934).

24. R. Klien, M. D. Scheer, and L. J. Schoen, J. Am. Chem. Soc. 78, 50 (1956).

25. I. D. Gay, C. P. Glass, G. B. Kistiakowsky and H. Niki, J. Chem. Phys. 43, 4017 (1965).

26. H. G. Schecker and W. Jost, Ber. Bunsenges Physik. Chem. 73, 521 (1969).

27. A. M. Dean, B. L. Craig, R. L. Johnson, M. C. Schultz, and E. E. Wang, Seventeenth Symposium (International) on Combustion, (Combustion Institute, 1978), p. 577.

28. A. Horowitz and J. G. Calvert, Int. J. Chem. Kinet. 10, 713 (1978); Ibid. 10, 805 (1978).

29. R. S. Lewis and E. K. C. Lee, J. Phys. Chem. 82, 249 (1978).

30. J. C. Weisshaar and C. B. Moore, J. Chem. Phys. 70, 5135 (1979); Ibid. 72, 2875 (1980).

31. J. C. Weisshaar, Ph. D. Dissertation, University of California, Berkeley, 1979.

32. R. N. Pease, Chem. Rev. 21, 279 (1937).

33. J. Peeters and G. Mahnen, Fourteenth Symposium (International) on Combustion (Combustion Institute, 1975), p. 133; C. T. Bowman, Fifteenth Symposium (International) on Combustion (Combustion Institute), p. 869.

34. J. Heicklen, Atmospheric Chemistry (Academic, New York, 1976).

35. G. Koren, U. P. Oppenheim, D. Tal, M. Okon, and R. Weil, Appl. Phys. Lett. 29, 40 (1976).

36. O. P. Strausz and H. E. Gunning, Trans. Faraday Soc. 60, 347 (1964); M. A. A. Clyne, Tenth Symposium (International) on Combustion (Combustion Institute, 1964), p. 311.

37. Y. Haas and C. B. Moore (unpublished).

38. J. P. Reilly, J. H. Clark, C. B. Moore, and G. C. Pimentel, J. Chem. Phys. 69, 4381 (1978).

39. B. A. Ridley, J. A. Davenport, J. L. Steif, and K. H. Welge, J. Chem. Phys. 57, 520 (1972).

40. A. A. Westenberg and N. de Haas, J. Phys. Chem. 76, 2213 (1972).

41. W. R. Brennen, I. D. Gay, G. P. Glass, and H. Niki, J. Chem. Phys. 43, 2569 (1965).

42. J. J. Ahumada, J. V. Michael and D. T. Osborne, J. Chem. Phys. 57, 3736 (1972).

43. W. Wong and D. Davis, Int. J. Chem. Kinet. 6, 401 (1974).

44. J. R. McNesby, M. D. Scheer. and R. Klein, J. Chem. Phys. 32, 1814 (1960).

45. J. Bigeleisen, J. Chem. Phys. 17, 675 (1949); J. Bigeleisen and M. G. Mayer, J. Chem. Phys. 15, 261 (1947); J. Bigeleisen and M. Wolfsberg, Adv. Chem. Phys. 1, 15 (1958). See also W. A. Van Hook in *Isotope Effects in Chemical Reactions*, ACS Monograph 167, ed. C. J. Collins and N. S. Bowman (Van Nostrand Reinhold, New York, 1970), p. 1.

46. J. W. C. Johns, S. H. Priddle, and D. A. Ramsay, Discuss. Faraday Soc. 35, 90 (1963); D. E. Milligan and M. E. Jacox, J. Chem. Phys. 41, 3032 (1964).

47. M. E. Jacox and D. E. Milligan, J. Mol. Spectrosc. 48, 536 (1973).

48. D. C. Moule and A. D. Walsh, Chem. Rev. 75, 67 (1975).

49. R. Klein, J. R. McNesby, M. D. Scheer, and L. J. Schoen, J. Chem. Phys. 30, 58 (1959).

50. A. A. Westenberg and N. de Haas, J. Chem. Phys. 47, 1393 (1967).

51. H. S. Johnston, *Gas Phase Reaction Rate Theory* (Ronald, New York, 1966), p. 81.

CHAPTER IV

BARRIER HEIGHT TO MOLECULAR DISSOCIATION OF FORMALDEHYDE

A. Introduction

The successful use of a rate equation model to treat MPD in SF_6 and other large molecules has been demonstrated by several authors.[1-5] In this chapter the model is applied to MPD in D_2CO in order to obtain the barrier height to molecular dissociation from the experimentally observed radical/molecule branching ratio. The branching ratio calculated from the rate equation model depends on the dissociation rates used for each reaction channel hence on the barrier height to molecular dissociation. Shifting the barrier height affects the rates for molecular dissociation. Thus by varying the dissociation rates in the calculation, the branching ratio was evaluated as a function of barrier height. Matching the calculated value with the experimentally observed branching ratio provides a measure of the barrier height.

The applicability of the rate equation model to MPD in D_2CO is not unquestioned. This process differs on several counts from the collisionless dissociation observed in SF_6. It can be argued on the basis of the observations in Chapter III and discussions in this chapter that most differences arise basically from the difficulty of excitation through the discrete state region in D_2CO. Once in the QC, the molecules behave similarly: excitation is incoherent and a rate equation model is valid. Additional terms are required in the master equation, however, to deal with collisional processes occurring during excitation in the QC. The presence of collisions strengthens the assumption of statistical energy distribution which permits the use of RRKM theory to describe the unimolecular reaction rates.

Since D_2CO is a small polyatomic molecule, a QC may not exist until very high levels of excitation in the molecule are reached. Parameters in the calculation model how and when molecules enter the QC. These parameters have little effect on the calculated barrier height, however, as their effects are "washed out" as molecules climb the ladder of vibrational excitation. The absorption of about 30 photons is necessary to excite D_2CO to its dissociative levels so effects at the lower levels are unimportant. The branching ratio is instead determined in the region where the dissociation rates of the levels, k_m, are comparable to the excitation rate, k_{exc}. The position of the onset of the QC is of little importance so long as a QC exists in this region where $k_m \sim k_{exc}$. The relative valves of the radical and molecular dissociation rate constants in this region, along with the excitation and deactivation rates, define the branching ratio. Assuming that RRKM theory is applicable to each dissociation channel, the ratio of the rates for dissociation through the radical channel to dissociation via the molecular channel depends on the threshold for radical decomposition and the height of the barrier to molecular dissociation. The product distribution depends most sensitively on the position of these levels relative to one another. The rate equation calculations are used to determine that energy difference between the radical threshold and the barrier height, $E_{rad.\,thr.} - E_{bar.\,ht.} = \Delta BT$. The location of the top of the barrier relative to the ground state level of D_2CO then depends on the exact position of the radical threshold.

The rate equation calculations performed here are less than rigorous: Approximations are invoked to simplify the treatment of collisions and QC absorption cross sections; the calculations rely on theoretical calculations[4] of RRKM tunneling rates to molecular products; limiting values, estimated from the literature must be used for other parameters in the calculations. The range of acceptable values for these parameters defines limiting values for the barrier height. These semi-quantitative calculations nonetheless provide a valuable experimental probe of the barrier height to compare with recent *ab initio* calculations.[5,6] These results are also useful in resolving some questions regarding the thermal chemistry and the UV photochemistry of formaldehyde.

B. Rate Equation Model

1. Justification

There are several prerequisites for the use of the rate equation model to describe MPD in D_2CO. It must first be determined if, for the most part, excitation and dissociation are due to optical pumping. Then, the applicability of the rate equation model to MPD in small molecules must be determined.

Let us begin by considering possible dissociation mechanisms other than pure multiphoton absorption. Excitation and dissociation could result from thermal heating (V-T,R transfer) or intermolecular vibration-to-vibration (V-V) energy transfer. The former can be treated by examining the IR fluorescence from the C-D stretches in multiphoton excited D_2CO (see Fig. III-15). The initial peak occurring about 1 μs after the start of the laser pulse is due to purely vibrational excitation. All of the absorbed energy still resides in the vibrational degrees of freedom. The long fluorescence tail, however, arises from the degradation of the absorbed energy to thermal excitation. The amplitude of this thermal component of the fluorescence extrapolated back to the time of the maximum fluorescence is 1/6 that of the peak vibrational fluorescence. By comparing these fluorescence amplitudes the peak thermal temperature reached and the amount of thermal decomposition can be estimated.

The amplitude of the IR fluorescence from a given vibrational mode can act as a thermometer for its vibrational temperature since the fluorescence is proportional to the total population in that mode. Each mode can achieve a distinct vibrational temperature when V-T,R transfer is considerably slower than V-V equilibration as a metastable vibrational distribution is established.[7] Temperatures for the bending and stretching modes in D_2CO were calculated as a function of energy absorbed in the bending mode using a quasithermodynamic approach developed by Shamah and Flynn.[8] In this model, the stoichiometry of the V-V transfer process and the energy gap between initial and final states determine the resulting vibrational temperature for each mode.

Due to their overlap and Coriolis coupling,[9] the two C-D stretches were considered to be degenerate with an average frequency of 2108 cm^{-1} while the bends were also taken to be doubly degenerate[10,11] however, the pumping frequency 946 cm^{-1} was used. The amount of energy funneled into the C-D stretches from the pumped bending modes depends on the V-V transfer mechanism that is operational. The stretching modes are most probably collisionally populated by a near-resonant transfer of two bending quanta, be it through the collision of two molecules each having a bending quantum or of a vibrationally cold molecule with a bending overtone. Neglecting anharmonicity,

$$D_2CO\ (\nu_b) + D_2CO\ (\nu_b) \rightarrow D_2CO\ (\nu_s) + D_2CO - 108\ cm^{-1} \qquad (1)$$

$$D_2CO\ (2\nu_b) + D_2CO \rightarrow D_2CO\ (\nu_s) + D_2CO - 108\ cm^{-1} \qquad (2)$$

The other vibrational modes were not included in the calculation since they were further off resonance and only had an effect on the total energy content. The actual absorbed total energy is therefore significantly greater than the calculated values due to energy in the other modes.

According to Shamah and Flynn,[8] the temperatures of the absorbing mode i and the collisionally coupled mode j are related by

$$T_i = [\varepsilon_i T_j/(f_{ji}\varepsilon_j T' + (\varepsilon_i - f_{ji}\varepsilon_j)T_j)]\ T' \tag{3}$$

where $\varepsilon_i = h\nu_i$, $f_{ji} = v_j/v_i$, the v's being the quantum numbers for the states between which intermode energy transfer occurs, and T' is the steady-state translation-rotation temperature taking into account the endo or exothermicity of the V-V energy transfer process. The ambient temperature T is related to T' by the thermodynamic expression

$$3Nk\ (T'-T) = N \sum_j \left(f_{ij} \frac{\varepsilon_i}{\varepsilon_j} - 1\right)\ \Delta\bar{E}_j^{vib} \tag{4}$$

where $\Delta\bar{E}_j^{vib} = \bar{E}_j\ (T_j) - \bar{E}_j^{\circ}\ (T)$ is the mean vibrational excitation per molecule in mode ν_j. The average energy of a vibrationally excited molecule in mode j is

$$\bar{E}_j\ (T_j) = g_j\varepsilon_j/[\exp(\varepsilon_j/kT_j)-1]. \tag{5}$$

Equations (3) and (4) were solved iteratively (see Table IV-1) for T' and the temperature of the stretching mode, T_s, for a given bending mode temperature, T_b and the energy transfer scheme proposed in (1) and (2). The calculated vibrational temperatures are shown in Fig. IV-1. The temperature of the bending mode continuously increases while the stretching mode saturates fairly early. The limiting temperature of the

Table IV-1. Parameters and results used in calculation of vibrational temperatures[a]

T_b (K)	$\bar{E}_b$ (cm^{-1})	T_s (K)	E_s (cm^{-1})	T' (K)	E_{abs} (cm^{-1})	ϕ[b]
750	552	649	39.7	298	561	0.59
1000	978	803	88.4	295	1036	1.09
1250	1439	935	170	292	1578	1.67
1500	1919	1048	246	288	2134	2.26
1750	2411	1144	320	284	2700	2.85
2000	2909	1229	350	281	3228	3.41
2250	3413	1300	452	277	3834	4.05
2500	3920	1363	510	274	4399	4.65
5000	9068	1720	870	255	9906	10.47
7000	13122	1845	1009	248	14195	15.00

---

[a] Calculations use ε_b = 946 cm^{-1}, ε_s = 2108 cm^{-1}, $g_b = g_s = 2$, $f_{bs} = 2$.

[b] ϕ = number of photons absorbed per molecule.

Figure IV-1. Temperatures for the bending modes (ν_b = 946 cm^{-1}, g_b = 2), T_b, and the stretching modes (ν_s = 2108 cm^{-1}, g_s = 2), T_s, and the steady-state translation-rotation temperature, T', achieved by vibrational equilibration of the bending and stretching modes in D_2CO as a function of the number of photons ($h\nu$ = 946 cm^{-1}) absorbed. V-T,R processes are assumed to be much slower than V-V transfer. The calculations were performed using equations (3) and (4) assuming that energy flows only between these modes. The abscissa, therefore, does not reflect the total energy content of the molecule.

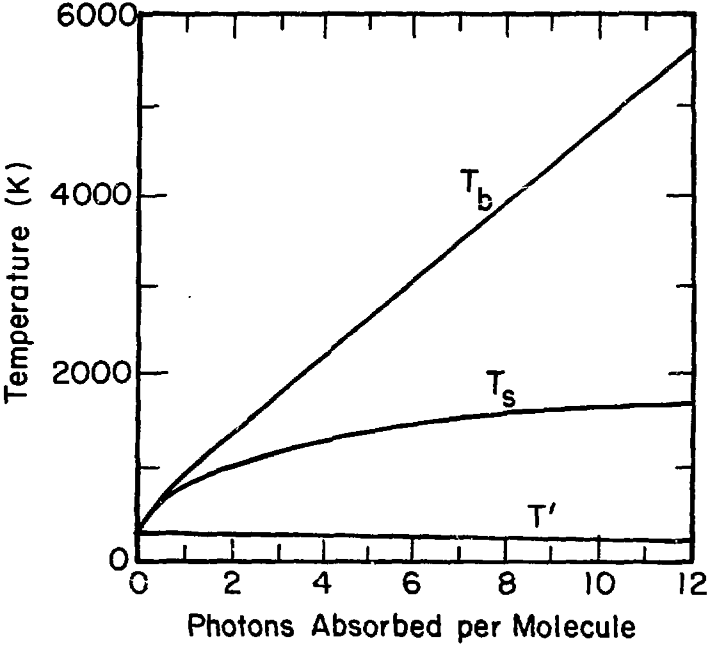
6000
4000
2000
0
Temperature (K)
T_b
T_s
T'
0
2
4
6
8
10
12
Photons Absorbed per Molecule

XBL 811-7582

stretching mode is a function of T',

$$T_s^{max} = [f_{sb}\varepsilon_s/(f_{sb}\varepsilon_s - \varepsilon_b)]\ T'. \tag{6}$$

Including only the C-D stretches and the bending modes results in an endothermic process giving thermal cooling (T' = 200 K) and a limiting value of $T_s^{max} \approx 2000$ K. If other processes maintain T' at its initial valve of ~300 K then T_s^{max} approaches 3000 K. A stretching mode temperature of 3000 K corresponds to an average population in each stretching mode of $\langle n\rangle_s^{vib} = 0.57$ where

$$\langle n\rangle_s^{vib} = \frac{\bar{E}_s^{vib}}{h\nu_s}$$

(see Fig. IV-2). Since the amplitude of the thermally excited stretches is 1/6 that of the peak vibrationally excited fluorescence from the stretches, the thermal population of the stretching mode due to laser heating is $1/6 \times \langle n\rangle_s^{vib} = 0.095$. Assuming statistical distribution of energy in all degrees of freedom (thermal equilibrium), this population corresponds to a maximum thermal temperature of ~1250 K (see Fig. IV-2) and sets an upper bound on the equilibrated temperature. The rate constant for thermal decomposition of H_2CO has been measured by Schecker and Jost[12] and Dean et al.[13] as 8.3×10^{-8} exp (-72 kcal/mole/RT) and 6.0×10^{-7} exp(-87 kcal/mole/RT) cm^3 $molecule^{-1}$ s^{-1} respectively, in the ranges 1400-2200 and 1800-2500 K. Since the maximum thermal temperature of ~1250 K is maintained for less than 10^{-3} s, thermal dissociation, according to these rates, would destroy on the order of 10^{-5}% of the molecules in the focal volume. This is negligible compared to the 2% dissociation yield seen for molecules in the focal region. The lack of H_2 production in the photolysis of an equimolar mixture of H_2CO and D_2CO

Figure IV-2. The upper curve shows the average total energy content per D_2CO molecule as a function of temperature for thermal excitation. The energy scale on the left is multiplied by 10 for this curve and the ordinate on the right is inapplicable. The lower curve shows the average vibrational energy in one C-D stretching mode of D_2CO (ν_s = 2108 cm^{-1}, g_s = 1), as a function of the vibrational temperature, T_s. The right hand ordinate gives the average population in this mode as a function of T_s.

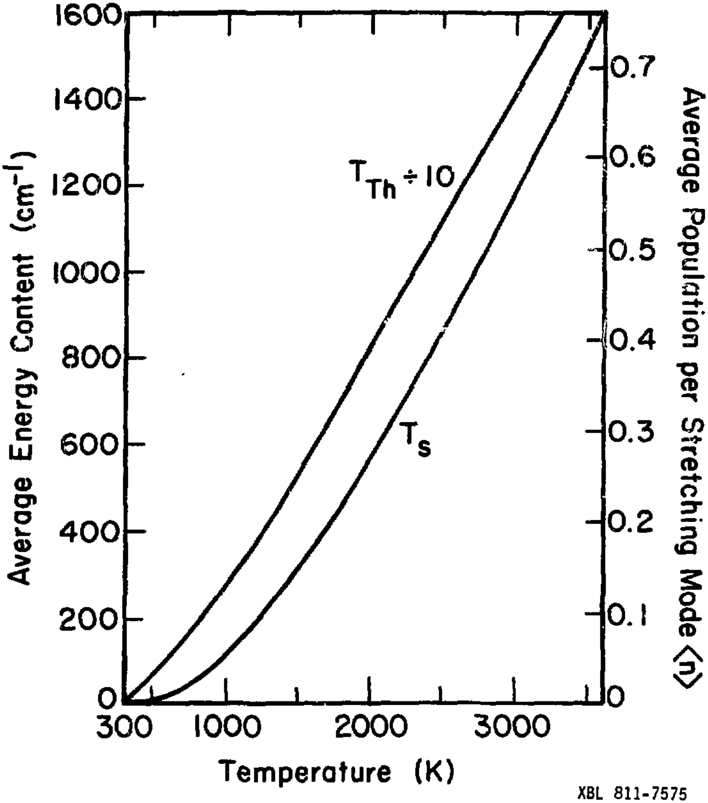
Average Energy Content (cm^{-1})
1600
1400
1200
1000
800
600
400
200
0
300
1000
2000
3000
Temperature (K)
$T_{Th} \div 10$
T_s
Average Population per Stretching Mode ⟨n⟩
0.7
0.6
0.5
0.4
0.3
0.2
0.1
0

XBL 811-7575

also argues strongly against thermal decomposition.

Several results can be used in order to gauge the role of V-V energy transfer in the excitation process. The low H_2 production in the equimolar H_2CO-D_2CO photolysis indicates that V-V transfer to H_2CO was insufficient to either quickly excite H_2CO to the QC or cause dissociation. V-V transfer from D_2CO to H_2CO would, however, likely be slower than transfer between D_2CO molecules due to resonance effects. The IR fluorescence data for multiphoton-excited mixtures of D_2CO + Ar (Sec. III-E) showed that V-V transfer between D_2CO molecules is necessary to overcome bottlenecks at the v=1 level. For molecules in the QC, however, V-V transfer is insignificant compared to optical pumping. The excitation rate for the latter is $\sim 10^9\ s^{-1}$ while collisional uppumping would proceed at a rate of $\sim 10^8\ s^{-1}$ if uppumping took place on every collision. Due to microscopic reversibility, there must be more deactivating than uppumping collisions for hot molecules. Since only about 20% of the molecules in the focal volume are excited (see Sec. IV-B.2), the probability of significant collisional uppumping relative to optical excitation is quite small. Lyman[3] has included the effects of collisions in a rate equation description for unimolecular dissociation of SF_6 and a simplified treatment is used here.

Previously, rate equation descriptions have been applied to MPD in large molecules.[1-3] The applicability of the model depends on excitation through the QC being incoherent. In small molecules which display quite different MPD characteristics,[14] the QC, if one exists, begins at very high vibrational levels due to the low density of states. Fuss,[2] however, points out that as long as an effective local continuum is established within a resolution ω_R excitation will be incoherent. This condition can be met in small molecules due to anharmonic splittings, Coriolis interactions and combination and overtone bands which cluster around multiples of the fundamental frequency. Variations of the transition dipole moment between different molecules within the laser bandwidth also inhibit coherent oscillation of the population between vibrational levels.[2] Incoherent excitation is therefore a viable approximation or description for small polyatomic molecules and the rate equation model is applicable even though a true QC may not exist.

MPD of formaldehyde displays strong power dependences,[15] D_2CO yield being proportional to $I^{3.3}$ with HDCO yield going as $\sim I^5$. Koren and Oppenheim[16] argued that laser power was more important than laser fluence in MPD of HDCO since they found that experiments using a laser pulse having a 150 ns spike and no tail gave about a ten times greater yield than a pulse of the same total energy having 1/4 of the energy in the 150 ns spike and the remainder in a 1 μs long tail. They further argued that since collisions increase MPD in HDCO one would expect greater dissociation for longer pulses if fluence were an important parameter. If, however, collisions and high power are only necessary to excite molecules through the discrete state region as argued in Chapter III of this thesis, their results are still consistent with fluence dependent incoherent excitation in the QC. The higher yield at higher power occurs since more molecules can reach the QC. Once in the QC, collisions act to deactivate excited molecules thus reducing dissociation yields.

2. Calculation Details

Using a modified version of the rate equation model developed by Schulz and co-workers[1] the normalized population of the m^{th} excited level at energy $mh\nu$ is governed by

$$\frac{dN_m}{dt} = \frac{I(t)}{h\nu}\left[\sigma_{m-1}N_{m-1} + \frac{g_m}{g_{m+1}}\sigma_m N_{m+1} - \left(\frac{g_{m-1}}{g_m}\sigma_{m-1} + \sigma_m\right)N_m\right] + k_{col}\,(N_{m+n} - N_m) - k_m N_m \tag{7}$$

where I(t) is the laser intensity, hν is the photon energy, σ_m is the absorption cross section from level m to level m+1, and g_m is the degeneracy factor for level m, just the density of states in this case. The total rate of unimolecular dissociation from level m is given by k_m, the sum of the rates for molecular and radical decomposition. The collisional deactivation rate is k_{col}. Deactivation is taken to occur in energy steps of nhν, integral multiples of the photon energy.

The laser pulse profile used in the calculations is taken from the output of the photon drag detector and is shown in Fig. II-1a. The pulse was divided into 10 ns sections and the intensity taken as the integral of each section normalized to the fluence of 125 J/cm^2. Integration of Equation (7) over time yields level populations in the QC that depend on fluence, not on intensity. In each calculation the integration of the set of rate equations to determine the level populations was performed at intervals of 10 ps. All calculations were performed on the LBL CDC 7600/6600 computer system.

Since this model treats only molecules in the QC, it is significant at what level the QC begins, how quickly molecules reach that level and what fraction of the irradiated molecules enter the QC. These factors affect the degree of uppumping and the resulting branching ratio between radical and molecular products. Most of these effects, however, are quite small due to the large number of steps up the ladder to dissociation.

A QC as defined by the condition that the inverse of the laser linewidth, 10/cm^{-1}, is greater than the density of states is not reached in D_2CO until 20,000 cm^{-1} considering harmonic vibrational states (see Fig. IV-3). Since D_2CO is an asymmetric rotor, the density of states available for allowed radiative transitions is increased by a factor of from 3 to 6 due to rotational states. This lowers the QC onset to 13,000 - 16,000 cm^{-1}. Power broadening, on the order of 1 cm^{-1}, and strong vibration-rotation coupling in D_2CO can significantly lower this level. Calculations of branching ratios were found to be very insensitive to the level of the QC onset between $v = 5$ to 15 and were generally performed with the onset at $v = 10$ (Table IV-2).

MPD in D_2CO differs from MPD in SF_6 in that collisions as well as laser intensity determine the coupling of molecules into the QC. In the calculations, molecules enter the QC through an additional source term for the level at the QC origin. The functional form of how molecules were coupled to the QC as a function of time was determined from the observed pressure and power dependences of the dissociation yield. A cubic pressure dependence is seen for D_2CO dissociation. One factor of pressure arises from the increased number density. The probability of dissociation, which is equated here with entering the QC, therefore depends on the square of the pressure or the square of the number of collision undergone. As the yield is also proportional to approximately the cube of the laser power, the fraction of the total number of molecules that eventually enter the QC that enter in a given time was taken to be

$$c(t) / \sum_{t=0}^{t_{max}} c(t)$$

Figure IV-3. The density of vibrational states (right hand ordinate) in SF_6 and D_2CO as a function of energy in the molecule. The former was calculated by the Whitten-Rabinovitch approximation and the latter by direct count. The left hand ordinate gives the density of vibration-rotation states in D_2CO (v, J) as a function of energy.

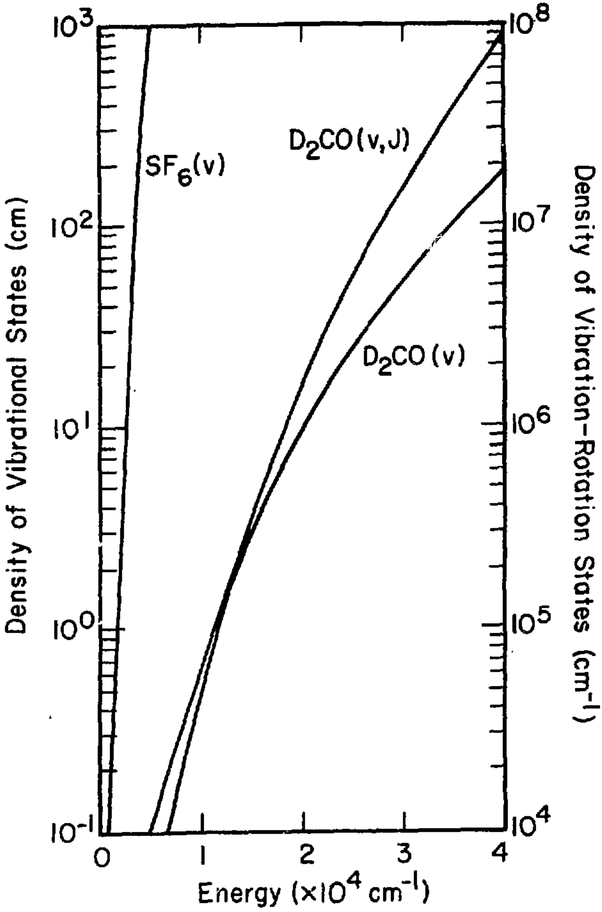
10³
10²
10¹
10⁰
10⁻¹
Density of Vibrational States (cm)
10⁸
10⁷
10⁶
10⁵
10⁴
Density of Vibration-Rotation States (cm⁻¹)
0
1
2
3
4
Energy (×10⁴ cm⁻¹)
SF6(v)
D2CO(v,J)
D2CO(v)

XBL 811-7572

Table IV-2. Effects of Parameters on Calculated Barrier Heights[a]

QC onset (v)	QC Coupling[b]	E (J/cm^2)	Dissociation Yield (% in QC)	Barrier Height[c] (kcal/mole)	ΔBT (kcal/mole)
5	I	125	1.1	87.3	2.3
10	I	125	3.0	87.1	2.5
15	I	125	8.6	86.8	2.8
10	II	125	2.0	87.3	2.3
10	II	75	0.06	88.0	1.6

---

[a] Calculations use $\sigma = 2.0 \times 10^{-20}$ cm^2, $\varepsilon_D = 1000$ cm^{-1}, $J = 10$, $k_{rad} = \frac{2}{3} k_{mol}$, and the radical threshold = 89.6 kcal/mole.

[b] See text.

[c] Barrier height which gives a 10% radical yield.

[d] ΔBT = Radical threshold - Barrier height.

where $c(t) = n_c^2(t) \times I^3(t)$, $n_c(t)$ is the number of collisions per molecule undergone during a time t after the start of the laser pulse, I is the laser intensity and t_{max} is the time at the peak of the laser pulse. This model, denoted as type I coupling, discriminates against molecules that couple to the QC after the peak of the pulse and are thus exposed to smaller uppumping rates. The extent of this effect can be seen from calculations performed with the coupling to the QC considered to be a step function with unity coupling at time t_{max}. This is denoted as type II coupling. The branching ratio in these calculations is slightly lower than for type I coupling since in the former some molecules are exposed to uppumping for a shorter period of time. This results in a calculated barrier height for type II coupling that is 0.2 kcal/mole higher than when type I coupling is used.

Since the rate equation calculation deals only with molecules that have reached the QC, in order to compare the calculated yields with experimentally observed dissociation yields, one must know the fraction of irradiated molecules that couple to the QC. In Section IV-B.1 it was shown that a maximum thermal temperature of ~1250 K was achieved in the focal region. This corresponds to an average energy content of ~4000 cm^{-1}/molecule. The rate equation calculations indicate that at peak vibrational excitation, the average excitation level of absorbing molecules is between $v = 17$ to 20. In order to deposit the observed quantity of total energy into the focal volume, the number of molecules absorbing in the QC must represent ~20% of the total number of molecules in that region. The experimentally observed dissociation yield is typically 0.4% of the molecules in the geometrically calculated focal volume or 2% of the molecules in the effective focal volume calculated correcting for the power dependence of dissociation (see Sec. III-F.3).

The acceptable calculated yield is thus determined by the experimentally observed yield divided by the percentage of absorbing molecules. Using generous error limits, barrier heights were estimated only from calculations which predicted dissociation yields of between 2 and 25% of the molecules in the QC.

Since collisions occur throughout the excitation process, the excited distribution of molecules should exhibit a continuous spread of energies rather than discrete packets up the energy ladder as is the case in a single calculation. In one calculation, the energy levels are not closely spaced enough to determine this smooth distribution. Performing rate equation calculations at several photon energies differing by only 0.05 kcal/mole (2.65, 2.70 and 2.75 kcal/mole) provides nearly identical excitation up slightly offset energy ladders. The results define a smooth distribution of dissociation yield vs excitation energy. The fraction of dissociation in the radical channel is the ratio of the area under the curve defined by the total yield distribution times k_{rad}/k_{tot} to the area under the total yield distribution curve.

3. Excitation and Deactivation

Incoherent excitation in the QC is governed by the photon flux and the absorption cross section at each particular level. The former is experimentally determined so only the cross sections remain to be determined. Several functional forms have been proposed[1,2] for QC absorption cross sections predicting cross sections which increase, decrease, or are constant with increasing excitation. For harmonic oscillators, the absorption cross section will increase with vibrational level v. Detuning due to anharmonicity or intensity borrowing by nearby states tend to reduce the average absorption cross section at higher v. A constant cross section throughout the QC has been used successfully[3,17] in other rate equation calculations and is adopted here.

The magnitude of the QC absorption cross section can be estimated from the observed integrated intensity of the $v = 0 \rightarrow 1$ transition for the 200 cm^{-1} broad band consisting of the overlapped ν_4 and ν_6 modes in H_2CO. The integrated intensity has been measured[18] to be $A_{H_2CO} = 1.6 \times 10^{-18}$ cm/molecule. Multiplying by $(\nu_D/\nu_H)^2$ provides an approximate correction for the effect of deuteration giving $A_{D_2CO} = 1.0 \times 10^{-18}$ cm/molecule. Since the transition moment is proportional to the vibrational quantum number of the final state of the transition, the intensity must be multiplied by the average vibrational quantum number of the ν_4 and ν_6 modes in the QC. If intramolecular energy redistribution is complete throughout all vibrational modes on the time scale of the absorption, then distribution of 20,000 cm^{-1} in D_2CO results in the excitation of the pumped ν_4 and ν_6 modes each to $v=4$. If the intensity is then distributed across the entire 200 cm^{-1} wide rotational profile, the resulting average cross section is

$$1.0 \times 10^{-18} \text{ cm/molecule} \times 4 \div 200 \text{ cm}^{-1} = 2.0 \times 10^{-20} \text{ cm}^2.$$

Larger cross sections could arise due to incomplete randomization of energy among the vibrational modes resulting in a larger value of v or from incomplete energy coupling across the 200 cm^{-1} wide absorption band. Values of σ_{QC} in the range 2-8 x 10^{-20} cm^2, along with the deactivation rates used, gave calculated total dissociation yields of between 2 and 25% of the molecules excited to the QC and were used in estimating the barrier height. Using a collisional deactivation rate constant that is only 0.3 times the gas kinetic collision frequency, a QC cross section of 1 x 10^{-20} cm^2 produced a yield of less than 1% of the molecules in the QC.

Deactivation was included from two sources: stimulated emission and collisional deactivation. The former is determined by the absorption cross section and the density of states of the levels involved which was calculated using the Whitten-Rabinovitch approximation.[19] Densities of states calculated in this manner agree with a direct count of harmonic vibrational levels to better than 0.5% at energies above 10,000 cm^{-1}. Collisional processes, deactivation and uppumping, are treated as a single net deactivation term. Deactivation step sizes ranging from 100 to 5000 cm^{-1} per collision have been observed[20] in other highly vibrationally excited molecules. Since deactivation in the calculations proceeds in steps of $h\nu$, calculations were performed with a range of deactivation step sizes between 1000-5000 cm^{-1} per collision. Deactivation was presumed to take place on every gas kinetic collision, $k_{col} = 8.3 \times 10^7\ s^{-1}$. This simple model does not explicitly take into account uppumping or the dependence of the probability of energy transfer on internal energy. It was shown in Section IV-B.2, however, that only about 20% of the molecules in the focal zone are excited. Over 80% of all D_2CO-D_2CO collisions will, therefore, deactivate the excited molecules as detailed balancing also favors deactivation. Thus, collisional uppumping will be small compared to optical pumping and deactivation and can be considered as merely decreasing the average deactivation step size. Lyman[3] has included a more detailed description of vibrational energy transfer in his rate equation calculations on unimolecular decomposition of SF_6 where collisional excitation was the prime source of energization. Such a detailed treatment did not seem warranted in this case.

4. Dissociation Rates

The molecular dissociation rates used in these calculations were RRKM rates calculated by Miller[4b] for formaldehyde dissociation to molecular products including corrections for tunneling. The values of these rates relative to one another should be accurate to within 20-30%.[4b] The transition state frequencies used in the RRKM calculation were calculated by Goddard and Schaefer[5] with the stretching frequencies scaled by Miller[4,6] and are listed in Table IV-3. The dissociation rates are shown in Figure IV-4 for the barrier height calculated by Goddard and Schaefer[5] and molecules in $J=0$. Rates for D_2CO in $J=10$, the maximum of the rotational population distribution at 298 K, were obtained by dividing the $J=0$ rates by 2 as suggested by Miller.[4] The rates shown contain the factor of 2 increase required[4] due to the symmetry number of 2 in H_2CO and D_2CO resulting from the two-fold rotation axis in these molecules. Rates for H_2CO calculated[4b] using transition state frequencies calculated under the same level of approximation as the ones used here differ only slightly from newly calculated values[6] for H_2CO. Previously calculated rates[4a] were incorrect due to errors in the transition state frequencies.

The tunneling rates were calculated using an Eckart potential[21] for the barrier with the vibrational frequency along the reaction coordinate and the barrier height taken from Goddard and Schaefer.[5] This barrier height of 93.6 kcal/mole is the energy difference between the minima of the ground state formaldehyde and molecular dissociation transition state potential surfaces. In this work, the zero of energy is taken as the zero-point level of ground state D_2CO. Barrier heights include the transition state zero-point energy (ZPE) so these heights correspond to the minimum energy required to overcome the barrier (see Fig. IV-5).

Table IV-3. Transition state frequencies used in RRKM calculation of molecular dissociation rates[a]

	H_2CO	D_2CO
ν_1	2714	2115
ν_2	1811	1678
ν_3	1261	954
ν_4	1015	725
ν_5	800	543
ν_r	2320i	1530i
ZPE (cm^{-1})	3800.5	3007.5
ZPE (kcal/mole)	10.9	8.6

---

[a] Units of all frequencies are cm^{-1}.

Figure IV-4. The RRKM dissociation rates for D_2CO molecular dissociation as a function of energy are shown for a barrier height of 89.1 kcal/mole. See text for details of calculation.

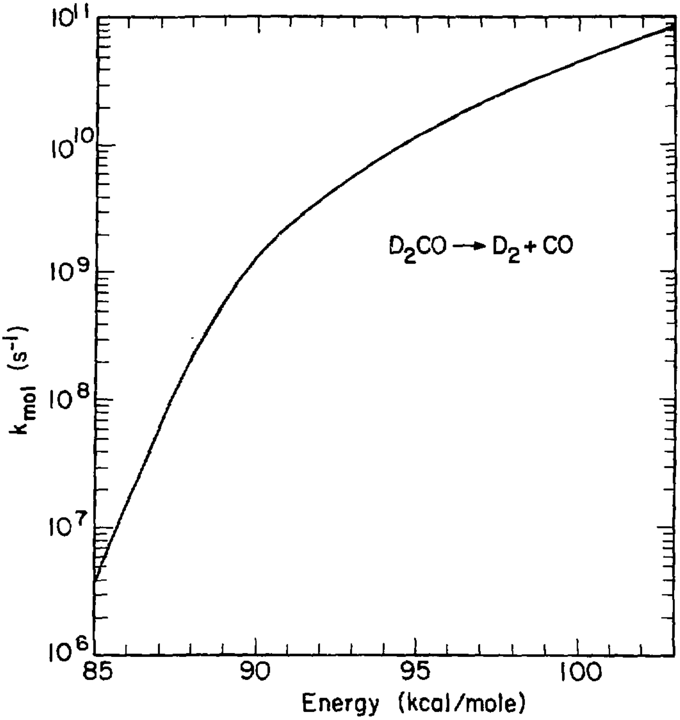

10^{11}
10^{10}
10^{9}
10^{8}
10^{7}
10^{6}
k_{mol} (s^{-1})
$D_2CO \rightarrow D_2 + CO$
85
90
95
100
Energy (kcal/mole)

XBL 811-7503

Figure IV-5. An energy level diagram for formaldehyde showing the zero-point levels of ground state molecule, the transition state to molecular products, and the formyl radical. The minima of the formyl radical and formaldehyde potential surfaces as well as the bare barrier to molecular dissociation are also shown. The difference in zero-point energies (ΔZPE) between the hydrogen and deuterium isotopes for the ground state molecule (M), the transition state (TS) and the radical (R) are indicated. The vertical arrows represent the barrier measured between zero-point levels of the formaldehyde and the transition state.

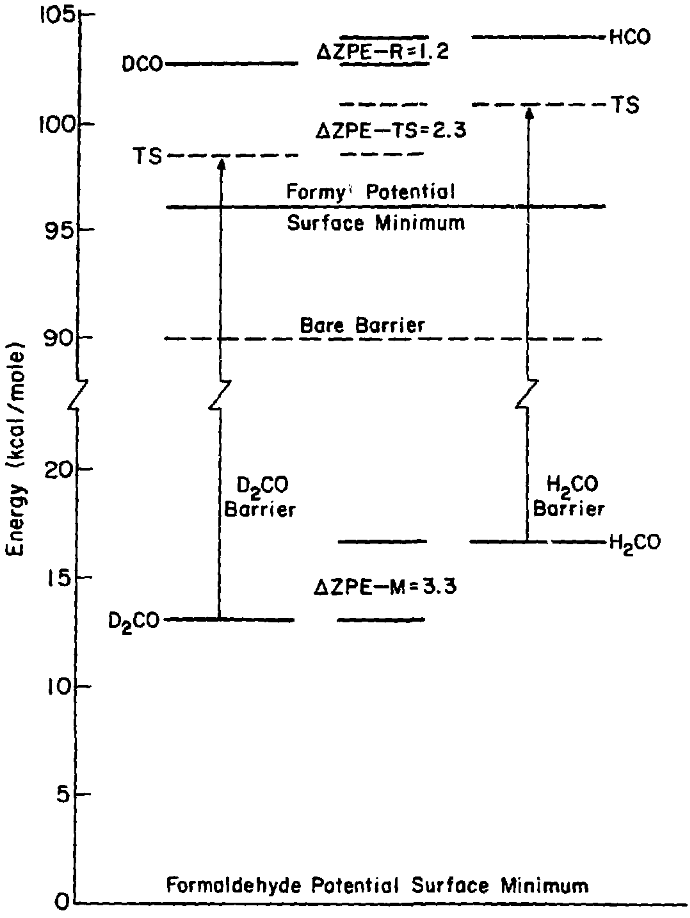
Energy (kcal/mole)
105
100
95
90
20
15
10
5
0
DCO
ΔZPE−R=1.2
HCO
TS
ΔZPE−TS=2.3
TS
Formyl Potential
Surface Minimum
Bare Barrier
D_2CO Barrier
H_2CO Barrier
H_2CO
ΔZPE−M=3.3
D_2CO
Formaldehyde Potential Surface Minimum

XBL 811-7501

The ZPE of the transition state to molecular products is taken as one half the sum of the calculated transition state frequencies listed in Table IV-3. The ZPE of ground state formaldehyde (see Table III-4) is not exactly equal to one half the sum of the observed fundamental frequencies. The ZPE defined in terms of the harmonic frequencies ω_i is[22]

$$\mathrm{ZPE} = \frac{1}{2}\sum_i \omega_i + \frac{1}{4}\sum_i x_{ii} + \frac{1}{4}\sum_i \sum_{j>i} x_{ij} \tag{8}$$

where the x_{ij} are the anharmonicities (usually negative) and higher order terms are neglected. The ZPE obtained from one half the sum of the observed fundamental frequencies can be expressed as

$$Z_\nu = \frac{1}{2}\sum_i \nu_i = \frac{1}{2}\sum_i \omega_i + \sum_i x_{ii} + \frac{1}{2}\sum_i \sum_{j>i} x_{ij}\,. \tag{9}$$

This differs from the true ZPE as

$$\mathrm{ZPE} = Z_\nu - \frac{3}{4}\sum_i x_{ii} - \frac{1}{4}\sum_i \sum_{j>i} x_{ij}\,. \tag{10}$$

Combining equations (8) and (10) and defining $Z_\omega = \frac{1}{2}\sum_i \omega_i$,

$$\mathrm{ZPE} = \frac{1}{2} Z_\nu + \frac{1}{2} Z_\omega - \frac{1}{4}\sum_i x_{ii}\,. \tag{11}$$

If we assume that all of the $x_{ij} = 0$, then this reduces to

$$\mathrm{ZPE} = \frac{1}{4} Z_\nu + \frac{3}{4} Z_\omega\,. \tag{12}$$

Using this equation and the harmonic frequencies for D_2CO from Duncan and Mallinson[23] gives $Z_\omega = 13.2$ kcal/mole, $Z_\nu = 12.8$ kcal/mole, and ZPE = 13.1 kcal/mole. The calculated barrier height[5] of Goddard and Schaefer corrected for ground state and transition state ZPE's is then 93.6-13.1 + 8.6 = 89.1 kcal/mole.

The rate constants for the radical dissociation channel were estimated in two ways. First, RRKM calculations were performed using a program written by W. L. Hase and D. Bunker, assuming a D atom breaking away from a rigid DCO fragment. RRKM calculations on bond cleavage reactions with no barrier to the back reaction are difficult to perform[24] accurately since the critical configuration is not well defined. Minimum state density calculations are often used[24,25] to determine the appropriate transition state parameters. In this case, the critical configuration was estimated from Goddard and Schaefer's calculation of radical decomposition in H_2CO (Ref. 5, Fig. 5) as having one C-D bond extended to between 2.5 to 3 times its equilibrium bond length. The vibrational frequencies used were scaled D_2CO frequencies. The vibrational frequencies, moments of inertia and bond lengths[26] used in the RRKM calculations are listed in Table IV-4. A radical threshold of 89.6 kcal/mole was used. The calculated unimolecular dissociation rate constants are shown in Figure IV-6 for different sets of transition state parameters. The extreme curves were each used in the rate equation calculations.

An alternative approach to the determination of the radical dissociation rates was to fix the ratio of the radical to molecular dissociation rates according to the observed branching ratio in UV photolyses.[27] Above the radical threshold, a constant 3:2 ratio of molecular to radical quantum yield was observed. Thus, radical rates were set to be $\frac{2}{3}k_{mol}$. This description is consistent with the independent RRKM calculations for each channel as the calculated radical and molecular rate constants in Figure IV-6 approximately display this behavior. The problem with this model is that it is not proven that the branching ratio in the UV experiments corresponds to the ratio of unimolecular dissociation rates. At pressures >0.1 Torr, excitation to S_1 in D_2CO

Table IV-4. Parameters used in RRKM calculation of radical dissociation rates

C-D bond length (Å)	Moments of Inertia[a]					
	I_x		I_y		I_z	
	g cm^2 ($\times 10^{39}$)	AMU-Å^2	g cm^2 ($\times 10^{39}$)	AMU-Å^2	g cm^2 ($\times 10^{39}$)	AMU-Å^2
2.78	3.49	21.0	5.61	33.8	2.11	12.7
3.34	3.90	23.5	6.80	40.9	2.91	17.5

	Vibrational Frequencies[b]				
	ν_1	ν_2	ν_3	ν_4	ν_6
$\nu' = 0.7\ \nu_{D_2CO}$	1439	1360[c]	774	654	693
$\nu' = 0.8\ \nu_{D_2CO}$	1645	1530[d]	884	747	792

---

[a] Equilibrium geometry has C-D bond length = 1.116 Å, C-O bond length = 1.208 Å, D-C-D bond angle = 116° 31'. $I_x = 2.606 \times 10^{-39}$ g cm^2, $I_y = 3.200 \times 10^{-39}$ g cm^2, $I_z = 6.00 \times 10^{-40}$ g cm^2.

[b] Units for all frequencies are cm^{-1}. Reaction coordinate is ν_5.

[c] $\nu' = 0.8\ \nu_{D_2CO}$

[d] $\nu' = 0.9\ \nu_{D_2CO}$

Figure IV-6. The calculated RRKM dissociation rate constants for radical dissociation of D_2CO vs energy using a radical threshold of 89.6 kcal/mole. The critical configuration parameters used in the calculation are:

1) ——; $r = 3.34$ Å, $\nu' = 0.7\ \nu$.

2) .....; $r = 2.78$ Å, $\nu' = 0.7\ \nu$.

3) — — —; $r = 3.34$ Å, $\nu' = 0.8\ \nu$.

The upper dashed curve (—·—) is the RRKM molecular dissociation rate for a barrier of 86.2 kcal/mole. The squares and circles are calculated rates for parameter sets 2 and 3.

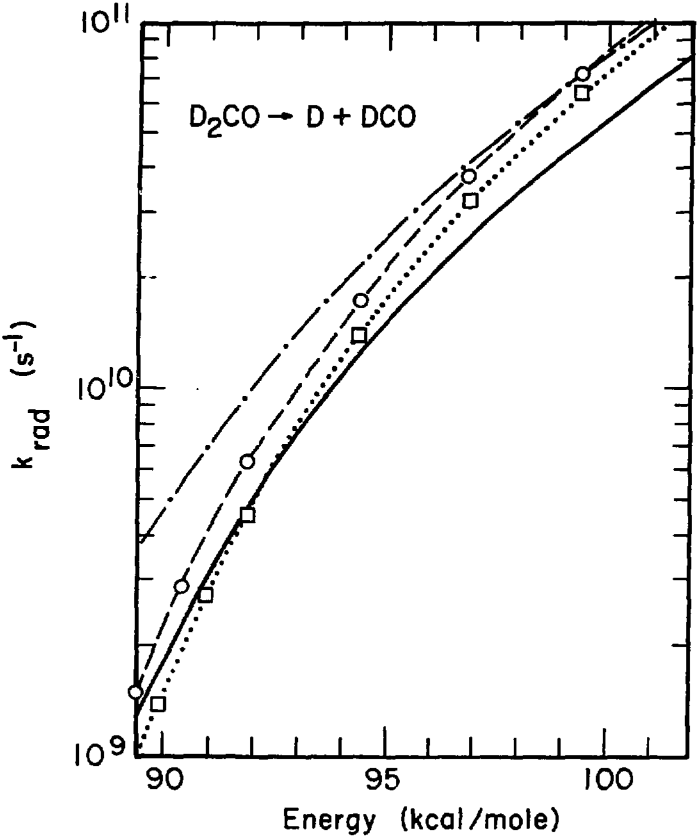
$D_2CO \rightarrow D + DCO$
10^{11}
10^{10}
10^{9}
k_{rad} (s^{-1})
90
95
100
Energy (kcal/mole)

XBL 811-7571

is followed by transition to an intermediate state I before dissociation to molecular products occurs.[28] Dissociation presumably[28] takes place through high vibrational states in S_0. One expects a branching between radical and molecular dissociation in S_0. It has not been determined, however, if radical products can additionally be produced by a direct route that bypasses the intermediate state. If such a pathway is important at the pressures used, it would create a second point of branching resulting in a larger k_{mol}/k_{rad} ratio being necessary to match the observed 40% radical quantum yield in the UV. Time-resolved, wavelength and pressure dependent studies of the rise of DCO product from UV photolyzed D_2CO will hopefully shed some light on this question. A direct, collisionless channel should be discernible from the pressure dependence of DCO production.

There is some uncertainty in the absolute magnitude of the radical dissociation rates due to uncertainty of the exact position of the radical threshold. The best thermodynamic valves are 89.2 ± 2 and 90.5 ± 1.6 kcal/mole from calculations by Walsh and Benson[29] and Warneck[30] and corrected by 2.3 kcal/mole for the different zero-point energies for the deuterated species. Clark _et al._[27] found that radical formation in the UV photolysis of D_2CO began between 87.6 and 89.4 kcal/mole above the ground state. The radical threshold for H_2CO was limited to the range 86 ± 1 kcal/mole by considering the results for different isotopes and zero-point energy changes. This corresponds to a radical threshold of 88.3 ± 1.3 kcal/mole for D_2CO. Calculations were performed at several radical thresholds in this range. Barrier heights calculated relative to the radical threshold eliminate the added uncertainty from the position of the radical threshold.

C. Results

A set of curves of calculated percent radical yield as a function of barrier heights is shown in Figure IV-7. Each point on a curve corresponds to a set of 3 rate equation calculations performed at photon energies 2.65, 2.70 and 2.75 kcal/mole in order to obtain the smooth distribution of total yield vs energy needed to accurately calculate the percentage radical yield. The calculations in this figure were performed for a radical threshold of 89.6 kcal/mole, total angular momentum $J = 0$, and different valves for the QC absorption cross section σ_{QC} and the energy per deactivation step ε_D. The radical dissociation rates were set as $k_{rad} = \frac{2}{3} k_{mol}$ according to the UV branching ratio. The barrier heights which gave a calculated 10% radical yield using values of σ_{QC} and ε_D which provide total yields between 2 to 25% (see Sec. IV-B.2) range from 1.7 to 4.4 kcal/mole below the threshold (ΔBT) for radical dissociation. The limiting QC absorption cross sections used, 2-8 x 10^{-20} cm^2, were restricted by the total yield constraint and the limiting 1000-5000 cm^{-1} collisional deactivation steps. The smallest absorption cross section which produced a minimum 1% dissociation yield with no collisional deactivation was 0.4 x 10^{-20} cm^2.

Larger QC absorption cross sections, hence larger uppumping rates, enable molecules to reach higher levels before dissociation becomes a competitive pathway. This results in the observed larger radical yields when larger σ_{QC}'s are used and predicts lower barriers. Increased collisional deactivation also results in an increased contribution from the radical channel and lower calculated barriers. Collisional deactivation at a gas kinetic hard sphere collision frequency effectively quenches molecules in the low energy part of the population distribution prohibiting

Figure IV-7. The calculated percent radical yield from rate equation calculations of D_2CO MPD as a function of barrier height. All calculations are performed with $J = 0$ and the radical threshold = 89.6 kcal/mole. The QC absorption cross section ($\times 10^{-20}$ cm^2) and the deactivation step size (in cm^{-1}) used were: ◇, 2.0, 1000; ○, 4.0, 1000; △, 4.0, 5000; □, 8.0, 5000.

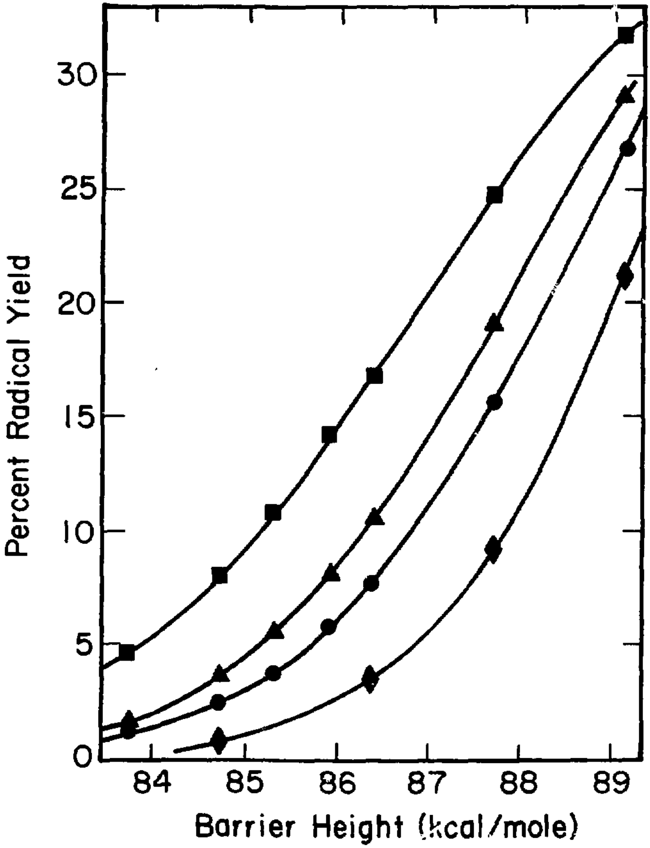
Percent Radical Yield
0
5
10
15
20
25
30
84
85
86
87
88
89
Barrier Height (kcal/mole)

XBL 811-7500

them from dissociating. Thus, in Figure IV-8, the population distribution for the calculation using a larger deactivation step size has a larger fraction of molecules at higher energies. Since the total yield is reduced, a larger fraction of the molecules that do dissociate were more strongly uppumped than without collisional deactivation, hence larger percentage radical yields are observed. Dissociation yields and calculated barrier heights are about twice as sensitive to changes of a factor of two in cross section as to factor of two changes in the deactivation step size between 1000 to 5000 cm^{-1}.

The results of calculations performed employing different absorption cross sections, deactivation step sizes, total angular momentum, radical thresholds and radical rate constants are tabulated in Table IV-5. For total angular momentum $J = 10$, the dissociation rates are a factor of 2 smaller than for $J=0$. The smaller dissociation rates in this case permit molecules to be driven to higher levels of excitation before dissociation becomes competitive. This reduces the importance of tunneling contributions to dissociation since it occurs at low excitation levels. The percent radical yield increases resulting in lower calculated barrier heights. Table IV-5 shows that the limiting barrier heights are shifted by about 0.5 - 1.0 kcal/mole to lower energy relative to the rotationless $J=0$ calculations.

Calculations performed with a radical threshold of 87.6 kcal/mole, the lower limit from the observations of Clark et al.,[27] exhibited limiting barrier heights that reproduce the 10% radical yield located 1.6 to 4.0 kcal/mole below the radical threshold for $J=0$. For $J = 10$, the limiting range is 2.4 to 5.3 kcal/mole below the radical threshold. These limiting values differ by at most 13% from the valves calculated for an 89.6 kcal/mole radical threshold. This indicates that the

Figure IV-8. The population distribution after 80 ns in rate equation calculations for $\sigma_{QC} = 4 \times 10^{-20}$ cm^2. The solid curve (left hand axis) is for a calculation using a deactivation step size of $\varepsilon_D = 5000$ cm^{-1}, the dashed curve (right hand axis) $\varepsilon_D = 1000$ cm^{-1}. The arrow shows the first vibrational level above the barrier.

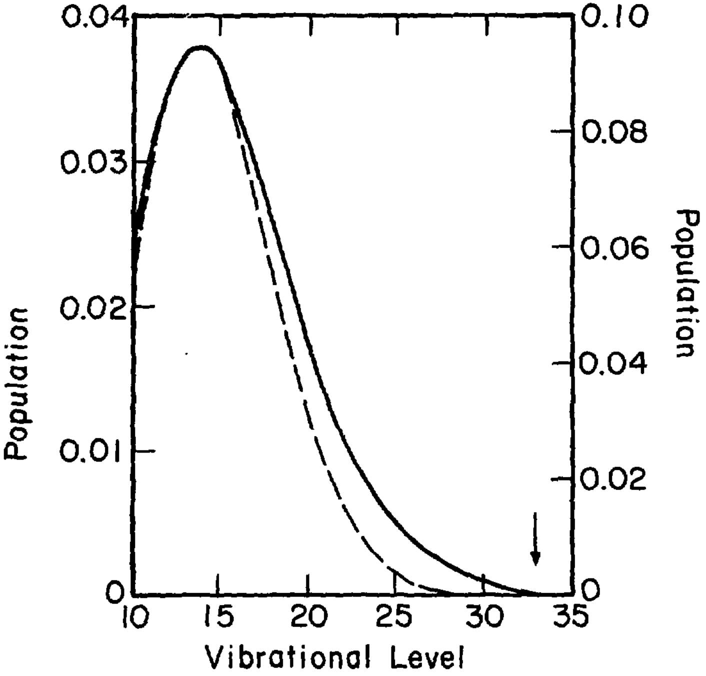
0.04
0.03
0.02
0.01
0
Population
0.10
0.08
0.06
0.04
0.02
0
Population
10
15
20
25
30
35
Vibrational Level

XBL 811-7505

Table IV-5. Calculated Barrier Heights from Rate Equation Model[a]

σ_{QC} (10^{-20} cm^2)	ϵ_D (cm^{-1})	J	Dissociation Yield (% in QC)	Radical Threshold (kcal/mole)	Barrier Height (kcal/mole)	ΔBT (kcal/mole)
$k_{rad} = \frac{2}{3} k_{mol}$						
2.0	1000	0	3.0	89.6	87.8	1.8
4.0	1000	0	32.6	89.6	86.6	2.8
4.0	5000	0	3.2	89.6	86.3	3.3
8.0	5000	0	22.1	89.6	85.1	4.5
2.0	1000	10	3.0	89.6	87.1	2.5
8.0	5000	10	22.2	89.6	84.0	5.6
2.0	1000	0	3.1	87.6	86.0	1.6
8.0	5000	0	22.2	87.6	83.6	4.0
2.0	1000	10	3.1	87.6	85.2	2.4
8.0	5000	10	22.2	87.6	82.3	5.3
2.0	2000[b]	10	4.3	89.6	87.2	2.4
2.0	2000[c]	10	11.2	89.6	87.5	2.1
2.0	2000[d]	10	19.8	89.6	87.6	2.0
2.0	1000[c]	10	24.1	89.6	87.7	1.9
1.0	1000[c]	10	1.7	89.6	88.7	0.9
$k_{rad} = k_{rad}^{RRKM}$[e]						
2.0	1000	0	3.2	89.6	87.9	2.1
8.0	5000	0	21.0	89.6	86.5	3.1
2.0	1000	10	3.1	89.6	86.9	2.7
8.0	5000	10	21.1	89.6	85.1	4.5

continued

Table IV-5 (continued)

σ_{QC} (10^{-20} cm^2)	ϵ_D (cm^{-1})	J	Dissociation Yield (% in QC)	Radical Threshold (kcal/mole)	Barrier Height (kcal/mole)	ΔBT (kcal/mole)
			$k_{rad} = k_{rad}^{RRKM}$[f]			
2.0	1000	0	3.2	89.6	87.5	2.1
8.0	5000	0	21.0	89.6	85.7	3.9
2.0	1000	10	3.1	89.6	86.5	3.1
8.0	5000	10	21.1	89.6	84.3	5.3

---

[a] Calculation use type I coupling, $E = 125\ J/cm^2$, QC onset at $v = 10$.

[b] Calculations use a collision frequency of 0.5 times the gas kinetic collision frequency, $k_{col} = 0.5\ k_{g.k.}$

[c] Calculations use $k_{col} = 0.3\ k_{g.k.}$

[d] Calculations use $k_{col} = 0.2\ k_{g.k.}$

[e] RRKM calculation with $r_{CD} = 3.34$ Å, $\nu' = 0.8\ \nu_{D_2CO}$

[f] RRKM calculation with $r_{CD} = 3.34$ Å, $\nu' = 0.7\ \nu_{D_2CO}$

calculated barrier position relative to the radical threshold is fairly insensitive to the total energy in this range.

Taking the limiting valves from Table IV-5 for calculations producing yields between 2 and 25%, the barrier to molecular products in D_2CO is estimated to lie between 1.6 and 5.6 kcal/mole (3.6 ± 2.0 kcal/mole) below the radical threshold. Using the limiting radical thresholds of Clark et al.,[27] this corresponds to between 82.0 and 87.9 kcal/mole (85.0 ± 3.0 kcal/mole) above the ground vibrational state of D_2CO. This is shown in the energy level diagram for D_2CO in Figure IV-9. The actual position of the barrier height might be expected to lie in the higher energy range (smaller ΔBT) since that corresponds to calculations using smaller absorption cross sections and deactivation rates. The estimated absorption cross section (Sec. IV-B.2) was 2×10^{-20} cm^2, the lowest value used in the calculations. Deactivation step sizes of between 1300-4000 cm^{-1} are the most commonly observed values[20] for collisions of highly vibrationally excited, small (6-10 atoms) hydrocarbons or their halogenated derivatives with similar molecules. Varying the deactivation step size in this range or varying the collision rate by a factor of 5, however, had little effect on ΔBT (see Table IV-5).

Extending the D_2CO results to H_2CO requires several zero-point energy corrections (see Fig. IV-5). Barrier heights calculated relative to the radical threshold need to be corrected for the difference in zero-point energies in the isotopic formyl radicals and the transition states to molecular products. This places the barrier in H_2CO 1.1 kcal/mole closer to the radical threshold than in D_2CO (ΔBT = 0.5-4.5 kcal/mole). The barrier height relative to the ground vibrational level of the isotopic formaldehydes is 1.2 kcal/mole lower in H_2CO than in D_2CO due to

Figure IV-9. An energy level diagram for D_2CO with the radical threshold at 88.3 kcal/mole and the barrier at 85.0 kcal/mole. The top of the barrier includes the transition state ZPE.

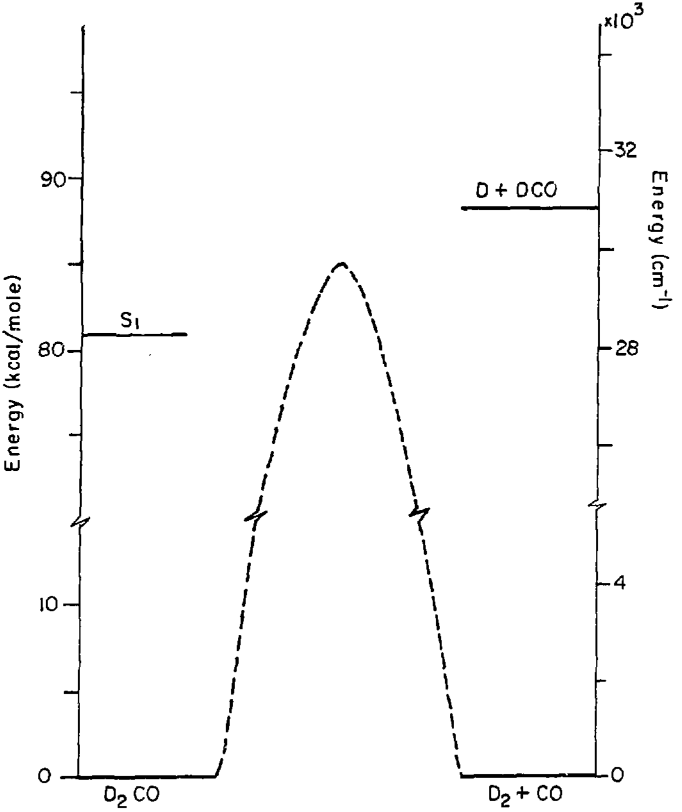
Energy (kcal/mole)
90
80
10
0
S₁
D₂CO
D + DCO
D₂ + CO
x10³
32
28
4
0
Energy (cm⁻¹)

XBL 811-5050

ZPE differences in the transition states and the molecular species. This gives a barrier height range of 80.8-86.7 kcal/mole or 83.8 ± 3.0 kcal/mole in H_2CO. The bare barrier height, the energy from the minimum to the saddle point of the formaldehyde potential energy surface is between 86.9 and 92.8 kcal/mole or 89.9 ± 2.9. This agrees quite well with the bare barrier height of 93.6 ± 5 kcal/mole calculated[5] by Goddard and Schaefer especially since their value should be considered an upper limit as MO calculations usually predict slightly high barrier heights.

D. Discussion

In evaluating the results of the rate equation calculations it is worthwhile considering the effects of the approximations used. The simplifications in the treatment of collisions employ a single deactivation term which is independent of total energy to account for all collisional effects in the QC. Collisional uppumping is accounted for in the magnitude of the deactivation step size. In the calculations, most dissociation occurred in the first few hundred ns of the pulse and no dissociation took place after the end of the pulse. The use of smaller deactivation step sizes or of a deactivation rate that is slower than the gas kinetic collision frequency (i.e., probability of energy transfer <1) would favor molecular dissociation and predict higher barriers.

In the calculations, coupling of molecules to the QC was terminated after the peak of the laser pulse. Molecules which enter the QC at later times are exposed to slower uppumping than those molecules that couple to the QC on or before the peak. The slower excitation rate would increase the contribution to total dissociation from the molecular channel. Failure to deconvolute the effects of the intensity distribution in the focal volume could also affect the calculated branching ratio. Use of the intensity scaled focal volume tries to correct for this. Dissociation occurring outside of the calculated focal volume would take place at lower power densities enhancing molecular dissociation, however, the dissociation yield in the low intensity region is quite low. All of these effects would have no more than a 1.0 kcal/mole effect on ΔBT, however, they do favor the barrier lying in the upper part of the predicted range. In addition, neglect of radical recombination (D + DCO → D_2 + CO) makes the branching ratio used a lower limit. This could result in, at most, a 20% larger radical yield than the value used (see Fig. III-17), giving a branching ratio of 0.12 and higher calculated barrier heights. Fitting the rate equation calculations to this value shifts the barrier up by 0.3 kcal/mole. Neglect of the mode locked spikes in the laser pulse counters these effects.

The use of RRKM theory to describe UV dissociation of formaldehyde has been questioned[27] on the basis of different barriers for radical and molecular dissociation in light of the constant radical/molecule branching ratio observed at energies above the radical threshold. As seen earlier, however, RRKM calculations for the radical channel predict rates increasing with a slope similar to that for the molecular channel using an appropriate barrier height. The faster rise in the radical rates near the radical threshold would be somewhat lessened in experiments by the thermal population distribution.

Weisshaar[31] has suggested that non-RRKM behavior in H_2CO might be able to help explain the widely varying lifetimes observed for single rotational lines in S_1 formaldehyde at energies below the radical threshold. Such an explanation requires a manifold of "slow" states which do not couple strongly to product states (i.e., little reaction coordinate character, long lifetime) and a much more sparse set of "fast" states which are strongly coupled to the reaction coordinate. Under the collisional conditions employed in these IR experiments, equilibration between these states should be rapid since slow and fast states would be separated by 10^{-1}-10^{-3} cm^{-1}. Long range collisions should affect equilibration. In the limit of high pressures, collisions provide rapid energy redistribution substituting for collision-free intramolecular energy randomization and the RRKM rate constant is obtained. At pressures where equilibration is not as rapid as the dissociation rate of the fast states, population remains in slow states for times longer than the RRKM lifetime. Dissociation rates slower than the RRKM rate would be observed.

In order to check the RRKM description in the pressure range of interest (5-10 Torr), the RRKM rates were used in the rate equation model to try to fit the observed[27] wavelength dependence of the total quantum yield in UV photolyses. Clark et al observed that in D_2CO the total quantum yield rises from zero at the S_1 origin to almost unity just below the radical threshold. In H_2CO, a quantum yield of 0.7 is observed at the S_1 origin and it quickly approaches a valve of 1.0. It is possible that these quantum yield dependences on excitation wavelength arise from the competition between collisional deactivation and dissociation at the energies reached by UV excitation. This is the same energy region probed by the IR MPD branching ratio experiments. If the RRKM rates can describe this process using a barrier height consistent with that obtained in IR MPD experiments, these rates would appear to provide an adequate and unified description of dissociation in both cases. The similar NO effect in both cases argues for similar dissociation dynamics.

The rate equation calculations used started with all population in an S_0 state (fast, internal conversion is assumed) at the energy corresponding to the monochromatic excitation frequency. Collisions and dissociation were then allowed to compete as in the previous calculations with deactivation proceeding in 1000 cm^{-1} steps. Dissociation rates corresponding to different barrier heights were used until agreement with the observed total quantum yields were achieved. Since there is no competing uppumping process, the calculations are simplified and are described by the equation

$$\phi^T = f_1 + f_2\ (1-f_1) + f_3\ [1-f_2(1-f_1)] + \ldots$$

$$\phi^T = f_1 + f_2 g_1 + f_3 g_2 + \ldots$$

$$\phi^T = \sum_i f_i\ g_{i-1}$$

where $f_i = \frac{k_i}{k_{col}+k_i}$, k_i is the RRKM dissociation rate from level i with level 1 being the directly excited level and the index i increasing towards lower energy states, and $g_i = i - f_i\ g_{i-1}$ with $g_o \equiv 1$. The first term, f_1, typically accounts for about 98% of ϕ^T. Dissociation rates used for H_2CO were calculated using transition state frequencies calculated under the same level of approximation as those used in calculating the D_2CO rates.

The fits observed by this procedure are shown in Figure IV-10. The D_2CO data is fit well with barrier heights of 87.2 kcal/mole using rates for J=0 and 86.4 kcal/mole for J = 10. These valves are in very good agreement with the calculated barriers from the MPD branching ratio experiments. Accurately fitting the H_2CO results is more difficult since only one point is available to define the curvature. The fit gives a barrier in H_2CO of 82.9 kcal/mole well within the uncertainty range of the barrier predicted by IR MPD but a few kcal/mole lower than expected just from ZPE differences in the barrier calculated for D_2CO in the same manner. The H_2CO calculation should be less reliable, however, due to

Figure IV-10. Rate equation calculation fits to the UV photolysis data of Clark *et al.*[27] The D_2CO data, taken at 5 Torr, is fit with the barrier at 87.2 kcal/mole and J = 10. The H_2CO data, taken at 10 Torr, is fit with the barrier at 82.9 kcal/mole and J = 10. R. T. denotes the radical threshold.

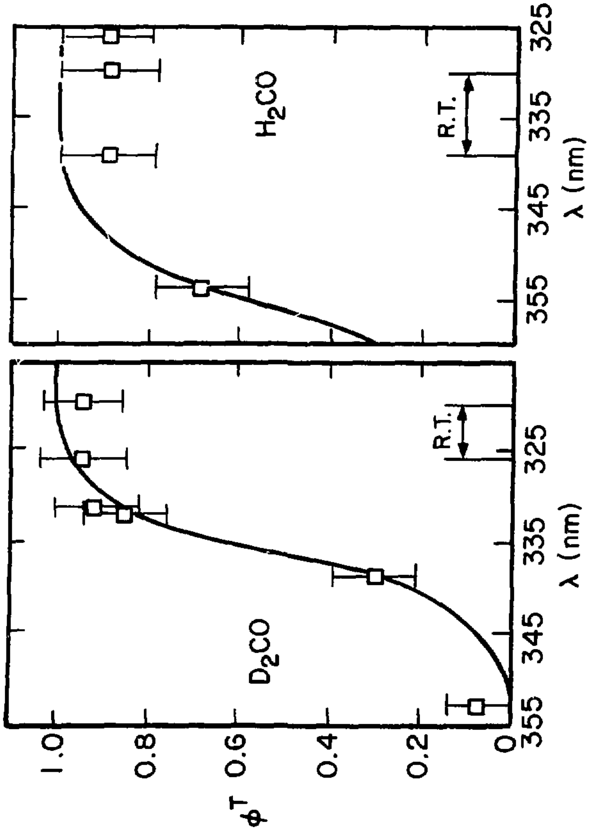
ϕ^T
1.0
0.8
0.6
0.4
0.2
0
D$_2$CO
H$_2$CO
R.T.
R.T.
355
345
335
325
λ (nm)
355
345
335
325
λ (nm)

XBL 811-7502

the lack of points to fit. Fitting the H_2CO data to the top of the error bar at 353 nm lowers the calculated barrier by 0.5 kcal/mole.

The general agreement between IR and UV experiments indicates that the RRKM description is applicable to formaldehyde photochemistry in the pressure range of several Torr. A unified description of dissociation occurring through high vibrational levels of S_0 is also supported.

The position of the molecular barrier and the observed competition between molecular and radical dissociation on the ground state surface has important implications for the interpretation of formaldehyde shock tube data. The identification of radical dissociation in shock tube pyrolyses was established by Gay et al.[32] They observed an induction period in the formaldehyde decay indicating a radical chain process taking place. Scrambling was also observed in the hydrogen molecules produced in the pyrolysis of an equimolar mixture of H_2CO and D_2CO. An induction period in the H_2CO decay was also observed by Dean et al.[13] who monitored the loss of H_2CO by the decay of its 3 μm IR fluorescence. Dean et al. found that they could fit their observations of formaldehyde disappearance with various sets of rate constants in a four reaction mechanism not including molecular dissociation. In a comment to that paper, Just[13] pointed out that it is possible to reinterpret these data with the inclusion of a molecular channel having $k_{mol} = 10 \times k_{rad}$ and a faster rate for $H + H_2CO \rightarrow H_2 + HCO$.

Only the latter interpretation of the shock tube results is consistent with the predominance of molecular dissociation seen here in MPD. Although excitation in MPD is localized in the vibrational degrees of freedom compared to thermal excitation in shock tubes, the branching ratio for dissociation on the ground state potential surface should be determined for the most part by the proximity of the barrier height to the radical threshold and the dissociation rates in each channel. This separation is slightly smaller in H_2CO than in D_2CO but the larger dissociation rates for H_2CO compared to D_2CO (due to better tunneling as a result of the lighter H atom) should keep the branching ratio in an experiment using thermal excitation in the same range. Excitation rates in shock tubes will not be greater than optical pumping in MPD so the molecular dissociation channel will not be bypassed.

Careful shock tube experiments in which radical and molecular products are simultaneously or independently measured might, with a rate equation model, provide a more precise measurement of the barrier position. In any event, it is clear that the barrier to molecular dissociation and the radical threshold are quite close and that molecular dissociation plays an important role in the dissociation of formaldehyde on its ground state potential surface.

REFERENCES

1. E. R. Grant, P. A. Schulz, Aa. S. Sudbø, Y. R. Shen and Y. T. Lee, Phys. Rev. Lett. 40, 115 (1978); P. A. Schulz, Ph.D. Dissertation, University of California, Berkeley, 1979.

2. W. Fuss, Chem. Phys. 36, 135 (1979).

3. J. L. Lyman, J. Chem. Phys. 67, 1868 (1977).

4. a) W. H. Miller, J. Am. Chem. Soc. 101, 6810 (1979);
   b) unpublished results.

5. J. D. Goddard and H. F. Schaefer, III, J. Chem. Phys. 70, 5117 (1979).

6. S. K. Gray, W. H. Miller, Y. Yamaguchi, and H. F. Schaefer, to be published.

7. C. E. Treanor, J. W. Rich, and R. G. Rehm, J. Chem. Phys. 48, 1798 (1968); S. Mukamel and J. Ross, J. Chem. Phys. 66, 5235 (1977).

8. I. Shamah and G. W. Flynn, J. Chem. Phys. 69, 2474 (1978).

9. K. Yamada, T. Nakagawa, K. Kuchitsu, and Y. Morino, J. Mol. Spectrosc. 38, 70 (1971).

10. T. Nakagawa and Y. Morino, J. Mol. Spectrosc. 38, 84 (1971).

11. D. Coffey, Jr., C. Yamada and E. Hiruta, J. Mol. Spectrosc. 64, 98 (1977).

12. H. G. Schecker and W. Jost, Ber. Bunsenges Physik. Chem. 73, 521 (1969).

13. A. M. Dean, B. L. Craig, R. L. Johnson, M. C. Schultz, and E. E. Wang, Seventeenth Symposium (International) on Combustion, (Combustion Institute, 1978) p. 577.

14. D. Proch and H. Schröder, Chem. Phys. Lett. 61, 426 (1979); D. K. Evans, R. D. McAlpine and F. K. McClusky, Chem. Phys. Lett. 65, 226 (1979).

15. G. Koren, M. Okon and U. P. Oppenheim, Opt. Commun. 22, 351 (1977).

16. G. Koren and U. P. Oppenheim, Opt. Commun. 26, 449 (1978).

17. H. L. Dai, A. H. Kung, and C. B. Moore, J. Chem. Phys. (in press).

18. I. C. Hisatune and D. F. Eggers, Jr., J. Chem. Phys. 23, 487 (1955).

19. P. J. Robinson and K. A. Holbrook, Unimolecular Reactions (Wiley, New York, 1972).

20. D. C. Tardy and B. S. Rabinovitch, Chem. Reviews 77, 369 (1977).

21. H. S. Johnston, Gas Phase Reaction Rate Theory (Ronald, New York, 1966), pp. 40-44.

22. G. Herzberg, Infrared and Raman Spectra of Polyatomic Molecules (Van Nostrand-Reinhold, New York, 1945), p. 206.

23. J. L. Duncan and P. D. Mallinson, Chem. Phys. Lett. 23, 597 (1973).

24. W. Wong and R. A. Marcus, J. Chem. Phys. 55, 5625 (1971).

25. D. L. Bunker and M. Pattengill, J. Chem. Phys. 48, 772 (1968).

26. K. Takagi and T. Oka, J. Phys. Soc. Jap. 18, 1174 (1963).

27. J. H. Clark, C. B. Moore, and N. S. Nogar, J. Chem. Phys. 68, 1264 (1978).

28. P. L. Houston and C. B. Moore, J. Chem. Phys. 65, 757 (1976).

29. R. Walsh and S. W. Benson, J. Am. Chem. Soc. 88, 4570 (1966); S. W. Benson, Thermochemical Kinetics (Wiley, New York, 1968).

30. P. Warneck, Z. Naturforsch. Teil A 26, 2047 (1971); 29, 350 (1974).

31. J. C. Weisshaar, Ph.D. Dissertation, University of California, Berkeley, 1979.

32. I. D. Gay, G. D. Glass, G. B. Kistiakowsky and H. Niki, J. Chem. Phys. 43, 4017 (1965).

CHAPTER V

THE UNIMOLECULAR DECOMPOSITION OF TETRALIN

A. Introduction

The identification of the lowest energy reaction channel in unimolecular decompositions can often be complicated by heterogeneous surface reactions. Surface catalyzed reactions can often mask the true, low energy, homogeneous gas phase pathway. This is the case in the thermal chemistry of the aromatic hydrocarbon tetralin (1). Recent experiments[1] motivated by interest in the fate of hydrogen donors which are used as recycle liquids in the solvent refining of coal have resulted in conflicting data[1a,1e] regarding the homogeneous thermal reactivity of tetralin. Dehydrogenation is the major reaction channel observed in flow pyrolysis experiments.[1,2] The observed product distributions appear to depend on the presence of hydrogen, hydrogen acceptor molecules, different types of reactor surfaces and surface history. Two techniques are employed here, both using TEA CO_2 laser excitation to energize tetralin molecules in the absence of hot, potentially catalytic surfaces and study the competition between reaction channels.

IR multiphoton dissociation (MPD) and SiF_4 - sensitized pyrolysis were used to study the truly homogeneous gas phase reactions of tetralin. The activation energies for the unimolecular reactions of tetralin are about 70 kcal/mole. MPD provides direct excitation of tetralin as energy is deposited in the molecule's vibrational modes. When low laser fluence is used and the uppumping rate does not greatly exceed the dissociation rate, dissociation primarily occurs through the lowest energy dissociation channel. When the uppumping rate is increased, higher energy channels become more accessible. Sensitized pyrolysis employs a non-reacting gas to absorb the laser energy. SiF_4, a strong absorber of CO_2 laser radiation with a large bond dissociation energy, is an ideal sensitizer and is used here. Tetralin molecules in the volume irradiated by the laser beam are thermally excited by collisional energy transfer from SiF_4 while the cell walls remain at room temperature. The temperature reached in the heated gas can be altered by varying the incident laser intensity or the gas mixture in the cell. The product distribution can thus be studied as a function of temperature and the lowest energy reaction pathways discerned. MPD and SiF_4 - sensitized pyrolysis have produced similar product distributions in the dissociation[3] of $CHClF_2$.

Six major products are observed in the conventional flow pyrolysis[2] of tetralin as well as in MPD and SiF_4 - sensitized pyrolysis. These products, benzocyclobutene (2), styrene (3), o-allyltoluene (4), indene (5), 1,2-dihydronaphthalene (6), and naphthalene (7), are shown in Figure V-1. An additional product, phenylacetylene, is observed in MPD experiments. The three major reaction channels observed in the thermal decomposition of tetralin are listed in Figure V-2. The first process is ethylene loss by a retro-Diels-Alder reaction producing 2 plus ethylene. The second channel shown is dehydrogenation, producing 6 and H_2. Finally, cleavage of a C-C bond in tetralin can result in disproportionation producing 4, an isomer of tetralin. The SiF_4 - sensitized pyrolysis experiments presented here provide the first identification of disproportionation as a primary decomposition pathway in tetralin. This was possible since during sensitized pyrolyses, the gas was heated for only a few ms, reducing the extent of secondary decomposition relative to that observed in conventional pyrolyses.

Figure V-1. The major products of the thermal dissociation of tetralin (1) are shown. They are benzocyclobutene (2), styrene (3), o-allyltoluene (4), indene (5), 1,2-dihydronaphthalene (6), and naphthalene (7).

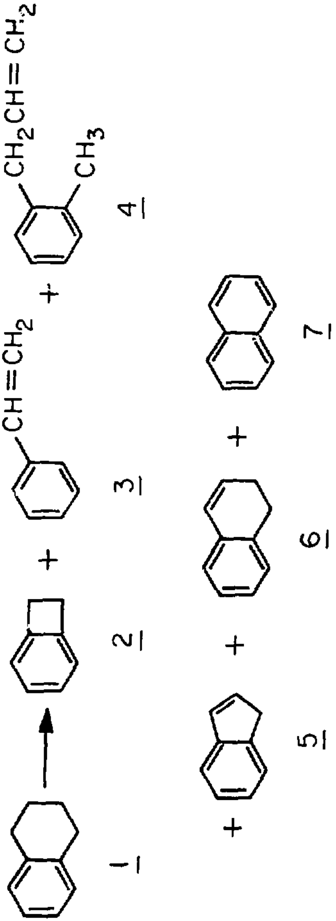

XBL 811-5038

Figure V-2. The thr [illegible] thermal dissociation pathways of tetralin are shown. They are ethylene-loss (retro-[2 + 4]cleavage), dehydrogenation, and disproportionation.

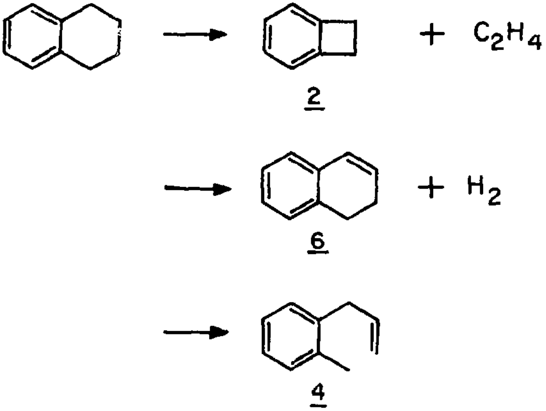

XBL 811-5060

The mechanisms and the relative energetics of the above reaction pathways were studied using MPD and SiF_4 - sensitized pyrolysis. In order to judge the competition between reaction channels, all of the products resulting from a particular pathway must be accounted for. The primary products 2, 4, and 6, all decompose under the sensitized pyrolysis conditions. The resulting secondary products, 3, 5, and 7, must be grouped with the appropriate parent molecule in order to determine the contribution of each reaction channel to the total dissociation yield. The details of the dissociation mechanism were investigated by photolyzing or pyrolyzing several deuterated isotopomers of tetralin. Appropriate labelling of the tetralin to be dissociated provided mechanistic information regarding different reaction pathways. The deuterated species used were 1,1,4,4-tetradeuteriotetralin (tetralin-d_4), *cis*-1,2-dihydrotetralin-d_{10} (tetralin-d_{10}) and perdeuteriotetralin (tetralin-d_{12}). These molecules are shown in Figure V-3.

B. Experimental

1. Sample Handling

In addition to the experimental details in Chapter II, there are many details specific to the tetralin experiments. The low vapor pressure of tetralin at 295 K (~0.4 Torr), its solubility in hydrocarbon greases, and its penchant for sticking to surfaces dictated many of the experimental conditions and procedures employed. Extreme care was taken to avoid contamination of starting materials and products by molecules desorbing from the walls of the vacuum system. A glass vacuum system with all greaseless stopcocks (Kontes 4 mm) and a base pressure of $\sim 10^{-6}$ Torr was used. No hydrocarbon greases were used. O-ring joints, silicone grease (Dow Corning 970 V) or black wax were used where needed.

Figure V-3. The isotopomers of tetralin used in labelling experiments. The molecules are 1,1,4,4-tetradeuteriotetralin (tetralin-d_4), *cis*-1,2-dihydrotetralin-d_{10} (tetralin-d_{10}) and perdeuteriotetralin (tetralin-d_{12}).

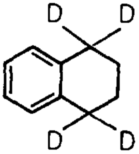

Tetralin - d_4

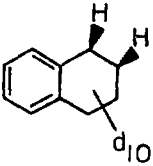

Tetralin - d_{10}

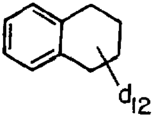

Tetralin - d_{12}

XBL811-5061

The vacuum manifold was warmed with heating tape to 80°C or higher when not being used to expedite desorption of molecules from the walls. Two liquid nitrogen (LN_2) cooled traps, one directly after the diffusion pump and the other adjacent to the manifold were used. The latter significantly helped in preventing contamination of samples or products that were vacuum transferred through the manifold. Since SiF_4 reacts quickly with water to produce HF, all surfaces which came in contact with SiF_4 were heated under vacuum to remove adsorbed water. The vacuum line manifold was removed, cleaned in Chromerge solution (a saturated solution of $Na_2Cr_2O_7$ in H_2SO_4) and baked out between the series of experiments using tetralin-h_{12}, tetralin-d_4 and tetralin-d_{10}. Pressures were measured with a capacitance manometer (MKS Baratron 222 AHS).

The photolysis cells used in all tetralin experiments contained at least one sidearm which could be closed off by a stopcock. MPD experiments were carried out in the photolysis cells described in Chapter III. Sensitized pyrolyses were all performed in 4.5 cm diameter pyrex cells. The cells were either 3.85 or 4.00 cm long except when a 1.0 cm long cell was used to study the effect of the cell surface area on the product distribution. All cells had two polished NaCl or KCl windows affixed parallel to one another and perpendicular to the cylinder axis with epoxy (Eccobond 45). Different cells were used for each tetralin isotope used. A similar 4.00 cm long cell equipped with 2.0 cm diameter NaCl windows above and below the laser beam was used for viewing infrared fluorescence.

The sample handling procedure for sensitized pyrolysis experiments was to load a given pressure of SiF_4 (from 5 to 10 Torr) into the cell, freeze the SiF_4 into the sidearm with LN_2, and close the sidearm stopcock.

NO, when used, was then added to the cell and frozen into the sidearm which contained the SiF_4. After pumping out the cell, tetralin (usually 0.325 Torr) was added to the cell. The sidearm was warmed and opened allowing SiF_4 to expand into the cell. Five minutes were allowed for equilibration of the gases before pyrolysis was initiated. If tetralin was frozen into the sidearm, the high pressure of SiF_4 relative to the tetralin would trap the latter and droplets of tetralin could be seen in the sidearm. Tetralin in the main manifold was not refrozen into the sample holder to prevent contamination. Some pyrolysis cells had an additional sidearm containing a supply of tetralin so cells could be filled directly, eliminating unnecessary contact with the vacuum manifold. In those cases, the cells were filled with the vapor pressure of tetralin at 295 K (~0.4 Torr) without measuring the exact pressure with the capacitance manometer. These experiments were concerned mainly with the distribution of product isotopomers so it was not necessary to know the precise tetralin pressure. Tetralin samples were degassed by repeated freeze-pump-thaw cycles prior to use.

After equilibration of the gases, the gas mixture was irradiated (see Sec. B-2). Condensible materials were frozen into the sidearm with LN_2 following the pyrolysis. When non-condensible products were analyzed, they were either directly injected into a mass spectrometer or sampled for analysis by gas chromatography (GC) with a gas syringe (Precision Sampling, Pressure-Lok Series "A", 1 cc) through a septum placed over the cell outlet joint. The volume between the septum and the cell was flushed with nitrogen. The cell sidearm was then warmed with a dry ice-isopropanol bath (195 K). SiF_4 and other gases were either pumped away or collected with LN_2 for GC analysis. The remaining contents of the cell were transferred to a LN_2 cooled collection tube containing 20 μl of n-hexane solvent. The n-hexane was previously transferred by condensing the n-hexane vapor (273 K) in the vacuum manifold into the collection tube with LN_2. The collection tube consisted of a 5 cm long piece of 2 mm i.d. pyrex tubing with a 14/20 female taper joint on top. Some collection tubes contained an additional arm containing a 14/20 female joint which was sealed during product collection. When several tetralin isotopes were used simultaneously on the vacuum line, individual transfer manifolds were used to vacuum transfer materials from the cell to the collection tube.

The sample handling for SiF_4 - sensitized pyrolyses of benzocyclobutene, o-allyltoluene and 1,2-dihydronaphthalene were as described above, simply substituting the molecule to be pyrolyzed for tetralin. Sample handling for tetralin MPD experiments was similar, just omitting the SiF_4 steps.

2. Analysis

The solutions of tetralin and its decomposition products dissolved in hexane were analyzed by GC or coupled GC-mass spectroscopy (GC-MS). An internal standard, 1 μl of n-undecane solution in n-hexane (either 0.018 or 0.058 M), was added to the solution with a syringe before GC analysis. Samples for GC analysis were taken from the collection tube with a syringe by several techniques: 1) A 14/20 teflon cap (Mininert valve) which was closed in one position and revealed a septum in the open position was placed in the second 14/20 outlet of the collection tube on those tubes so equipped. Samples were removed through the septum. 2) The collection tube was vented with N_2 and samples taken through a septum placed in one of the taper joints. 3) The 2 mm tubing was sealed off (by melting the glass) with a torch while the contents remained frozen in the bottom of the tube at 77 K. The glass seal was broken and the sample solution exposed to the atmosphere when sampled by a syringe. Using this technique, samples could be stored at 273 K for several days before analysis. These sampling techniques were used interchangeably. The entire collection and sampling technique was checked to be quantitative by transferring and analyzing known amounts of tetralin, styrene and 1,2-dihydronaphthalene.

GC analyses were performed on a Perkin Elmer Sigma 3 gas chromatograph using a 250 ft x 1/16 in o.d. stainless steel OV-17 wall coated open tubular (WCOT) column (Column I) and flame ionization detection (FID). The column temperature was programmed as follows: 110°C, 12 min; increase at 2°/min for 5 min; 120°C, 35 min. Injections of 0.06 μl were made with a 1 ul syringe (Hamilton #7101) into the injector port kept at 175°C. The He carrier gas flow rate was 10 ml/min. GC peaks were integrated with a Spectra-Physics Autolab System I computing integrator interfaced to the GC. A sample chromatogram is shown in Figure V-4. At least two injections of each sample were made and the product signals relative to either the tetralin or internal standard signals agreed from injection to injection to within ±3%. Results for the repetition of an experiment agreed to within ±5%. GC peaks were corrected for the FID response of each compound. GC analyses of gaseous ethylene and acetylene products were performed using a 10 ft x 1/8 in o.d. stainless steel, 100/120 mesh Poropak T column.

Isotopic analysis and product identification was achieved by GC-MS analysis on a Finnigan 4000 GC-mass spectrometer. All GC-MS analyses were performed with either a 30 m or 60 m glass capillary SP 2250 WCOT column and an electron energy of 20 eV to limit fragmentation. Mass

Figure V-4. A sample chromatogram from an SiF_4 - sensitized pyrolysis of tetralin. The off-scale peak is the n-hexane solvent. The internal standard peak is designated by S.

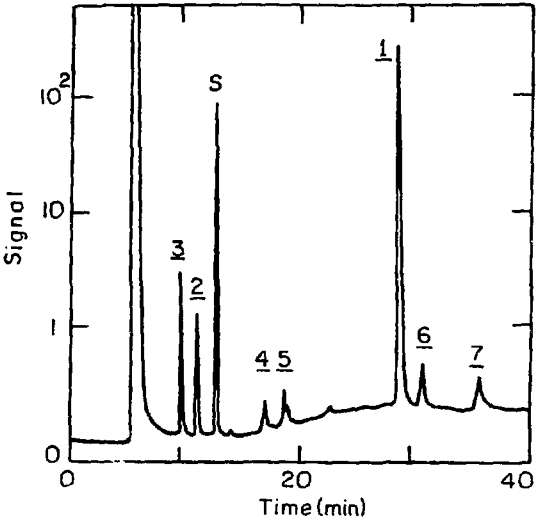

XBL 811-5043

spectral analyses of gaseous products were performed on an AEI-MS 12 mass spectrometer using a 20 eV electron energy. The response of H_2 and D_2 were calibrated with known samples of pure H_2, D_2 and mixtures of these two gases.

Infrared spectra of tetralin were recorded with a Nicolet Model 7199 FTIR. Spectra were taken of a liquid smear of tetralin between two NaCl plates and of gas phase tetralin (vapor pressure at 295 K, ~0.4 Torr) in a multiple pass cell (Wilks 20 m) using a path length of 9.75 m.

Infrared fluorescence from SiF_4 was observed using a LHe cooled Cu:Ge detector (see Chapter II). Fluorescence was observed in the 2000 cm^{-1} region through a W 4741-4 filter, peak transmission of 88% at 2110 cm^{-1}, 10% power points at 1850 and 2430 cm^{-1}, and 1% power points at 1805 and 2460 cm^{-1}. Fluorescence was collected with a CaF_2 lens as described in Chapter III. In order to observe fluorescence at all frequencies above ~700 cm^{-1}, the CaF_2 lens was replaced by a 5.0 cm diameter, f/1 NaCl lens. All CaF_2 and MgF_2 windows were removed from in front of the detector and replaced by a cell with NaCl windows containing 200 Torr SiF_4. The scattered light signal was still very large.

3. Materials

Tetralin-h_{12} (Eastman Practical Grade) was purified by preparative GC on a 15 foot x 3/8 in o.d. stainless steel column of 20% OV-17 on 60/80 mesh Chromosorb P-AW/DMCS. Styrene was from MCB and 1,2-dihydronaphthalene (Aldrich) was purified by preparative GC on Column I. Benzocyclobutene, o-allyltoluene and all of the deuterated isotopomers of tetralin used were prepared by Paul Comita.[4] The percent deuterium incorporation in these isotopomers were: tetralin-d_4, 98.7%; tetralin-d_{10}, 97.8%; and tetralin-d_{12}, 98.1%. SiF_4 (Matheson) was distilled from an n-pentane slush (142 K) to LN_2 (77 K) in order to remove any HF impurity.

The SiF_4 was stored in a well-flamed pyrex bulb. Nitric oxide was purified as described in Chapter III. The n-undecane (Aldrich) was washed with $H_2SO_4/KMnO_4$ and triply distilled. Hydrogen (Matheson), deuterium (Matheson, 99.6% D) and n-hexane (Aldrich) were used without further purification. GC analyses showed all samples, solvents and standards to be >99.99% pure.

4. Photolysis and Pyrolysis

A schematic diagram of the experimental arrangement for the SiF_4 - sensitized pyrolyses is shown in Figure V-5. Pyrolyses of tetra[illegible]-d_{10} and tetralin-h_{12}-tetralin-d_{12} mixtures were performed with the [illegible]er internal iris set at 0.8 cm. No external iris was used. All other experiments used a 1.2 cm internal iris with a 0.7 cm external iris to define the incident beam size. The former technique generated a much more reproducible, well defined, near Gaussian beam (see Fig. II-1) while 0.2 cm (FWHM) wide spikes resulting in 30% fluctuations in amplitude were seen across the profile of the latter. The CO_2 laser was operated on the P(40) line at 1027.4 cm^{-1}. The unattenuated laser output was about 0.30 J/pulse in a 0.7 cm diameter beam. Attenuation was performed with a 4 cm long gas cell filled with 0 to 10 Torr of SiF_4. The laser beam was not focused. The incident energies used ranged from 0.11 to 0.27 J/pulse. The maximum fluence and power density were 0.7 J/cm^2 and 3.5 MW/cm^2 respectively.

A small portion of the laser energy (~10%) was directed into a Scientech power meter (Model 36-0001) PM 1 by a 4 mm thick polished NaCl flat (BS). The reading from PM 1 was used as measurement of the laser power in order to normalize the total energy reaching PM 2 (Scientech Model 38-0101). The output from each power meter was recorded on a dual pen chart recorder (Leeds and Northrup) throughout the pyrolysis. Prior

Figure V-5. A schematic diagram of the apparatus used for SiF_4-sensitized pyrolysis experiments. The iris (0.7 cm diameter) is designated by I, A is the attenuation cell, BS is the NaCl beam splitter and PM 1 and PM 2 are power meters.

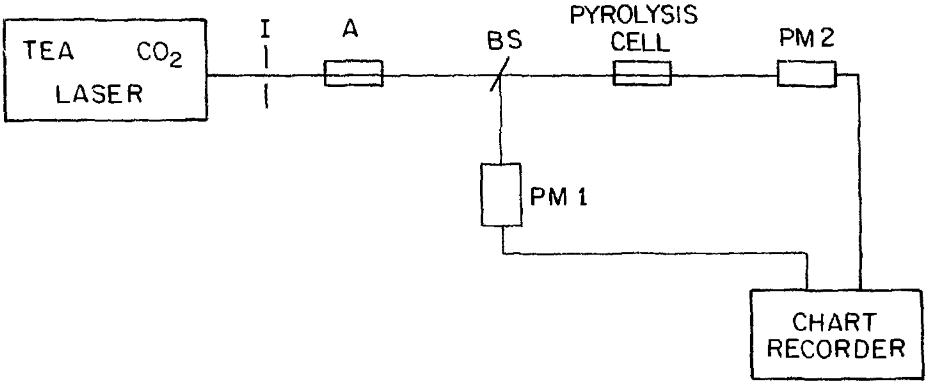

XBL 811-5062

to each pyrolysis, I_0, the energy reaching PM 2 with no cell in the beam path was measured.

During SiF_4 - sensitized pyrolysis, the laser beam passed through the center of the pyrolysis cell and irradiation continued until the desired conversion of starting material, between 1 to 10%, was achieved. This typically required 200 to 2000 pulses, depending on the laser intensity and the gas mixture in the cell. The incident energy (PM 1) and the energy transmitted through the cell (PM 2), I_T, were monitored throughout the pyrolysis. The average laser power was maintained constant to within ±5% during the course of a pyrolysis. Pyrolyses were performed at a laser repetition rate of either 1.00 or 0.87 Hz.

After a pyrolysis the laser beam was blocked from the pyrolysis cell and the condensible materials in the cell frozen into the sidearm with LN_2. Care was taken not to touch the cell or close the stopcock during this process so the empty cell transmission, I_c, could be measured with the cell in the exact position as it was during the pyrolysis. Finally, the pyrolysis cell was removed and the incident laser power and the beam splitter calibration measured.

MPD experiments were performed with an arrangement similar to that shown in Figure V-5 except that the beam splitter (BS) is replaced by a 15 cm focal length NaCl lens and the iris was removed. The $\frac{1}{e}$ beam waist at the focus was 0.13 cm and the focus was approximately at the center of the cell. Photolyses were performed at 946.0 cm^{-1}. The laser beam was attenuated with an SF_6 gas cell (10 cm long, NaCl windows, 0-25 Torr SF_6).

C. SiF_4 - Sensitized Pyrolysis

1. Introduction

The sensitized pyrolysis technique has been employed in several systems.[2-8] This technique enables the use of intense lasers to excite molecules which do not themselves absorb the laser radiation. Both pulsed[2-7] and continuous-wave[8] (CW) CO_2 lasers have been used as excitation sources. Several sensitizing gases (SF_6, CH_3F, NH_3, and SiF_4) have also been employed.[2-8] SiF_4 is an excellent sensitizer due to its large absorption coefficient in the region of the 9 μm CO_2 laser transition and to the large F_3Si-F bond dissociation energy (129 kcal/mole). SiF_4 has been found to be unreactive in the presence of many organic molecules under irradiation conditions similar to those employed here.[3,6] Tetralin does not absorb at the laser frequency (1027.4 cm^{-1}) used to excite SiF_4.

The absorption coefficient of SiF_4 increases with increasing SiF_4 pressure between 5 to 10 Torr with the laser intensity (~1 MW/cm^2) used (Fig. V-6). The fraction of the incident energy absorbed by SiF_4 increased from about 25% to 30% as the laser energy decreased from 0.2 to 0.1 J/pulse, probably a result of saturation. These characteristics of SiF_4 absorption have been previously observed.[3] Typically, 25% of the incident energy is absorbed by SiF_4 in these experiments. Stronger absorption is undesirable in order to limit the non-uniformity of the distribution of absorbed energy along the length of the cell.

In order to investigate the competition between reaction channels of tetralin decomposition as a function of excitation energy in SiF_4-sensitized pyrolyses, a means for determining the quantity of energy absorbed per pulse is needed. The following sub-sections detail the calculations performed to determine the energy absorbed per pulse as well as

Figure V-6. The absorption coefficient ($\log_e$) of SiF_4 at 1027.4 cm^{-1} as a function of SiF_4 pressure. These measurements were made with a laser energy of 0.25 J/pulse in a 0.7 cm (external iris) beam. The laser repetition rate was 1.0 Hz. The cell length was 3.85 cm.

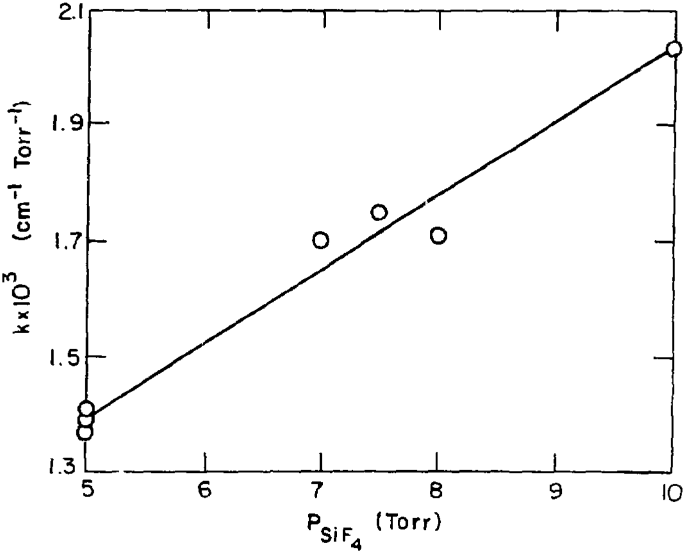

XBL811-5049

the resulting maximum thermal temperature that could be reached in the irradiated volume. The decay of this temperature and the extent to which diffusion can facilitate the reaction of hot molecules at the cell walls are also investigated.

2. Energy Absorbed

The energy absorbed per shot in a pyrolysis was calculated in the following way. The power measurements at PM 2 are divided by the simultaneous readings at PM 1 in order to correct for fluctuations in laser power during the course of the experiment. For each experiment, we define the constants

$$C_o = I_o/I_o^{BS};\ C_c = I_c/I_c^{BS};\ C_T = I_T/I_T^{BS},$$

where I_o^{BS}, I_c^{BS}, and I_T^{BS} are the readings at PM 1 when I_o, I_c, and I_T, respectively, are measured. The value of C_o used was the average of the values obtained from the readings taken before and after the pyrolysis. Since during the pyrolysis only I_T is measured, the absorbed energy must be calculated in terms of I_T and the above constants.

The energy absorbed is calculated as the fraction of the incident energy absorbed times the incident energy. In order to calculate the latter, the observed intensity at PM 2 must be corrected for reflectivity losses at the cell windows. Assuming that the decrease in transmission due to placing an empty cell in the beam is due only to reflective losses at each NaCl or KCl surface, the empty cell transmission is

$$\frac{C_c}{C_o} = (1-r)^4$$

where r is the reflectivity of a single window surface. The value of r based[9] on the refractive index at 1027.4 cm^{-1} is $1 - r = 0.960$ for NaCl and $1 - r = 0.965$ for KCl. Experimentally measured values were within 1% of these values. The measured cell transmissions were in the range

$$\frac{C_c}{C_o} = 0.857 \pm 0.015$$

for KCl windows compared to the theoretical value of 0.867 for KCl. The incident energy reaching the gas after transmission through the two surfaces of the front window is

$$E_{inc} = \left(\frac{C_c}{C_o}\right)^{\frac{1}{2}} I_o.$$

Since the constants C_c and C_o both contain I^{BS} in the denominator,

$$I_o = \frac{C_o}{T_T} I_T,$$

thus

$$E_{inc} = \frac{(C_o C_c)^{\frac{1}{2}}}{C_T} I_T.$$

The fraction of the incident energy absorbed by the gas is

$$A = 1 - \frac{C_T}{C_o\left(\frac{C_c}{C_o}\right)} = 1 - \frac{C_T}{C_c}.$$

The energy absorbed is then

$$E_{abs} = A \times E_{inc} = \left[\frac{(C_c C_o)^{\frac{1}{2}}}{CT} - \left(\frac{C_o}{C_c}\right)^{\frac{1}{2}}\right] I_T.$$

The error in the energy absorbed was typically ±5%. The average energy absorbed per molecule, $\tilde{E}_{abs}$, is obtained by dividing the energy absorbed by the total number of molecules in the irradiated volume,

$$\tilde{E}_{abs} = E_{abs}/(N \times V_{irr})$$

where N is the density of molecules in the gas and V_{irr} is the volume swept out in the cell by the laser beam.

3. Calculation of T_{max}

If it is assumed that the absorbed energy is statistically distributed into thermal energy of the molecules in the irradiated volume, we can calculate the maximum thermal temperature that could be attained.[9] The V-T,R transfer rate governing the transfer of the absorbed vibrational energy to thermal energy is usually determined by the lowest frequency vibrational mode in the molecule.[11] In SiF_4, the lowest frequency vibrational mode[10] has $\omega = 260\ cm^{-1}$. Comprehensive studies[11] of vibrational relaxation in a large series of molecules indicates that this frequency corresponds to a collision number of $Z_{10} = 65$ collisions required for V-T,R equilibration in SiF_4. At an SiF_4 pressure of 5 Torr and using a molecular diameter of $\sigma = 5 \times 10^{-8}$ cm, this equilibration takes place in 60 ns. Tetralin is expected to possess several vibrational modes between 200 to 600 cm^{-1} as well as many in the 1000 cm^{-1} region (see Table V-1) so equilibration with SiF_4 is expected to be rapid. In addition, the SiF_4/tetralin ratio used was always greater than 15.

The peak temperature was calculated assuming that the absorbed energy is statistically distributed among all of the available degrees of freedom. Treating translation and rotation classically, the average thermodynamic energy per molecule for a single gas is given by[10]

$$E = \bar{E}_{abs} + E_o = 3kT + \sum_j g_j \omega_j \frac{e^{-hc\omega_j/kT}}{\left(1-e^{-hc\omega_j/kT}\right)} \qquad (1)$$

where E_o is the initial thermal energy of the system evaluated as E when $\bar{E}_{abs} = 0$, and g_j is the degeneracy of vibrational mode j having frequency ω_j. For a given total energy absorbed, this equation can be numerically

Table V-1. Vibrational frequencies of benzene, cyclohexene and tetralin (in cm^{-1} units)

Benzene	Cyclohexene	Tetralin[a]
398 (2)[b]	236 (2)	236 (2)
608 (2)		
674	507 (4)	541 (10)
707		
846 (2)	791 (4)	833 (8)
967 (2)	905 (2)	
990	970 (2)	
995	1060 (3)	1051 (13)
1010	1127 (2)	
1037 (2)		
1146		
1178 (2)	1247 (4)	
1309	1363 (2)	1412 (15)
1350	1438 (6)	
1482 (2)	1667 (1)	
1585		
1606		
3038		
3047		
3056 (2)	2922 (10)	2960 (12)
3057		
3073		

---

[a] Vibrational frequencies for tetralin are estimates.

[b] Numbers in parentheses are degeneracies.

solved for the resultant temperature.

For a mixture of gases, the resultant temperature is calculated from

$$\bar{E}_{abs} + \sum_i x_i E_{o_i} = 3kT + \sum_i \sum_j x_i g_{ij} \omega_{ij} \frac{e^{-hc\omega_{ij}/kT}}{\left(1-e^{-hc\omega_{ij}/kT}\right)} \qquad (2)$$

where x_i is the mole fraction of gas i.

The calculated temperature, T_{max}, for pure SiF_4 and for a mixture of SiF_4 and tetralin vs absorbed energy per molecule is shown in Figure V-7. The SiF_4 vibrational modes and degeneracies (in parentheses) used[10] are, in cm^{-1} units, 260 (2), 420 (3), 800 (1) and 1022 (3). The 60 vibrational frequencies of tetralin were estimated from the frequencies of benzene[12] and cyclohexene.[13] Particularly accurate values for the tetralin vibrational frequencies are not required to judge the effect of tetralin on the heat capacity of the gas mixture. The estimated tetralin vibrational frequencies were grouped into six classes and average values used. Twelve C-H stretches were taken with the average frequency of the benzene and cyclohexene C-H stretching frequencies. All of the estimated frequencies are listed in Table V-1. The effect of tetralin on the calculated T_{max} is in good agreement with the effect predicted by the heat capacities[14,15] of SiF_4 and tetralin at about 1000°C. The tetralin heat capacity is estimated from group additivities.[15] The heat capacities are listed in Table V-2.

It should be noted that the cross sectional area of the laser beam, hence, the irradiated volume, has a significant and systematic effect on the calculated T_{max}. Increase of the beam diameter from 0.70 to 0.75 cm, for example, using the same total energy absorbed, would result in a T_{max} lower by about 200°. A rectangular or flat top beam profile is desired

Figure V-7. The maximum temperature, T_{max}, that can be reached in the heated gas in the pyrolysis cell assuming statistical, thermal distribution of the energy, calculated from Equation (2), as a function of the total energy absorbed divided by the number of molecules in the irradiated volume. The upper curve is for pure SiF_4, the lower curve for a mole fraction ratio of 0.939:0.061 for SiF_4 and tetralin.

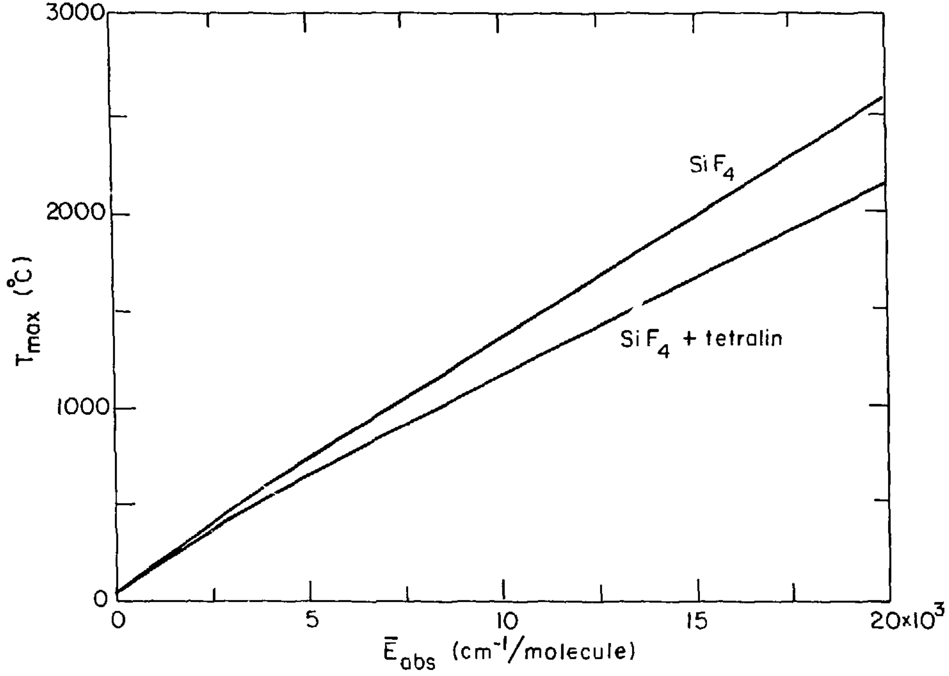
3000
2000
1000
0
T_{max} (°C)
0
5
10
15
20×10³
$\bar{E}_{abs}$ (cm⁻¹/molecule)
Si F_4
Si F_4 + tetralin

XBL811-5048

Table V-2. Heat capacities, C_p (cal/deg mole), of SiF_4 and tetralin

T(K)	SiF_4	Tetralin[a]
300	17.6	41.0
400	19.9	53.2
500	21.4	63.7
600	22.5	72.2
800	23.8	85.8
1000	24.4	94.3
1500	25.2	106.6

---

[a] Estimated from group additivities.[15]

so that a constant temperature is reached across the entire irradiated volume. Using an external iris with a large laser beam sharply defines the beam diameter but the intensity distribution across the beam is not well defined. An internal iris creates a more reproducible intensity distribution, however, there is a much less sharp cut-off at the fringe of the beam and a larger fraction of the energy in the lower energy wings of the beam. T_{max} can easily vary by 500° between the center of the beam and a point at the beam's half width. Precise measurements of T_{max} were not required for experiments that used this configuration. Errors in the estimation of the heat capacity of tetralin are inconsequential considering the large temperature non-uniformity. If more exact temperature measurements are required, a uniform intensity beam profile can be generated, for example, by superimposing multiple reflections of a diverging Gaussian beam with a rectangular light guide.[16] Other reflection techniques can also generate uniform intensity distributions.[17] The calculated values of T_{max} do not necessarily represent the true temperatures reached in the pyrolysis cell, however, they do provide a good relative parameter to be used in comparing sensitized pyrolysis results.

4. Cooling and Diffusion

The decrease of the temperature from T_{max} in the heated cylinder of gas can be estimated by solving the heat equation

$$\frac{\partial^2 u}{\partial x^2} + \frac{\partial^2 u}{\partial y^2} + \frac{\partial^2 u}{\partial z^2} = \frac{1}{K}\frac{\partial u}{\partial t} \qquad (3)$$

for a cylinder of radius a at a temperature u_1 with the outside edge of the cylinder kept at a constant temperature u_0. The temperature u at a distance r from the center of the cylinder at time t is given by[18]

$$u = u_0 + 2\ (u_1 - u_0) \sum_{\alpha} \frac{1}{\alpha J_1(\alpha)} e^{-\alpha^2 Kt/a^2} J_0\ (\frac{\alpha r}{a}) \tag{4}$$

where J_0 and J_1 are zero and first order Bessel functions, the α's are the positive roots of the equation $J_0\ (x) = 0$, and $K = \frac{\kappa}{c_v \rho}$ where c_v is the specific heat at constant volume per gram and ρ is the density. The coefficient of thermal conductivity is given by[19] $\kappa = \frac{1}{3} \bar{c} \lambda c_v \rho$ so K reduces to $K = \frac{1}{3} \bar{c}\lambda$ where $\bar{c} = (8\ kT/\pi m)^{\frac{1}{2}}$ is the average velocity and $\lambda = (\sqrt{2}\ n\pi\sigma^2)^{-1}$ is the mean free path with n being the density of molecules, σ the molecular diameter and m the molecular weight.

Several factors that affect the rate of cooling are not treated in this model. The rate of cooling decreases as the system cools since K depends on $\bar{c}$ and λ which are proportional to $T^{\frac{1}{2}}$ and T, respectively. Heating of the surrounding gas invalidates the boundary conditions and the calculations over-estimate the cooling rate. Calculations were performed for pure SiF_4 since experiments were always carried out at an SiF_4/tetralin ratio greater than 15. Changes in K due to tetralin will be small since its average velocity is only ~10% less than that for SiF_4. The specific heat of SiF_4 decreases[14] by about 10% between 1000 to 500 K and the value at 1000 K, $c_v = 0.21$ cal/g deg is used. A density of $\rho = 5.6 \times 10^{-5}\ g/cm^3$ evaluated for T = 300 K is used. The room temperature density was used since we assume that heating is fast and is initially confined to the irradiated volume with no expansion due to diffusion. Calculations were performed using a value of K calculated for $\bar{c}$ at 1000 K, $\bar{c} = 4.5 \times 10^4$ cm/s, and λ using $n = 1.62 \times 10^{17}$ molecules/cm^3 and $\sigma = 5 \times 10^{-8}$ cm giving $\lambda = 5.6 \times 10^{-4}$ cm and $K = 8.4\ cm^2/s$. Only the first three terms of the summation in Equation (4) are of any consequence on a ms time scale. The relevant values of α and J_1 are $\alpha_1 = 2.4$,

J_1 $(\alpha_1) = 5.6$; $\alpha_2 = 5.5$, J_1 $(\alpha_2) = -0.34$; $\alpha_3 = 8.6$, J_1 $(\alpha_3) = 0.27$.

According to Equation (4), the temperature at time t_o will depend on the initial temperature, the radius of the heated cylinder and the distance from the center of the cylinder. For 5 Torr of SiF_4, a beam diameter of 0.7 cm and an initial temperature of 1000 K, the calculated temperature at the center of the cylinder falls from 904 to 320 K between 1 and 10 ms after t_o (Fig. V-8). Similarly, for an initial temperature of 10,000 K, this model predicts that the temperature has cooled to 436 K in 10 ms. Despite the crudeness of the model, it appears to be clear that cooling in the pyrolysis cell occurs on a ms time scale for the conditions used.

The extent of the diffusion of excited molecules in the pyrolysis cell can be considered to see if hot molecules could reach any surface. Using the previously stated values of $\bar{c}$ at 1000 K and λ, the diffusion constant is $D = \frac{1}{2} \lambda \bar{c} = 6.3$ cm^2 s^{-1}. At a constant temperature of 1000 K, the average diffusion distance in one direction is $\langle x^2 \rangle^{1/2} = (2\ Dt)^{1/2} =$ 0.11 cm in 1 ms, or 3.5 cm in 1 s. At 300 K, the diffusion distances are 0.08 and 2.6 cm in 10^{-3} and 1 s, respectively. The average velocity of tetralin is quite similar to that for SiF_4 ($\bar{c}_{tetralin} = 4.0 \times 10^4$ cm/s at 1000 K) so its diffusion distances should be similar. It is clear that hot molecules cannot diffuse to the side walls, a distance of about 2 cm, in the few milliseconds during which they remain hot. Hot molecules reaching the windows would be potentially more problematical. Only 5% of the molecules in the irradiated volume, however, could diffuse to the window surfaces in 1 ms if the molecules remained at 1000 K. Shock waves travelling through the cell, however, might be able to excite molecules near surfaces. Shock-wave excited molecules would not reach temperatures as high as those of molecules in the irradiated volume.

Figure V-8. The temperature at the center of a 0.7 cm diameter cylinder of 5 Torr of SiF_4, heated to 1000 K at time = 0, as a function of time as calculated by Equation (4). The calculations use the value K = 8.4 cm^2/s.

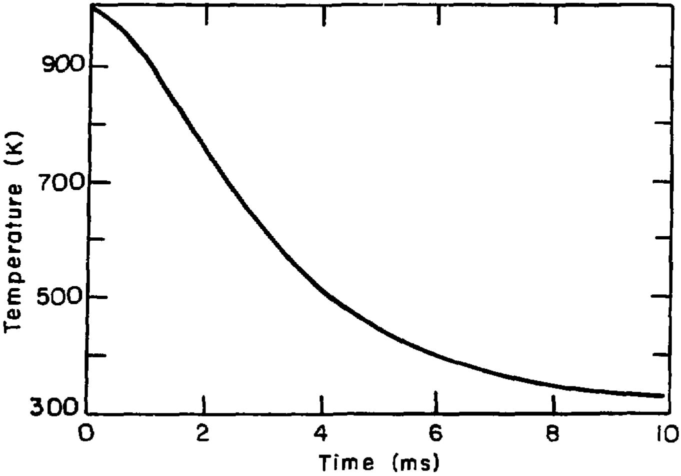

XBL 811-5054

5. Infrared Fluorescence

While infrared fluorescence intensity is not necessarily proportional to the temperature of the emitting species, it does indicate the degree of vibrational excitation. If the excitation in the molecules is thermal, then changes in the IR fluorescence intensity correspond to changes in temperature. IR fluorescence was, therefore, observed during an SiF_4 - sensitized pyrolysis from the irradiated volume in order to monitor the temperature decay in the pyrolysis cell.[20]

All of the observed emission was due to SiF_4 fluorescence. Emission was observed in the 1800-2400 cm^{-1} region corresponding to a two-quantum transition in the 1022 cm^{-1} mode. Total fluorescence above ~700 cm^{-1} was also observed although a large scattered light signal prevented determination of the peak fluorescence signal, and the signal-to-noise ratio was not as good as for purely 5 μm emission. Figure V-9 shows a trace of the 5 μm fluorescence signal from excited SiF_4. The peak fluorescence intensity decays rapidly in the first 50 μs. The rapid decay of fluorescence is apparently due to a shock wave eminating from the center of the cell, transporting energy to the rest of the cell while cooling the central zone. Reflected shock waves can potentially create hot molecules at the surface. However, since the diameter of the cell is about seven times the beam diameter, the energy per molecule at the surface is greatly decreased.

The fast decay is followed by a slower, thermal cooling. Many oscillations are superimposed on the slow decay. These fairly regularly spaced peaks are due to shock waves propagating through the cell. The time between the largest shock wave peaks is 400 ± 25 μs moving from the low to the high end of this range as the time after the laser pulse increased. When the laser beam was moved off center in the pyrolysis cell

Figure V-9. The infrared fluorescence at 5 µm from an SiF_4 - sensitized pyrolysis cell containing 5 Torr of SiF_4. The upper curve (a), shows the fluorescence observed when the laser beam passed directly through the center of the pyrolysis cell. The lower curve (b), shows the fluorescence observed when the laser beam passed through the cell off-center, displaced from the cell axis toward the detector. The beam axis was 1.5 cm from the center of the cell and 0.7 cm from the cell wall. The laser energy was 0.20 J/pulse in a 0.7 cm diameter beam. The droop of the baseline below zero is due to the amplifier response.

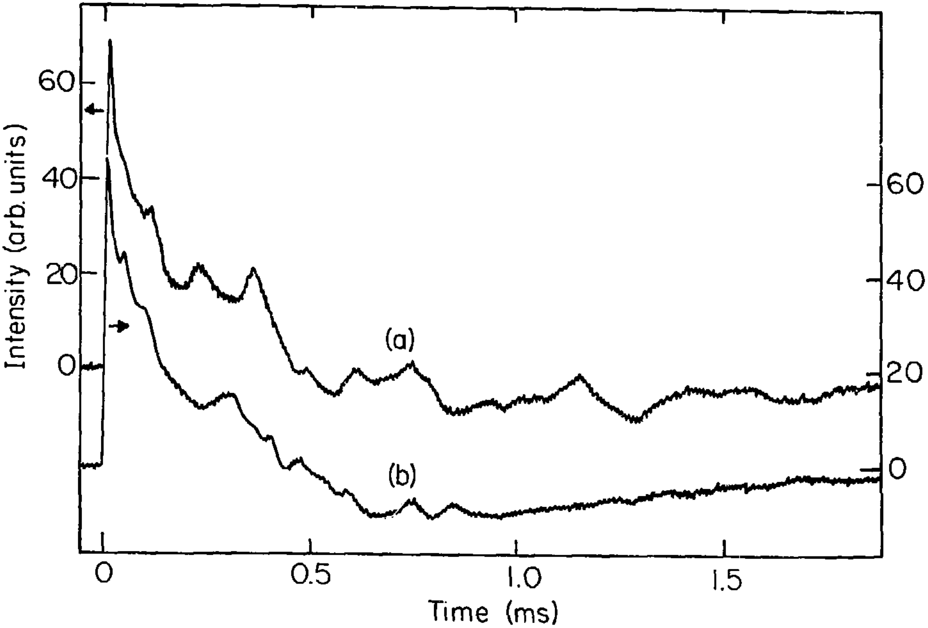

XBL 811-5063

but still in line with the detector, the amplitude of the shock waves was greatly reduced (Fig. V-9b). Fluorescence around 2000 cm^{-1} is seen until about 2 ms after the start of the laser pulse. The fluorescence signal for all frequencies above ~700 cm^{-1}, however, extends to about 10 ms. These observed cooling times agree with the predicted values in the last section.

D. Results

1. Multiphoton Dissociation

Tetralin possesses several absorption features of moderate intensity in the 10 μm region of the infrared spectrum. This portion of the spectrum is shown in Figure V-10 for a liquid smear of tetralin. The largest peak has an absorbance ten times smaller than the strongest absorbance features at 700 and 3000 cm^{-1}. Figure V-11 shows an enlargement of the spectrum of the band irradiated during MPD experiments for the liquid smear as well as for the spectrum of gas phase tetralin. The absorption band in the latter is broader due to increased rotation in the gas phase.

Irradiation of 0.325 Torr of tetralin (1) with a focused CO_2 TEA laser at 946.0 cm^{-1} produced products 2 - 7 and phenylacetylene. Styrene and phenylacetylene had similar GC retention times and were not individually resolved in GC analysis, but were identified by GC-MS analysis. No dissociation products were observed when the laser beam was unfocused.

The product distribution was studied as a function of the laser fluence to determine the effect of the uppumping rate on the competing reaction channels. The results are listed in Table V-3. The product yield of 2, the primary product of ethylene loss and the combined yield of 6 + 7, the products from the dehydrogenation channel, are shown in Figure V-12. The ethylene-loss channel, retro-[2+4] cleavage, is

Figure V-10. The infrared spectrum of a liquid smear of tetralin between NaCl plates in the 900-1100 cm^{-1} range. The resolution is 1 cm^{-1}.

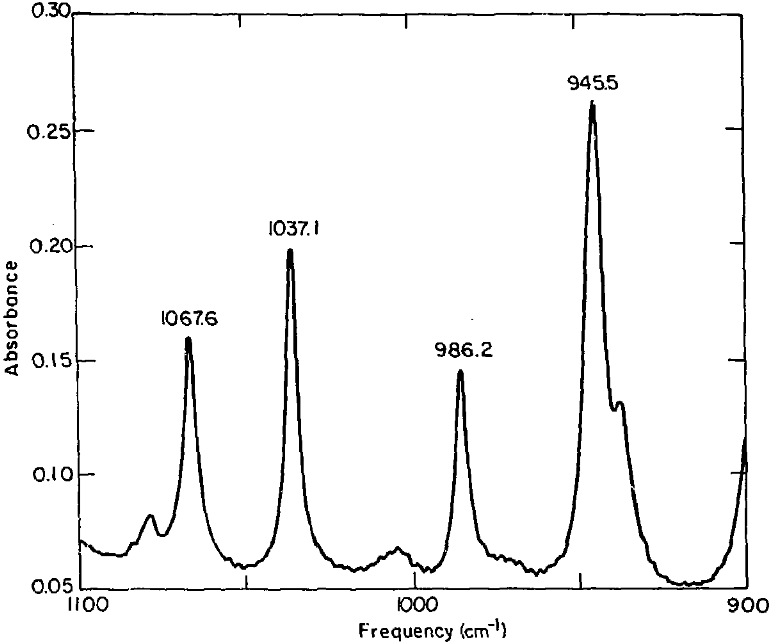
0.30
0.25
0.20
0.15
0.10
0.05
Absorbance
1067.6
1037.1
986.2
945.5
1100
1000
900
Frequency (cm^{-1})

XBL 811-5047

Figure V-11. The infrared spectrum of tetralin in the 915-975 cm^{-1} range. The solid curve is the spectrum of gas phase tetralin (~0.4 Torr) taken with a path length of 9.75 m and a resolution of 1 cm^{-1}. The dashed curve is the spectrum of a liquid smear of tetralin. The absorbance scale refers only to the gas phase spectrum.

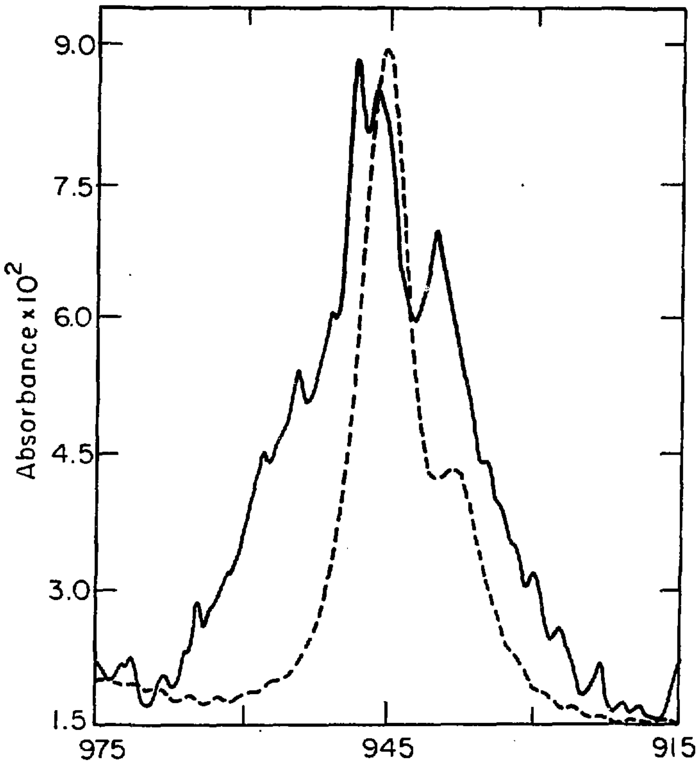

XBL 811-5046

Table V-3. Product distribution from MPD of tetralin

Fluence (J/cm^2)	Pulses (x10^3)	Products (%)							% Conversion of 1
		2	3[a]	4	5	6	7	Other	
23	12.6	72.6	11.7	3.4	4.2	6.2	0.0	2.0	0.4
35	3.6	60.0	22.9	2.3	5.2	6.8	trace	2.9	0.4
46	2.7	54.8	19.7	2.6	5.5	9.0	trace	8.4	0.8
75	2.7	35.5	9.9	7.2	10.6	9.9	8.8	18.1	1.7

---

[a] Includes response of phenylacetylene.

Figure V-12. The yield of 2 and the yield of the dehydrogenation products 6 + 7 as a function of fluence in the MPD of tetralin at 946.0 cm^{-1}.

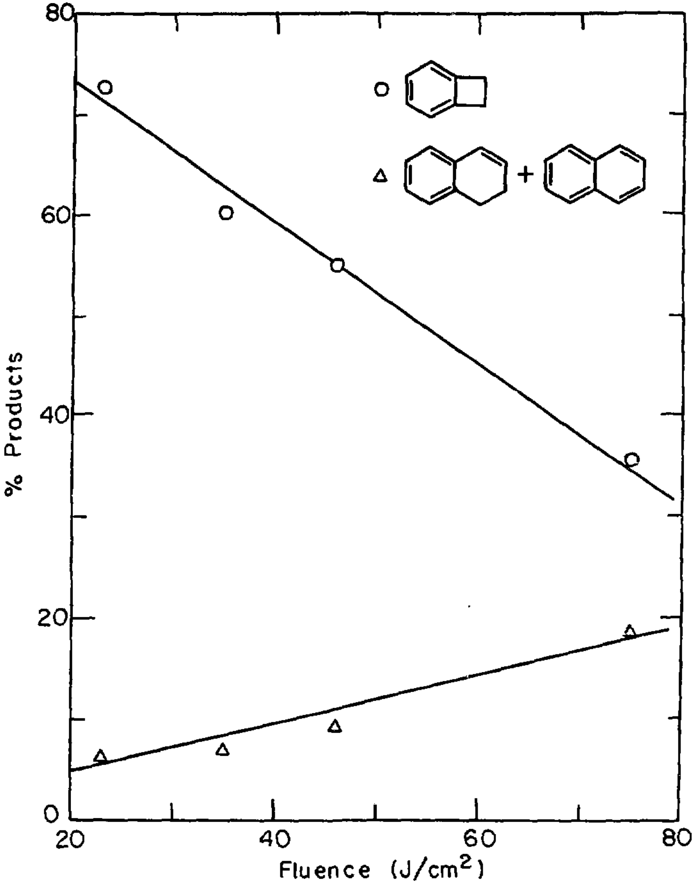

XBL 811-5057

clearly the dominant reaction channel at low fluence. At a fluence of 23 J/cm^2, the ethylene-loss channel accounts for 73% of the total dissociation of tetralin while only 6% of the dissociated tetralin forms dehydrogenation products. At higher fluence, the percentage of the total reaction yield accounted for by 2 decreases and there is a marked increase in the yield of "other" products, tentatively identified by their mass spectra and GC retention times as primarily toluene, ethylbenzene, 1,4-dihydronaphthalene, and o-ethylstyrene.

At all fluences employed except for the lowest fluence, 23 J/cm^2, a bluish visible emission was observed from the focal region. No attempt was made to either spatially or temporally resolve this emission. Visible emission from MPD of other organic molecules,[21] such as methanol and cyclopropane, is often observed under such fluence conditions due to excited C_2 and CH fragments. Fragmentation would complicate the observed product distribution. The observation of phenylacetylene, probably arising from dehydrogenation of excited styrene, is indicative of additional reactions not observed in flow pyrolysis or sensitized pyrolysis. GC-MS analysis of gaseous products shows that the acetylene/ethylene ratio increases from .59 to 1.15 as the fluence is increased from 35 to 75 J/cm^2, indicating high energy processes taking place at higher fluence.

Since MPD yield from tetralin was relatively low (see Table V-3, line 1), and fragmentation apparently complicates the product distribution at high fluence, another technique was desired to study the unimolecular decomposition of tetralin.

2. SiF_4 - Sensitized Pyrolysis

a. Tetralin-h_{12}

SiF_4 - sensitized pyrolysis provides a useful means for studying the unimolecular decomposition of tetralin. Products 2 - 7 are observed. A log-log plot of the total yield of dissociation products vs energy absorbed per molecule (Fig. V-13) shows a linear relationship with a slope of 8.5. The absolute yield of the individual products as a function of the calculated maximum attainable temperature, T_{max}, is shown in Figures V-14 and V-15. Figure V-14 shows the yield of the three primary products, while Figure V-15 displays the yield of the secondary products vs T_{max}. The yield of the secondary products increases more rapidly with increasing T_{max} than does the yield of primary products. The absorbed energy, hence T_{max}, was varied by attenuating the incident laser energy with an SiF_4 attenuation cell or increasing the SiF_4 pressure in the pyrolysis cell. The latter increased T_{max} since the SiF_4 absorption coefficient increased with increasing pressure (see Fig. V-6). The tetralin pressure used was 0.325 Torr and the SiF_4 pressure between 5 to 10 Torr. The total dissociation of tetralin was kept between 2 to 10% of the starting material in these experiments.

The product distribution in terms of the percentage of the total dissociation yield due to a single product is also affected by the absorbed energy per molecule or T_{max} (Table V-4). The yield of 2 and 4 increased relative to the other products as T_{max} decreased. The percentage yield of the primary products, 2, 4, and 6, and the secondary products, 3, 5, and 7, are shown in Figures V-16 and V-17.

Another parameter that had an effect on the product distribution was the number of pulses used to irradiate the sample, N_p. The percentage of products 2, 4, and 6 decreased and the percentage of 3, 5, and 7 increased with increasing N_p. This is believed to be due to dissociation of the accumulated primary products 2, 4, and 6 (see next sub-section).

Figure V-13. A log-log plot of the total decomposition of tetralin (sum of the product yields of all high (>90) molecular weight products) vs energy absorbed per molecule in SiF_4 - sensitized pyrolyses of tetralin. The slope is 8.5. A 0.7 cm diameter laser beam (external iris) at 1027.4 cm^{-1} was used with a 3.85 cm long pyrolysis cell. The tetralin pressure was 0.325 Torr and the SiF_4 pressures were 5,5,6, and 8 Torr, from left to right.

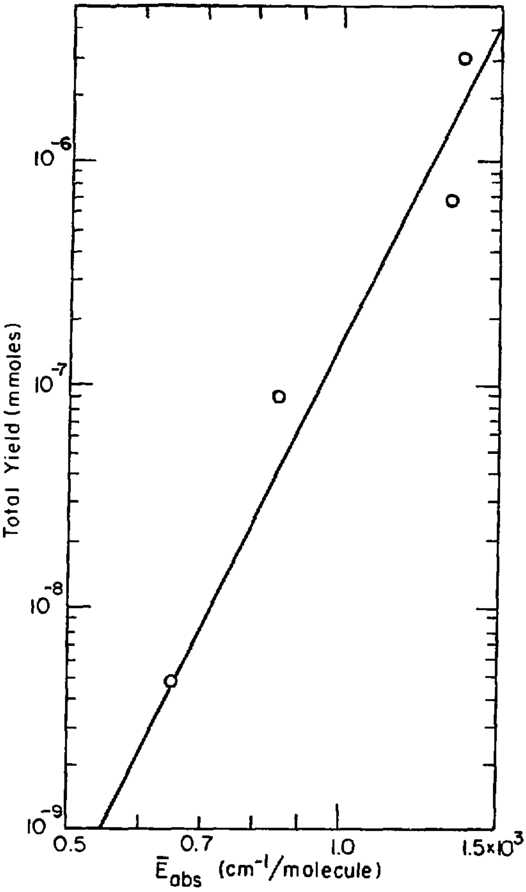
Total Yield (mmoles)
10^{-6}
10^{-7}
10^{-8}
10^{-9}
0.5
0.7
1.0
1.5×10^3
$\bar{E}_{abs}$ (cm^{-1}/molecule)

XBL 811-5037

Figure V-14. The absolute yield of the primary products of the decomposition of tetralin as a function of T_{max} in the SiF_4 - sensitized pyrolysis of tetralin. See Table V-4 for details.

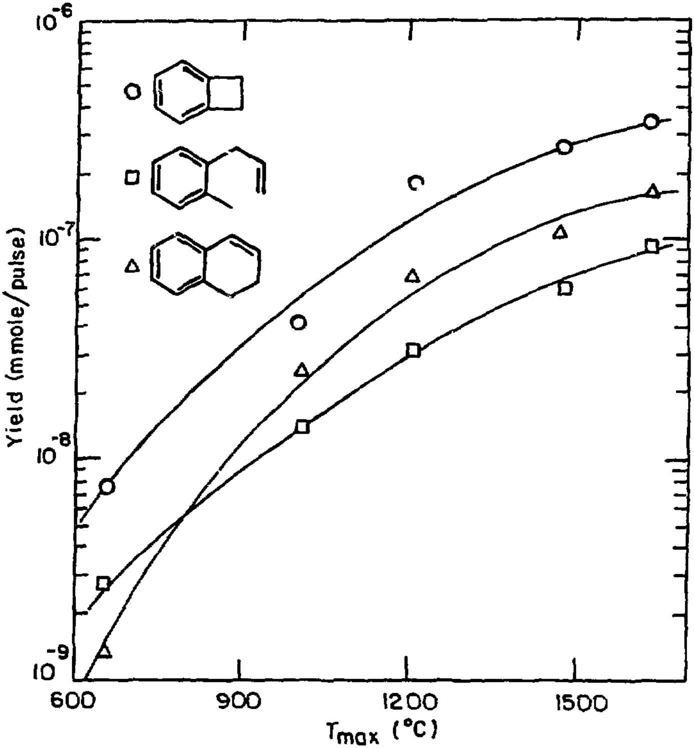

XBL 811-5055

Figure V-15. The absolute yield of the secondary products of the decomposition of tetralin as a function of T_{max} in the SiF_4 - sensitized pyrolysis of tetralin. See Table V-4 for details.

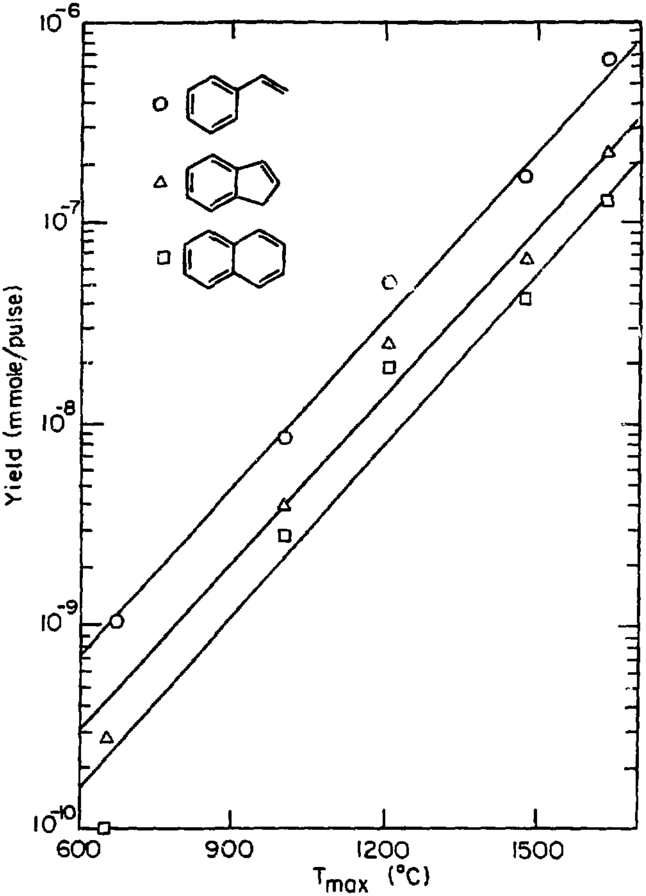
Yield (mmole/pulse)
10^{-6}
10^{-7}
10^{-8}
10^{-9}
10^{-10}
600
900
1200
1500
T_{max} (°C)
○
△
□

XBL811-5059

Table V-4. Product distribution from SiF_4 - sensitized pyrolysis of tetralin[a]

P_{SiF_4} (Torr)	E_{inc} (J)	T_{max} (°C)	Pulses ($x10^2$)	Products (%)						Other	% Conversion of 1
				2	3	4	5	6	7		
5.0	0.11	650	49.6	58.5	8.3	20.8	2.2	10.3	0	0	1.5
5.0	0.14	800	37.2	55.5	9.0	16.8	2.7	16.0	0	0	0.7
5.0	0.18	1000	16.7	45.2	10.0	14.8	3.9	22.7	2.2	1.3	2.8
5.0	0.21	1220	1.8	47.3	12.9	8.0	6.4	17.3	4.9	3.3	4.7
6.0	0.27	1490	1.8	38.2	20.1	8.4	9.4	15.5	5.6	2.8	7.7
10.0	0.21	1650	0.15	20.4	38.2	5.6	13.7	9.9	7.6	4.6	1.7

---

[a] Tetralin pressure = 0.325 Torr, external iris, 0.7 cm beam, 3.85 cm path length.

Figure V-16. The yield of the primary products of the decomposition of tetralin in terms of the percentage of total products vs T_{max} in the SiF_4 - sensitized pyrolysis of tetralin. See Table V-4 for details.

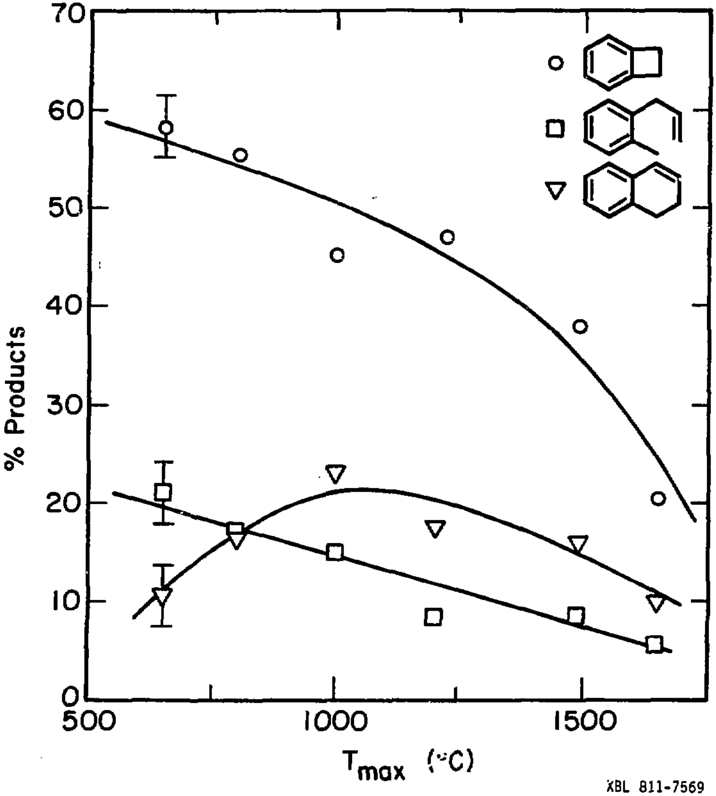

XBL 811-7569

Figure V-17. The yield of the secondary products of the decomposition of tetralin in terms of the percentage of total products vs T_{max} in the SiF_4 - sensitized pyrolysis of tetralin. See Table V-4 for details.

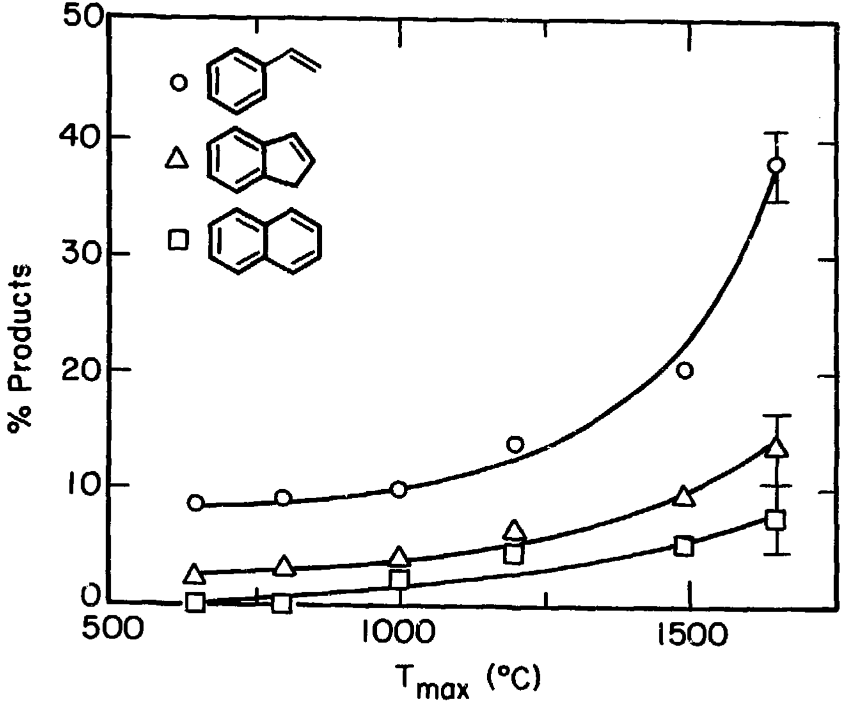

XBL 811-7568

Product 2 and ethylene are the primary products of the retro-[2+4] dissociation channel. Product 3, an isomer of 2, arises, to some extent from secondary decomposition of 2. The ratio of the yield of product 3 to the yield of 2, $R_{32} = 3/2$, as a function of N_p is shown in Figure V-18. The possibly non-zero intercept indicates that another channel of styrene production may exist.

Several experiments were performed to test for non-homogeneous processes during sensitized pyrolysis (Table V-5). A pyrolysis was carried out in a 1.0 cm long pyrolysis cell as opposed to the typical 4.0 cm long cell, in order to investigate the possibility of surface catalyzed reactions. The increase in surface area did not alter the ratio of ethylene-loss to dehydrogenation. As a test for radical chain processes, a sensitized pyrolysis was performed with a radical scavenger, 1 Torr of NO, added to 0.325 Torr of tetralin and 5 Torr of SiF_4. The only observed effect on the product distribution appeared to be that of lowering the T_{max} reached. It should be noted that NO may not be an irreversible scavenger at the temperatures reached, however, most other potential scavengers would themselves dissociate under the pyrolysis conditions used. Pyrolyses were performed with the tetralin pressure reduced from the usual 0.325 Torr to 0.080 and 0.032 Torr. This also had no effect on the ratio of ethylene-loss to dehydrogenation. No products were observed in a 20,000 shot irradiation with T_{max} = 450°C or when no SiF_4 was added to the pyrolysis cell. All GC-MS analyses show no evidence of F atoms in any product or in the starting material.

b. Secondary Decomposition

The primary products formed by the decomposition of tetralin undergo subsequent dissociation under the irradiation conditions used. Pure

Figure V-18. The ratio of styrene to benzocyclobutene (3/2) produced in the SiF_4 - sensitized pyrolysis of tetralin vs the number of laser pulse used in the irradiation. The experiments were performed with 0.325 Torr tetralin, 5.0 Torr SiF_4, a 0.7 cm diameter beam, external iris, 3.85 cm path length and a laser energy of 0.27 J/pulse. The calculated T_{max} was 1400°C.

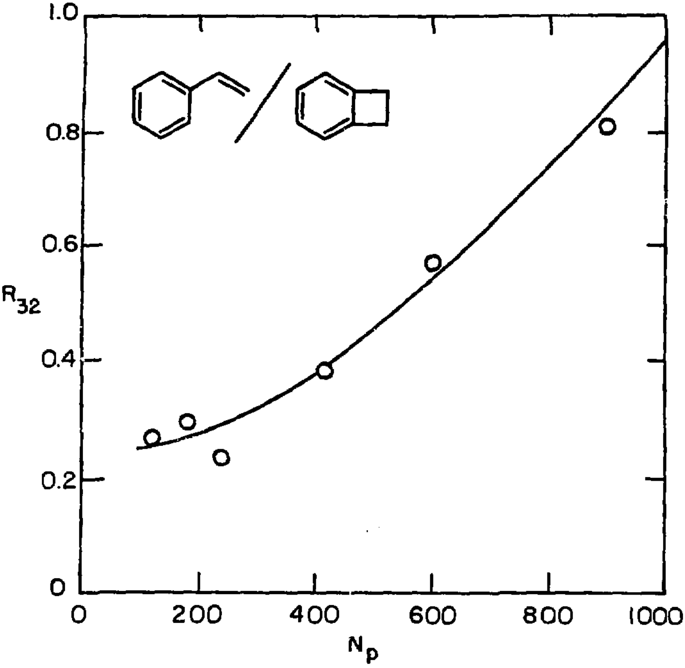

XBL 811-5058

Table V-5. Tests for non-homogeneous reactions in SiF_4 - sensitized pyrolysis of 1

Conditions[a]	E_{inc} (J)	N_p	Products (%)							% Conversion of 1
			2	3	4	5	6	7	Other	
cell length = 1.0 cm	0.27	1200	35.0	24.0	8.4	8.3	14.2	8.5	1.5	28.0
1.0 Torr NO[b]	0.27	300	57.0	10.0	13.2	3.4	15.9	trace	0	1.6
0.080 Torr 1	0.25	1200	30.8	22.6	6.5	8.9	13.3	12.4	5.5	31.4
0.030 Torr 1	0.26	3000	56.0	7.6	1.8	7.6	5.3	20.1	1.6	54.6

---

[a] Pyrolysis conditions: SiF_4 pressure = 5.0 Torr, tetralin pressure = 0.325 Torr, 3.85 cm path length, except where noted.

[b] Calculated T_{max} = 870°C including the effect of the added NO.

samples of 0.325 Torr of 2, 4, and 6 were each subjected to SiF_4-sensitized pyrolysis with 5 Torr of SiF_4. Less than 1/10 of this amount of primary products was ever generated during a tetralin pyrolysis. The results of these pyrolyses are listed in Table V-6. Sensitized pyrolysis of 2 produced exclusively 3. Decomposition of 6 resulted in primarily 7 (68% of product) in addition to smaller quantitites of 5, 1, 3, 1,4-dihydronaphthalene and six unidentified products. Sensitized pyrolysis of 4 produced many products including 5 (24% of products), 1, 3, 6, and seven unidentified products. The unidentified products observed in the dissociation of 4 and 6 are all observed, to a small extent, in SiF_4-sensitized pyrolyses of 1 carried out at high T_{max}.

c. Tetralin-d_4

The deuterium atoms in 1-d_4 are located on the C-1 and C-4 carbons of tetralin. Direct ethylene loss from 1-d_4 produces 2 containing four D atoms (2-d_4). Sensitized pyrolysis of 1-d_4 results in the distribution of isotopomers listed in Table V-7. The results indicate that 2 arises entirely from C_2H_4 loss from 1. The dehydrogenation product, 6, primarily contains 3 deuterium atoms. This indicates that dehydrogenation occurs predominantly from the adjacent 1 and 2 positions rather than a concerted 1,4-elimination which would leave two deuterium atoms in 6 (6-d_2).

The labelling in products 3 and 5 is complex indicating that multiple channels may be producing these products. The effect of the number of pulses used to irradiate the sample on the observed distribution of isotopomers was studied to see what contribution of 3 arises from secondary decomposition of 2 (Table V-7). The percentage of 3-d_4 is substantially increased as the pyrolysis time increases, indicating that 3-d_4 arises primarily from secondary decomposition (isomerization) of 2-d_4. The

Table V-6. Secondary decomposition of primary products

Parent	E_{inc} (J/pulse)	T_{max}[a] (°C)	Pulses	Products (%)									% Conversion
				1	2	3	4	5	6	7	8[b]	Other	
2	0.21	1200	300	-	x	100.0	-	-	-	-	-	-	69.8
4	0.18	1000	100	4.7	-	1.8	x	24.3	1.7	-	-	67.7[c]	16.0
6	0.21	1200	300	5.2	-	2.7	-	10.5	x	68.1	7.5	5.9[d]	21.7

---

[a] T_{max} calculated using the heat capacity of tetralin instead of that for 2, 4, or 6.

[b] 8 is 1,4-dihydronaphthalene.

[c] 7 products.

[d] 6 products.

Table V-7. Deuterium labeling in products from sensitized pyrolysis[a] of 1-d_4

Product	Pulses	% of Total Products	Isotopomer (%)			
			d_4	d_3	d_2	d_1
2	300	47.3	100.0[b,c]	0	0	0
	900	31.9	100.0	0	0	0
3	300	12.9	32.4	8.1	28.7	30.8
	900	25.5	58.1	10.7	16.0	15.2
4	300	8.0	100.0	0	0	0
	900	7.9	100.0	0	0	0
5	300	6.4	0.5	42.0	42.5	15.1
	900	7.1	4.5	41.4	40.4	13.6
6	300	17.3	9.6	83.0	7.3	0
	900	15.9	8.6	80.9	10.5	0
7	300	4.9	0	1.2	94.6	4.1
	900	4.7	0	20.1	72.3	7.6

---

[a] Pyrolysis conditions: 1-d_4 (0.325 Torr) was irradiated with 300 or 900 pulses, 0.27 J/pulse, with 5 Torr SiF_4. T_{max} was 1430°C.

[b] The numbers are the percent of product with the indicated number of deuterium atoms as determined by GC-MS analysis.

[c] The data are corrected for ^{13}C natural abundance and 98.7% deuterium incorporation in 1-d_4.

percentage of the total product yield accounted for by the other isotopes of 3 ([3-d_1 + 3-d_2 + 3-d_3] x % total product) remains relatively constant, 8.7 and 10.7% respectively for the 300 and 900 shot pyrolyses.

d. Tetralin-d_{10}

The two hydrogen atoms in 1-d_{10} are in the *cis*-1,2 positions. This facilitates the study of the stereochemistry of the dehydrogenation reaction. The isotopic distribution of products 6 and 7 are shown in Table V-8. Concerted 1,2-hydrogen elimination would occur with *cis*-hydrogen atoms, producing exclusively 6-d_8 and 6-d_{10}. The large amount of 6-d_9 observed (38%) indicates that non-concerted or step-wise hydrogen loss is taking place. A large percentage of 7-d_7 (48%) is also observed.

e. Tetralin-h_{12} + tetralin-d_{12}

A 1:2 mixture of 1-h_{12} and 1-d_{12} was subjected to sensitized pyrolysis in order to determine if intermolecular reactions were taking place. The hydrogen product from solely unimolecular dehydrogenation would be a mixture of H_2 and D_2. The results of mass spectral analysis of the hydrogen products are shown in Table V-9. The results are corrected for the responses of H_2 and D_2 obtained from independent calibration runs (Sec V-B.2). The approximately 40% yield of HD indicates that hydrogen is produced by intermolecular reactions. GC-MS analysis of the higher molecular weight products shows substantial scrambling in 3 and 5. No scrambling was detectable in the starting 1-h_{12} or 1-d_{12} or in products 2, 4, 6 or 7.

E. Discussion

In order to discern the lowest energy reaction pathway in the unimolecular decomposition of tetralin, the reaction products must be properly grouped so as to reflect the total yield for each reaction channel. The

Table V-8. Deuterium labeling in dehydrogenation products from sensitized pyrolysis[a] of 1-d_{10}

	Isotopomer, %				
Product	d_{10}	d_9	d_8	d_7	d_6
6	21.5[b]	38.5	40.1	0	-
7	-	-	37.9	49.1	13.0

---

[a] Pyrolysis conditions: 1 - d_{10} (0.325 Torr) was irradiated with 1000 pulses, 0.19 J/pulse, with 5 Torr SiF_4. T_{max} was 1050°C.

[b] The data are corrected for ^{13}C natural abundance and 97.8 % deuterium incorporation in 1-d_{10}.

Table V-9. Hydrogen product from the sensitized photolysis of mixtures of $\underline{1}$-h$_{12}$ and $\underline{1}$-d$_{12}$[a]

	Sample		Products, %		
Run	1-h$_{12}$ (Torr)	1-d$_{12}$ (Torr)	H$_2$	HD	D$_2$
1.	0.15	0.34	30.0	39.8	30.3
2.	0.16	0.34	29.7	38.8	31.5
3.[b]	0.16	0.34	27.1	42.0	30.9

---

[a] SiF$_4$ pressure = 5 Torr, laser intensity = 0.20 J/pulse, T_{max} = 1120°C.

[b] Same photolysis as 2 but this spectrum taken 5 min after run 2 with the sample constantly flowing into the mass spectrometer.

dependence of the product distribution on the number of pulses used to irradiate the sample and on T_{max} indicate that products 3, 5, and 7 arise primarily from secondary decomposition of 2, 4, and 6. Previous workers have not detected 4 as a primary decomposition product of 1 in flow pyrolysis experiments. This is presumably due to secondary decomposition of 4 in the latter. In sensitized pyrolysis experiments, the accumulated products are exposed to high temperatures for only a few ms after each laser pulse. Secondary decomposition is therefore significantly reduced relative to that observed in flow pyrolysis experiments. The peak in the percentage yield of 6 as a function of T_{max} (Fig. V-16) is a result of the competition between its production and secondary decomposition. The percentage yield of 2 and 4 monotonically decrease with increasing T_{max} due to the ease of their secondary decomposition relative to their production from decomposition of 1.

The dependence of the isotopic distribution of 3 obtained from the pyrolysis of 1-d_4 on the number of pulses used to irradiate the sample shows, that for long irradiation times, the majority of the 3 produced is derived from 2. At low conversion, however, there appear to be multiple channels for the formation of 3. This is confirmed by the labelling results from the sensitized pyrolysis of 1-d_{10}. The observed ratio of the yield of 3 to that of 2 as a function of the number of irradiation pulses appears to also indicate that 3 does not solely arise from the secondary decomposition of 2 accumulated in the cell. This result, however, is inconclusive due to the low single shot yields and the ill-defined intercept. The mixed isotope experiments indicate that there are also intermolecular mechanisms for the production of 3.

Secondary decomposition of 4 also produces 3. Under the conditions used for the secondary decomposition experiment, however, it produced more 5 than 3. Since production of 5 is always less than 10% of the total product, and since we do not know the ratio of 5/3 produced from the secondary decomposition of 4 as a function of T_{max}, we simply take the yield for the ethylene-loss channel to be the sum of the yields of 2 + 3. The yield of the disproportionation channel is taken to be the yields of 4 + 5, although the mixed isotope experiments indicate that some fraction of indene formation is intermolecular. The formation of 5 from either 4 or 6 (Fig. V-19) is consistent with the observed production of 5-d_2 and 5-d_3 from the sensitized pyrolysis of 1-d_4. The yield of the dehydrogenation channel is taken as the sum of the 6 and 7 produced.

The results of the percent product yield vs T_{max} are shown in Figure V-20 using the groupings just described. It is clear from these results and the results for MPD (Figure V-12) that the ethylene-loss channel is the lowest energy pathway for the homogeneous, gas phase dissociation of 1. The product distributions from these experiments are at variance with the results of pyrolysis of 1 in a flow reactor. We conclude that the larger yield of 6 and 7 in flow reactors[1,2] is due to surface catalyzed dehydrogenation. These effects are eliminated in both laser-induced dissociation techniques. It is interesting to note that SiF_4 - sensitized pyrolysis and MPD (at low fluence) create similar distributions of products despite the differing internal energy distributions in the excited tetralin. Any minor differences in the product distribution can be attributed to differing efficiencies of secondary decomposition. In MPD experiments, dissociation products containing significant internal excitation may already be in the QC and can themselves undergo MPD during the same laser pulse.

Figure V-19. A mechanism for the production of indene (5) from 4 or 6.

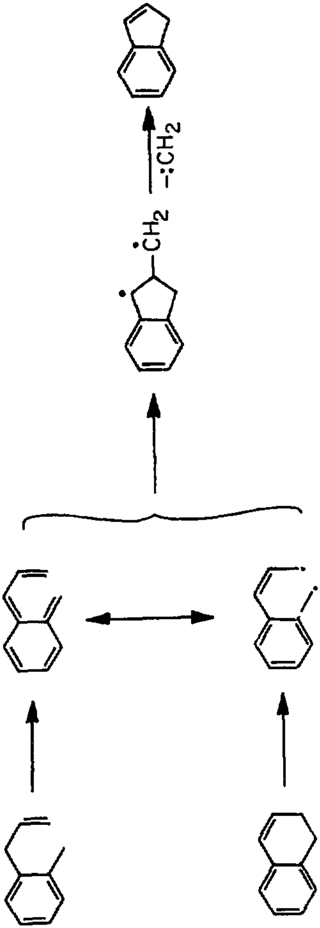

XBL 811-5041

Figure V-20. The percentage of the total product yield of the three major reaction channels for the decomposition of tetralin as a function of T_{max}. The products are grouped as follows: ○ - 2 + 3; △ - 4 + 5; □ - 6 + 7.

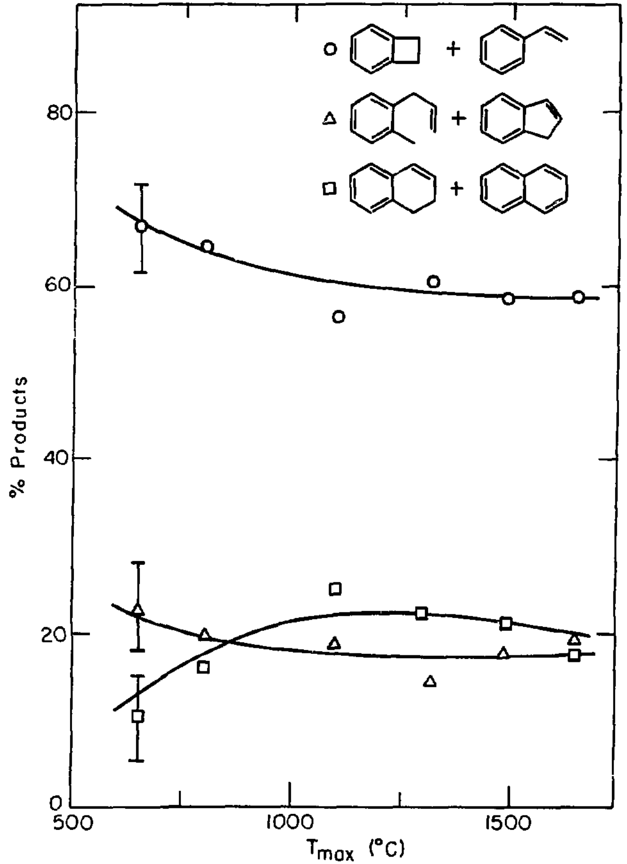

XBL 811-5044

The results of the sensitized pyrolyses of the isotopically labeled tetralins can be used to elucidate the mechanism of dehydrogenation. The isotopic distribution of 6 from the dissociation of 1-d_4 shows primarily 6-d_3. The loss of only one H atom indicates that dehydrogenation results in the loss of hydrogen from C-1 and C-2 of tetralin. This is in contrast to 1,4-dehydrogenation which is favored by Woodward-Hoffmann rules for concerted H_2 elimination and is seen as the primary mode of dehydrogenation in cyclohexene.[22] The transition state for such a concerted H_2 loss in tetralin, however, would be destabilized as the ring aromaticity would be lost. The production of 6-d_9 from the sensitized pyrolysis of 1-d_{10} and the generation of HD in the sensitized pyrolysis of a mixture of 1-h_{12} and 1-d_{12} indicate that dehydrogenation is a step-wise, intermolecular process. Two reasonable candidates for this mechanism are depicted in Figure V-21. Thermochemical calculations were carried out for both pathways using group additivities[15] (see Tables 10 and 11). At 1000 K, both pathways are feasible. It should be noted that Franz[23] has shown that the major product from the 1- and 2-tetralyl radicals (generated from the corresponding *t*-butyl peresters at 900 K) is 1,2-dihydronaphthalene. The fact that the addition of NO to a sensitized pyrolysis mixture did not significantly affect the product distribution can be attributed to its not being an irreversible radical scavanger at high temperatures.

Two possible mechanisms for the production of 2 are shown in Figure V-22. It cannot be determined from these experiments whether or not 2 is produced from a concerted or step-wise retro-(2 + 4) reaction. The activation energy, E_a, for the concerted process is estimated[4] as the E_a for the cyclohexene retro-(2 + 4) reaction plus 8 kcal/mole due to destabilization of the transition state due to the loss of aromaticity.[4]

Figure V-21. Two possible mechanisms for the production of 1,2-dihydronaphthalene (6) from tetralin. The upper pathway assumes C-H bond cleavage in tetralin while the lower pathway takes C-C bond cleavage in tetralin as the initial step. Both pathways produce free H atoms.

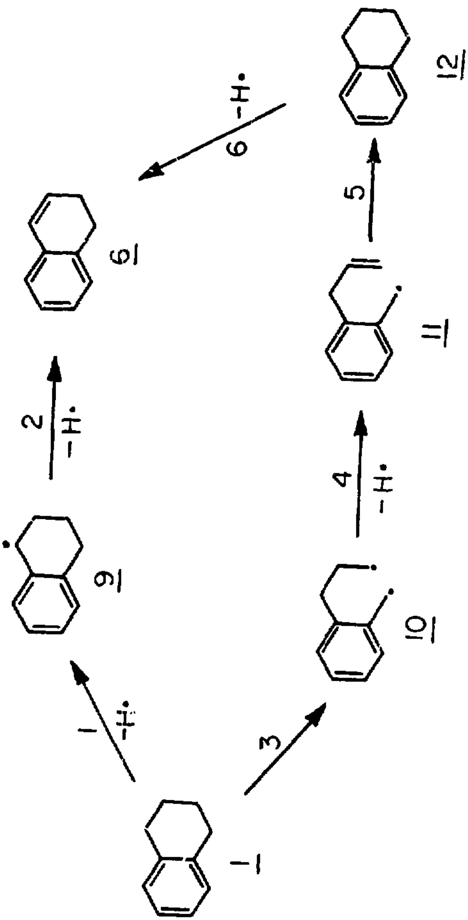

XBL 811-5039

Table V-10. Estimated thermodynamic quantitites for the compounds in Figure V-21.

Compound	ΔH°_{298} (kcal/mole)	S°_{298} (cal/deg mole)	C°_p (800 K) (cal/deg mole)
<u>1</u>	6.57	86.75	85.79
<u>9</u>	36.13	83.77	83.68
<u>6</u>	35.34	82.72	79.38
<u>10</u>	73.80	102.04	85.30
<u>11</u>	58.35	100.66	81.32
<u>12</u>	48.88	88.15	82.56

Table V-11. Estimated thermodynamic quantities for the reactions in Figure V-21 at 1029°C

Reaction	ΔH° (kcal/mole)	ΔS° (cal/deg mole)	ΔG° (kcal/mole)
1	84.4[illegible]	28.67	47.13
2	50.15	24.79	17.87
3	66.74	14.57	47.77
4	37.57	27.52	1.74
5	-8.23	-10.69	5.68
6	38.52	22.06	9.80

Figure V-22. Two possible mechanisms for the production of benzocyclobutene (2) from tetralin. The upper pathway is a concerted ethylene loss while the lower channel involves step-wise C–C bond cleavage. The lower pathway also leads to the production of o-allyltoluene (4).

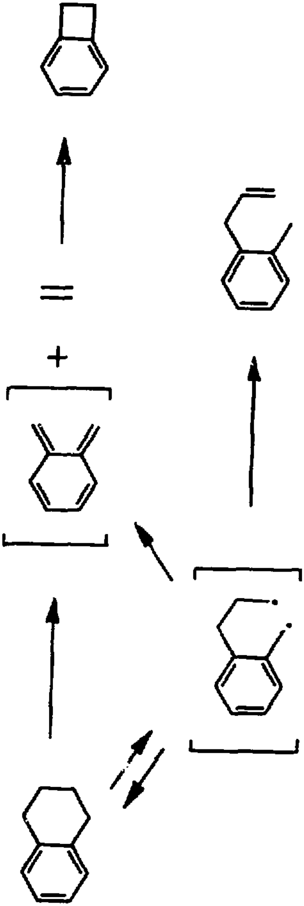

XBL 811-5042

This gives E_a = 74.2 kcal/mole for the concerted ethylene-loss from tetralin. The $\Delta H^\circ_{f_{298}}$ of the diradical intermediate in a step-wise process was estimated,[4] using group additivity parameters,[15] to be 67.23 kcal/mole above the $\Delta H^\circ_{f_{298}}$ of tetralin. The activation energy for ethylene loss from the diradical[4] is about 6 kcal/mole making both the concerted and step-wise processes feasible.

Since 2 and 6 can both possibly arise from the same diradical intermediate that leads to 4, a unified mechanism can be constructed (Fig. V-23) in which the branching between the three major reaction channels occurs solely at the diradical. Further experiments would be needed to confirm whether this unified mechanism or some combination of the previously described pathways best describes the unimolecular decomposition of tetralin.

Figure V-23. A possible unified mechanism for the production of all of the primary products of the decomposition of tetralin, 2, 4 and 6, from the diradical generated by C-C bond cleavage in tetralin.

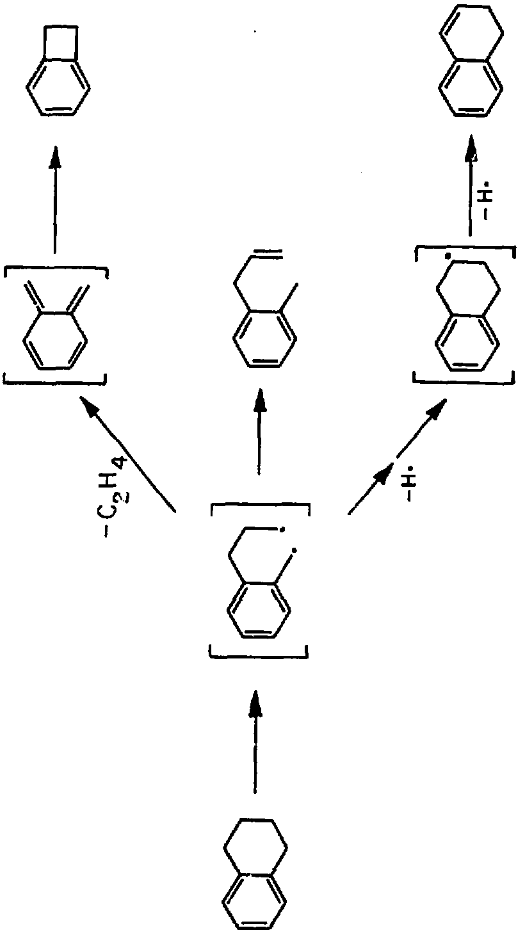

XBL 811-5040

References

1. a) A. G. Loudon, A. Maccoll, and S. K. Wong, J. Chem. Soc. (B), 1733 (1970); b) R. J. Hooper, H. A. J. Battaerd and D. G. Evans, Fuel, 58, 132 (1979); c) P. Bredael and T. H. Vinh, Fuel, 58, 211 (1979); d) B. M. Benjamin, E. W. Hagaman, V. F. Raaen and C. J. Collins, Fuel, 58, 386 (1979); e) T. Gangwer, D. MacKenzie, and S. Casano, J. Phys. Chem. 83, 2013 (1979).

2. M. R. Berman, P. B. Comita, C. B. Moore, and R. G. Bergman, J. Am. Chem. Soc. 102, 5692 (1980).

3. K. J. Olzyna, E. Grunwald, P. M. Keehn, and S. P. Anderson, Tet. Lett. 1609 (1977).

4. P. B. Comita, Ph.D. Dissertation, University of California, Berkeley (to be published).

5. W. E. Farneth, G. Glynn, R. Slater and N. J. Turro, J. Am. Chem. Soc. 98, 7877 (1976).

6. C. Cheng and P. Keehn, J. Am. Chem. Soc. 99, 5808 (1977); D. Garcia and P. M. Keehn, J. Am. Chem. Soc. 100, 6111 (1978).

7. C. Steel, V. Starov, P. John, R. G. Harrison and R. Leo, in Laser Induced Processes in Molecules, Ed. K. L. Kompa and S. D. Smith (Springer-Verlag, New York, 1979), p. 198.

8. W. M. Shaub and S. H. Bauer, Int. J. Chem. Kinet. 7, 509 (1975).

9. E. Grunwald, K. J. Olszyna, D. F. Dever and B. Krishkowsky, J. Am. Chem. Soc. 99, 6515 (1977).

10. J. D. Lambert, Vibrational and Rotational Relaxation in Gases (Oxford University Press, Oxford, 1977), p. 66.

11. G. Herzberg, Infrared and Raman Spectra of Polyatomic Molecules (Van Nostrand Reinhold, New York, 1945).

12. G. Herzberg, Electronic Spectra of Polyatomic Molecules, (Van Nostrand Reinhold, New York, 1966).

13. N. Neto, C. DiLauro, E. Castellucci and S. Califano, Spectrochimica Acta 23A, 1763 (1967).

14. JANAF Thermochemical Data (Dow Chemical Co., Thermal Laboratory, Midland, MI, 1963).

15. S. W. Benson, Thermochemical Kinetics (Wiley, New York, 1976); H. E. O'Neal and S. W. Benson in Free Radicals, Vol. II, Ed. J. K. Kochi (Wiley, New York, 1973), p. 275.

16. R. E. Grojean, D. Feldman, and J. F. Roach, Rev. Sci. Instrum. 51, 375 (1980).

17. SPAWR Optical Research, Inc., 1527 Pomona Rd., Corona, CA 91720.

18. F. Bowman, Introduction to Bessel Functions (Dover, New York, 1958), pp. 37-39.

19. R. D. Present, Kinetic Theory of Gases (McGraw Hill, New York, 1958).

20. Similar IR fluorescence experiments have been performed by D. Golden at SRI (unpublished).

21. M. L. Lesiecki and W. A. Guillory, J. Chem. Phys. 66, 4317 (1977); S. E. Bialkowski and W. A. Guillory, J. Chem. Phys. 67, 2061 (1977).

22. D. C. Tardy, R. Ireton, and A. S. Gordon, J. Am. Chem. Soc. 101, 1508 (1979).

23. J. A. Franz and D. M. Camaioni, J. Org. Chem., in press.